ÉCOLE DES PONTS PARISTECH / UNIVERSITÉ PARIS-EST

P H D T H E S I S

to obtain the title of

PhD of the University of Paris-Est

Specialty : SCIENCE, ENGINEERING AND ENVIRONMENT

Defended by

Yongfeng QU

Three-dimensional modeling of radiative and convective exchanges in the urban atmosphere

Thesis defended on November 18, 2011

Jury

President :	Dr. Patrice G. MESTAYER	-	IRSTV
Reviewers :	Dr. Majorie MUSY	-	CERMA
	Dr. Valéry MASSON	-	Météo-France
Examinators :	Pr. Jean François SINI	-	École Centrale de Nantes
	Pr. Jean Philippe GASTELLU-ETCHEGORRY	-	CESBIO
	Pr. Marina K.A. NEOPHYTOU	-	University of Cyprus
Advisor :	Dr. Bertrand CARISSIMO	-	CEREA
Co-advisor :	Dr. Maya MILLIEZ	-	EDF R&D
Co-advisor :	Dr. Luc MUSSON-GENON	-	EDF R&D

Acknowledgments

This research was conducted with the financial support from EDF. I thank Grégoire Pigeon for providing access to the CAPITOUL data and the Defense Threat Reduction Agency (DTRA) for providing access to the MUST data.

I would like to express my gratitude to my advisor, Bertrand Carissimo, for his insightful suggestions and guidance. More particularly, I must thank my co-advisor, Maya Milliez, whose endless patience, good-natured helpfulness, throughout kept the thesis on track and substantially improved it at every stage. I would like also to recognize the contribution of my co-advisor Luc Musson-Genon who gave me invaluable advice and provided me administrative assistance on numerous occasions.

I would like to express my sincere gratitude to Majorie Musy and Valéry Masson who take precious time off from their tight schedule to be reviewer. I also thank to Patrice Mestayer for accepting to be the president of the jury. I am greatly indebted to Jean-François Sini and Patrice Mestayer for their careful reading of the manuscript and helpful comments. My special thanks go to Jean Philippe Gastellu-Etchegorry, and Marina Neophytou for their participation in the jury committee members and the interest they have shown in my work.

My thanks go also to Christian Seigneur, Director of the CEREA, for hosting me in his laboratory. Thanks to all the CEREA members who have instructed and helped me a lot in the past three years. Also thanks to the personel of the university of Paris-Est and doctoral School for their kind support.

I am also grateful to the department MFEE of EDF R&D for hosting me in Chatou and for providing the facilities to conduct this thesis.

I would also like to acknowledge the CERMA laboratory for their technical assistance on the SOLENE software, especially, Julien Bouyer and Laurent Malys.

I am greatly indebted to people for their many helpful suggestions and comments: Richard Howard, Alexandre Douce, Namane Méchitoua, Matthieu Guillaud, David Monfort, James Voogt, Jörg Franke, Bert Blocken, Dominique Groleau. Special thanks go to my friends and colleagues who have supported me throughout my research: Denis Wendum, Dominique Demengel, Eric Gilbert, Eric Dupont, Raphael Bresson, Cédric Dall'ozzo, Fanny Coulon, Venkatesh Duraisamy, Marie Garo and Hanane Zaïdi and many others.

There is not enough space, here, to mention all the people who have helped me, with scientific discussions, or with their friendship and encouragement, during this thesis work. I would like to thank all of them.

I would like to dedicate this thesis to my family ...

Contents

Nomenclature

Superscripts

$\downarrow$	incoming	
$\uparrow$	outgoing	-
n	time step n	-

Subscripts

int	internal building or deep soil	
ref	reference height	-

Roman Symbols

C	heat capacity	$J\ K^{-1}\ m^{-2}$
CFL	Courant-Friedrichs-Lewy number	-
C_p	specific heat capacity	$J\ kg^{-1}\ K^{-1}$
C_μ	turbulence model coefficient	-
d	distance of the cell center to the wall	m
e	wall thickness	m
e_a	water vapor pressure	Pa
E_1	constant in the Bird model associated with aerosol absorption	-
$f_m,\ f_h$	Louis stability functions	-
F	cloud factor	-
F_c	ratio of the forward-scattered irradiance to the total scattered irradiance due to aerosols	-
g	gravity	$m\ s^{-2}$
$\widetilde{G}$	production or destruction rate due to buoyancy	-
h	altitude angle of the sun	rad
h_f	heat transfer coefficient	$W\ m^{-2}K^{-1}$
H	height	m
$I(\underline{x},\underline{D})$	intensity of radiation at the location ($\underline{x}$) along the propagation direction with the vector $\underline{D}$	$W\ m^{-3}\ sr^{-1}$
$I(z)$	turbulent intensity	-

k_s	equivalent roughness height	m
$k(z)$	turbulent energy	$m^2\ s^{-2}$
K	surface conductance	$W\ K^{-1}\ m^{-2}$
$K_a(\underline{x})$	radiation absorption coefficient	-
L	long-wave radiative flux	$W\ m^{-2}$
L_a	long-wave radiative flux from the sky	$W\ m^{-2}$
L_e	long-wave radiative flux from the multi-reflection on the other surfaces	$W\ m^{-2}$
$L(\underline{x},\underline{D})$	monochromatic luminance	$W\ m^{-3}\ sr^{-1}$
m	air mass	$kg\ m^{-3}$
p	pressure	Pa
Pr_t	turbulent Prandtl number	-
$\widetilde{P}$	production rate of turbulent energy	-
q_{rad}	radiative heating rate	$W\ m^{-3}$
Q_{cond}	conductive heat flux	$W\ m^{-2}$
Q_E	latent heat flux	$W\ m^{-2}$
Q_F	anthropogenic heat flux	$W\ m^{-2}$
Q_H	sensible heat flux	$W\ m^{-2}$
ΔQ_A	advective heat flux	$W\ m^{-2}$
ΔQ_S	storage heat flux	$W\ m^{-2}$
Q^*	net radiation flux	$W\ m^{-2}$
Re_L	Reynolds number based on the integral scale of the flow	-
S	short-wave radiative flux	$W\ m^{-2}$
S_0	solar constant ($= 1370$)	$W\ m^{-2}$
S_{dr}	solar Rayleigh diffusion flux	$W\ m^{-2}$
S_{dae}	solar aerosol diffusion flux	$W\ m^{-2}$
S_{dg}	solar reflection flux by the surface	$W\ m^{-2}$
S_D	direct solar flux	$W\ m^{-2}$
S_{Dn}	direct normal solar flux	$W\ m^{-2}$
S_e	solar flux diffused by the environment	$W\ m^{-2}$
S_f	solar flux diffused by the atmosphere above	$W\ m^{-2}$
S_k, S_ε	extra source terms of turbulence and dissipation	-

S_{rad}	extra thermal source	$J\ K\ m^{-5}s^{-1}$
T	temperature	K, °C
T_a	air temperature	K, °C
T_{br}	brightness surface temperature	K, °C
$T_{g/b}$	deep soil or internal building temperature	K, °C
T_{se}, T_{sfc}	external surface temperature	K, °C
u_*	friction velocity	$m\ s^{-1}$
U	wind speed	$m\ s^{-1}$
ν_t	turbulent viscosity	$m^2\ s^{-1}$
$\widetilde{\nu}$, ν', $\overline{\nu}$	Favre average for RANS, its fluctuation, the ensemble average	-
w	precipitation water content	-
y_P	a distance from the center point P of the wall-adjacent cell to the wall	m
z_g	ground level	m
z_G	boundary layer height	m
z_0	aerodynamic roughness length	m
z_{0_T}	thermal roughness length	m
z^+	dimensionless wall distance z/z_0	-
Z	sun zenith angle	rad

Greek Symbols

α, α_g, α_s	albedo, averaged ground albedo, clear sky or atmospheric albedo	-
β	wind power-law exponent	-
ε	emissivity of the surface	-
ε_{clr}	effective or apparent emissivity	-
$\varepsilon(z)$	dissipation rate	-
κ	von Kármán constant	-
λ	average thermal conductivity	$W\ m^{-1}K^{-1}$
μ	viscosity of the fluid	$kg\ m^{-1}s^{-1}$
μ_t	thermal admittance	$J\ m^{-2}\ s^{-0.5}\ K^{-1}$
ν	kinematic viscosity	$m^2\ s^{-1}$
ω	Earth angular frequency	Hz

$d\Omega$	element of the solid angle (sr) around the direction $\underline{D}$	-
ϕ	wind angle	$^\circ$
ρ	density	$kg\ m^{-3}$
σ	Stefan-Boltzmann constant ($= 5.66703 \times 10^{-8}$)	$W\ m^{-2}\ K^{-4}$
σ_t	turbulent Prandtl number	-
τ	number of seconds in a day	s
τ_w	wall shear stress	$N\ m^{-2}$
τ_a	transmittance due to aerosol absorption and scattering	-
τ_{aa}	transmittance due to aerosol absorption	-
τ_{ad}	transmittance due to aerosol scattering	-
τ_{aw}	transmittance due to water vapor absorption	-
τ_g	transmittance due to mixed gas absorption	-
τ_{oz}	transmittance due to ozone absorption	-
τ_r	transmittance due to Rayleigh diffusion	-
θ	potential temperature	K, $^\circ$C

Acronyms

1D, 2D, 3D	one-, two-, three-dimensional
ABL	Atmospheric Boundary Layer
AIJ	Architectural Institute of Japan
AMS	American Meteorological Society
CAO	Computer-Aided Design
CAPITOUL	Canopy and Aerosol Particles Interactions in TOulouse Urban Layer field experiment
CEREA	Centre d'Enseignement et de Recherche en Environnement Atmosphérique (Atmospheric environment teaching and research center)
CERMA	CEntre de Recherche Méthodologique d'Architecture (Center for Methodological Research in Architecture)
CFD	Computational Fluid Dynamics
Code_Saturne	3D open source CFD code developed by EDF and CEREA
COST	European COoperation in Science and Technology research group
DART	Discrete Anisotropic Radiative Transfer model
DNS	Direct Numerical Simulation

DOM	Discrete Ordinates Method
DTRA	Defense Threat Reduction Agency
EDF	Électricité De France (French electricity company)
ERCOFTAC	European Research Community on Fluids, Turbulence And Combustion organizations
FOV	angular Fields Of View
IOP	Intensive Observation Periods
IPCC	Intergovernmental Panel on Climate Change
IRT	InfraRed Thermometer
JAPEX	Joint ATREUS-PICADA EXperiment
LES	Large Eddy Simulation
LST	Local Standard Time
LUMPS	Local-scale Urban Meteoro-logical Parameterization Scheme
MBE	Mean Bias Error
MUST	Mock Urban Setting Test field experiment
RANS	Reynolds-Averaged Navier-Stokes
RMSE	Root Mean Square Error
RNG	ReNormalization Group
RTE	Radiative Transfer Equation
SEB	Surface Energy Balance
SOLENE	thermo-radiative software developed by CERMA
SUMM	Simple Urban Energy Balance Model for Mesoscale Simulations
SVF	Sky View Factor
SYRTHES	SYstèm de Résolution THErmique Solide code developed by EDF
TEB	Town Energy Balance scheme
TKE	Turbulent Kinetic Energy
TIR	Thermal InfraRed
TOPEUM	Towards Optimisation of urban-planning and architectural Parameters for Energy Use minimisation in Mediterranean cities campaign
TUF-3D	Temperatures of Urban Facets in 3D
PBL	Planetary Boundary Layer
UBL	Urban Boundary Layer
UCL	Urban Canopy Layer

UCLCM	Urban Canopy Layer Climate Model
UHI	Urban Heat Island
UT	Universal Time
WBCSD	World Business Council for Sustainable Development
WHO	World Health Organization

CHAPTER 1

Context and objectives

Contents

1.1 Background

Urbanization is a sign of modernization, industrialization and mobilization. It implies for a transformation in the social environment, political organization and division of work. On the other hand, rapid urban extension in the last century had far-reaching consequences for sustainability and had profoundly changed the environment by everyday activities. Furthermore, more than half of the world's population live in urban areas. As described by Oke (1987), the process of urbanization produces radical changes in the nature of the surface and atmospheric properties of a region. It involves the transformation of the radiative, thermal, hydrologic and aerodynamic characteristics and thereby alters the natural energy and hydrology balances, as well as the wind and turbulence levels.

Therefore, among the many issues and challenges involved in urban development, are the environmental ones, such as:

- Urban heat island
- Air quality
- Pedestrian wind comfort
- Energy management

1.1.1 Urban heat island

The Urban Heat Island (UHI) phenomenon consists in an increased air temperature within cities in comparison to the rural surroundings. It was first identified by Howard (1820) over the city of London. Especially at night, the air temperature difference can reach 3 to 10 K for large agglomerations (Oke, 1987). The deterioration of the urban thermal environment has been recognized as a serious problem during the summer months even in mid-latitude regions. During heat waves, it can lead to serious consequences in terms of public health. This was revealed during an important heat wave in August 2003 that affected Europe and caused more than $70,000$ victims, with a majority in urban areas ($15,000$ in France) (Hémon and Jougla, 2003). This deterioration could become worse in the context of climate change (temperature increase even larger in cities due to a positive feedback) (McCarthy et al., 2010).

Consequently, urban development initiatives that consider the influence on the urban thermal environment have received more attention than they have in the past. In addition, a thermally comfortable environment would be pleasant for the inhabitants and commuters in urban areas.

It is also worth noting that the UHI is seen during both summer and winter. Rational utilization of the UHI effect in winter may get some advantages: reducing the need for heating, making the snow on the roads melt faster etc. Moreover, most plants are sensitive to temperatures and only grow above a certain threshold. In areas which are affected by the UHI effect there is more growth in most plants, so whilst it may be practical from an agricultural point of view.

1.1.2 Air quality

The heat wave that struck Europe in summer 2003 was not only extreme in temperature but also in the persistence of high ozone concentrations for almost three weeks. The World Health Organization (WHO) states that more than two million people die each year from causes directly attributable to air pollution (WHO, 2006). Current research concludes that emissions in buildings are one of the major sources of the pollution that causes urban air quality problems, and pollutants that contribute to climate change. They account for 49% of sulfur dioxide emissions, 25% of nitrous oxide emissions, and 10% of particulate emissions, all of which damage urban air quality. From the source of World Resource Institute, based on data for 2000, buildings (including residential and commercial buildings) produce 15.3% greenhouse gas emissions ahead of industry (10.4%) and transportation (13.5%) sectors. In that event, sustainable development requires the improvement of the interrelationships between a building, its components, its surroundings, and its occupants.

1.1.3 Energy management

The World Business Council for Sustainable Development (WBCSD, 2009) points out that 40% of the world's energy use is consumed in buildings. New buildings that will use more energy than necessary are being built every day, and millions of today's inefficient buildings will remain in 2050. On one side, in order to reduce the global energy-related carbon footprint by 77% or 48 Gigatons to stabilize CO_2 levels in order to reach the ones recommended by the Intergovernmental Panel on Climate Change (IPCC), the building sector must radically make cut in energy consumption. On the other side, this presents an excellent opportunity for business to develop new products and services that cost-effectively reduce the energy burden on consumers and countries while contributing to the slowdown of climate change. This market could be worth between US$ 0.9 trillion and US$ 1.3 trillion.

1.1.4 Pedestrian wind comfort

Near high-rise buildings, it can happen that wind reaches high velocities at pedestrian levels, contributing to general discomfort of the city inhabitants or even being dangerous. In March 2011, in the United Kingdom, high winds blustered in Yorkshire for almost one day long, causing some minor structural damages to buildings and roads. Moreover, a report of the Daily

Mail described how a pedestrian was killed and another injured when a lorry overturned and toppled over them during a high wind episode in the center of the city of Leeds. Actually, there have already been recorded instances of people being blown off their feet near high-rise buildings. Lawson and Penwarden (1975) reported dangerous wind conditions to be responsible for the death of two old ladies in 1972 after being blown over by sudden wind gusts.

On the other hand, in weak wind region, a good urban ventilation helps to reduce the UHI. This is definitely an advantage with the raising concerns regarding the cost and environmental impact of energy use. Not only does wind provide natural ventilation (outdoor air) to ensure safe healthy and comfortable conditions for building occupants without the use of fans, it also provides free cooling without the use of mechanical systems. Adequate urban ventilation is also helpful to increase air pollutant dispersion around buildings (Shirasawa et al., 2008).

In fact, the construction of a building inevitably changes the microclimate and the ventilation in its vicinity. Therefore, the design of a building should not only focus on the building appearance and on providing good indoor environment, but should also include the effect of its architecture on the outdoor environment. The impact of buildings on outdoor environment, in particular related to wind, has received relatively little attention, so far.

1.2 Urban physics

As a consequence of these issues, focus was given on the research in the field of urban physics, aiming to better understand and model the phenomena occurring in urban areas and the atmosphere above, such as heat, moisture and momentum transfers, pollutant and acoustic dispersion, radiative transfer etc. Urban physics cover a large range of disciplines: meteorology, fluid dynamics, thermal, aerodynamics, and acoustics etc. For instance, in the field of wind engineering, urban physics analyze the effects of wind in the built-up environment and studies the possible damages or benefits which may result from wind. In the fields of air pollution, urban physics also includes low and moderate winds as these are relevant to dispersion of contaminants.

1.2.1 Spatial and temporal scales and urban boundary layer

The interactions between urban areas and the atmosphere above imply various scales. Orlanski (1975) gives a rational subdivision of scales for atmospheric processes:

- synoptic scale (scale of largest cyclones, distance larger than 2000 *km*)
- mesoscale (between synoptic scale and larger than microscale, from 2000 *km* to 200 *km* and from 200 *km* to 2 *km*)
- microscale (near-ground atmospheric phenomena, distance less than 2 *km*). More recently, microscale includes smaller scales, such as: building scale (less than 100 *m*), building component scale (less than 10 *m*) even building material scale.

Scale dependent parameterizations are needed to include the influences of built-up areas on meteorological fields in atmospheric models. In order to study the impact of an urban area on its surroundings (scale varying from 10 to 100 *km*) mesoscale modeling is used, where the influence of obstacles is parameterized. In order to study the phenomena occurring within the urban canopy (scale varying from 100 *m* to 2 *km*) obstacle resolving microscale models are used, where the obstacles are explicitly included in the mesh. Nevertheless, while characteristic scales of phenomena resulting from single obstacles are relatively small ($\sim$ 100 *m*, $\sim$ *minutes*) and can be resolved, in reality there are always multiple obstacles as, for example in urban areas; many buildings, in a wind turbine park; many turbines, or in a forest; many trees. In these cases, hardly all obstacles can be resolved with sufficient detail, and their impacts need to be parameterized (Schlünzen et al., 2011). To additionally calculate the interaction of canopy layer processes and the air above, a coupling between mesoscale and microscale models can be used. Based on Orlanski (1975), Randerson (1976) and Schlünzen et al. (2011) (Fig. 1.1) summarize the spatial scales of phenomena that can be directly simulated in a mesoscale model and microscale model and that have to be parameterized in a model or to be considered via the boundary values. The boundary layer over an urban area is of particular interest as it is in this layer of the atmosphere that the majority of observations in urban areas are made (Oke, 1987; Stull, 1988). It is therefore important to know what these observations represent. As air flows from one surface to another an internal boundary layer forms. The internal boundary layer is influenced by the new surface and deepens with fetch. The internal boundary layer formed over urban areas is the Urban Boundary Layer (UBL) (Oke et al., 1999; Stull, 1988). The buildings

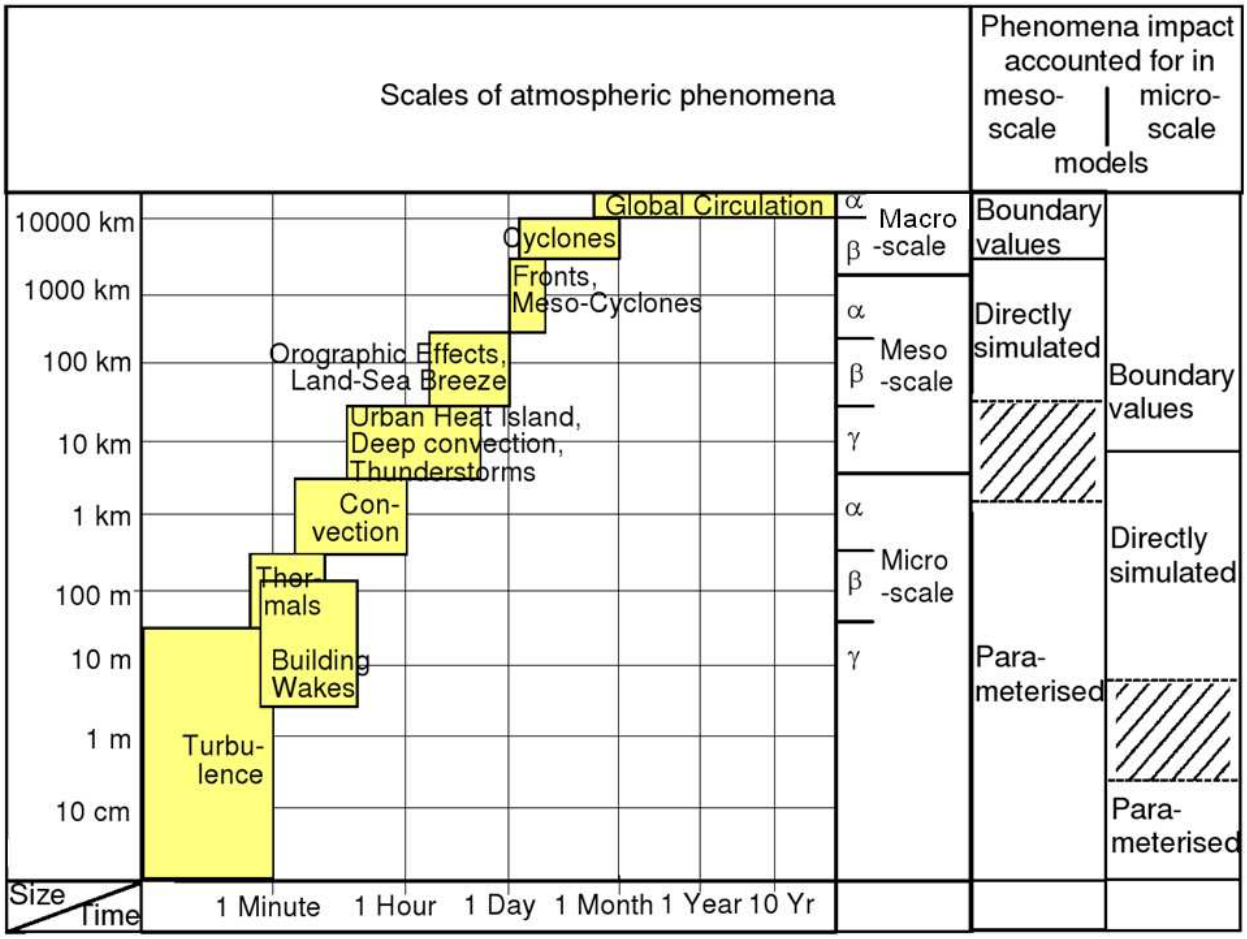

Figure 1.1: Spatial and temporal scales of atmospheric phenomena and how these phenomena are treated in Reynolds-Averaged Navier-Stokes (RANS) mesoscale or obstacle resolving micro scale models (right columns). Dashed areas in the right columns indicate the currently used RANS model resolutions and the resulting possibly resolvable minimum phenomena sizes. From Schlünzen et al. (2011).

introduce a large amount of vertical surfaces, high roughness elements, artificial materials, and impervious surfaces (such as buildings and pavements that are made of dark colors absorb the heat which causes the temperature of the surface and surrounding air to increase). The most well-known consequences are the UHI, the generation of local flows between the city center and its outskirts and between the various city districts, and the 'urban plume' downwind of a city. In calm or low wind condition, the warmer air in the city core rises, pulling air near the surface radically inward and a radially outward return flow develop aloft. This air circulation forms the 'urban dome' (a dome of heated air above the cities due to pressure differences between warmer temperatures in the city and cooler temperatures in the surrounding rural areas). The UBL structure and its various sub-layers are depicted in Figure 1.2.

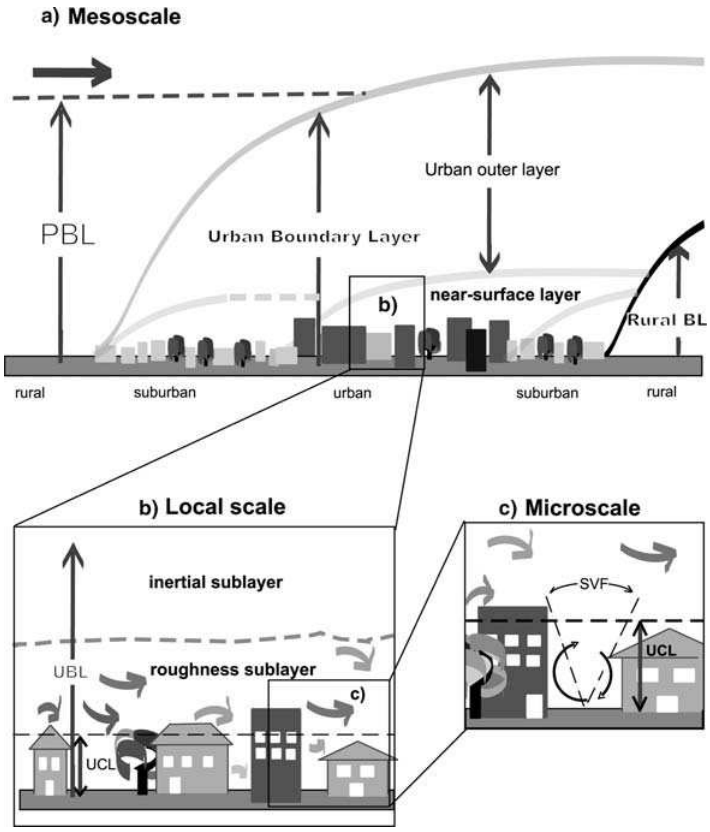

Figure 1.2: Schematics of the urban boundary-layer structure indicating the various (sub)layers and their names. a) PBL: planetary boundary layer; in b) UCL: urban canopy layer; in c) SVF: sky view factor. From Rotach et al. (2005); modified after Oke (1987).

1.2.2 Urban energy balance

Knowledge of the surface energy balance is essential to understand urban climate and boundary layer processes. Oke (1987) defines the energy balance for a building and air volume containing different heat fluxes as illustrated in Figure 1.3, with the following equilibrium relationship:

$$Q^* + Q_F = Q_H + Q_E + \Delta Q_S + \Delta Q_A, \tag{1.1}$$

where Q^* ($W\ m^{-2}$) is the net radiation flux through the volume, Q_F ($W\ m^{-2}$) is the anthropogenic heat flux release within the volume, Q_H ($W\ m^{-2}$) and Q_E ($W\ m^{-2}$) refer to convection of sensible heat flux and latent heat flux respectively. The terms ΔQ_S ($W\ m^{-2}$) and ΔQ_A ($W\ m^{-2}$) are storage of heat in the ground and the buildings and advective heat transfer within the volume. Note that here the terms 'convection' and 'advection' refer to vertical turbulent transfer and mean horizontal transfer, respectively.

For dry surfaces, the energy balance in equation (1.1) is simplified by neglecting Q_E, and if the sites are horizontally homogeneous, ΔQ_A can be also ignored. Therefore, surface temperature results from the balance of energy exchanges at the surface given the incoming radiative forcing, the local ambient air temperature, and the surface radiative properties.

1.2.2.a Radiative balance Q^*

The net radiative flux at a surface reads:

$$Q^* = S^{\downarrow} - S^{\uparrow} + L^{\downarrow} - L^{\uparrow}, \tag{1.2}$$

where $S^{\downarrow}$ ($W\ m^{-2}$) and $S^{\uparrow}$ ($W\ m^{-2}$) are respectively the incoming and outgoing short-wave radiative fluxes, $L^{\downarrow}$ and $L^{\uparrow}$ are respectively incoming and outgoing long-wave radiative fluxes ($W\ m^{-2}$).

Incoming short-wave radiation can be decomposed into its direct and diffuse component, and for both short- and long-wave radiation we can distinguish the contributions coming from the atmosphere above and from the urban environment:

$$S^{\downarrow} = S_D + S_f + S_e, \tag{1.3}$$

$$L^{\downarrow} = L_a + L_e, \tag{1.4}$$

where S_D ($W\ m^{-2}$) is the direct solar flux, S_f ($W\ m^{-2}$) the solar flux diffused by the atmosphere above, S_e ($W\ m^{-2}$) the flux diffused by the environment (i.e. from multi-reflection on the

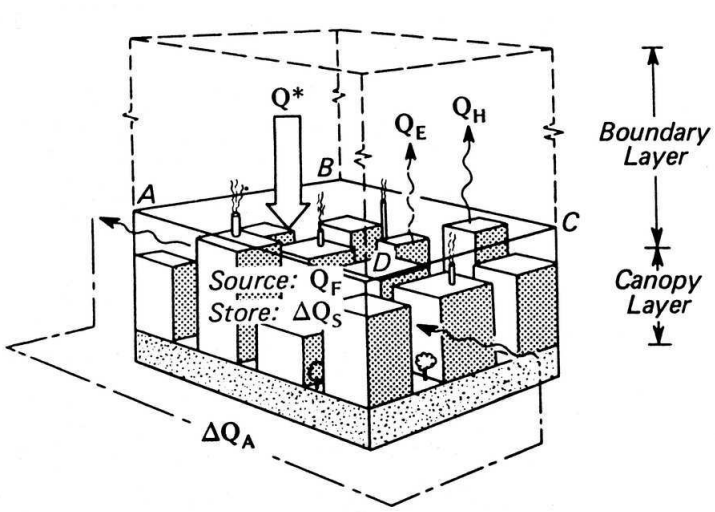

Figure 1.3: Schematics of the urban energy balance in an urban building-air volume. From Oke (1987). The base of the averaging volume is determined as the level across which there is negligible energy transfer on time scales of more than a day. With: Q^* ($W\ m^{-2}$) the net radiation; Q_H ($W\ m^{-2}$) the sensible heat flux; Q_E ($W\ m^{-2}$) the latent heat flux; ΔQ_S ($W\ m^{-2}$) storage; ΔQ_A ($W\ m^{-2}$) the advective flux; and Q_F ($W\ m^{-2}$) the anthropogenic heat flux.

surfaces). L_a ($W\ m^{-2}$) and L_e ($W\ m^{-2}$) are the long-wave radiation fluxes from the sky and from the multi-reflection on the other surfaces.

Outgoing solar radiation expresses by the albedo (usually written α, a dimensionless quantity) which is the fraction of solar radiation reflected by a surface. Albedo determines how much solar energy, a particular substance reflects. Hence, $S^{\uparrow}$ reads:

$$S^{\uparrow} = \alpha(S_D + S_f + S_e). \tag{1.5}$$

Outgoing long-wave radiation is decomposed into an emitted and reflected part. It is a function of surface temperature T_{sfc} (K) and surface emissivity (usually written ε, a dimensionless quantity). Emissivity of a particular material is the fraction of energy that would be radiated by a black body at the same temperature. For a black body ε would be equal to 1, while for any real object $0 < \varepsilon < 1$. Thus, $L^{\uparrow}$ reads:

$$L^{\uparrow} = \varepsilon\sigma T_{sfc}^4 + (1-\varepsilon)(L_a + L_e), \tag{1.6}$$

where σ is the Stefan-Boltzmann constant ($5.66703 \times 10^{-8}\ W\ m^{-2}\ K^{-4}$).

1.2.2.b Anthropogenic heat flux Q_F

Anthropogenic heat flux is generated by humans and human activity, whilst it has a small influence on rural temperatures, it becomes more significant in dense urban areas (Washington, 1972). The American Meteorological Society (AMS) defines it as: "Heat released to the atmosphere as a result of human activities, often involving combustion of fuels. Sources include industrial plants, space heating and cooling, human metabolism, and vehicle exhausts. In cities this source typically contributes $15 \sim 50\ W\ m^{-2}$ to the local heat balance, and several hundred $W\ m^{-2}$ in the center of large cities in cold climates and industrial areas."

Anthropogenic heat flux is one contributor to UHI. Although it is usually smaller (not in high latitude cities) compared to other fluxes, its influence is observable (Pigeon et al., 2007). Anthropogenic heat generation can be estimated by adding all the energy used for heating and cooling, running appliances, transportation, industrial processes, plus that directly emitted by human metabolism.

1.2.2.c Sensible heat flux Q_H

Surface sensible heat flux is the energy exchanged between a surface and the air in the presence of a surface-air thermal gradient. Modeling the sensible heat flux contributes to determine both stratification effects on turbulent transport, and to estimate the surface temperature. The sensible heat flux Q_H can be parameterized as:

$$Q_H = h_f(T_a - T_{sfc}), \tag{1.7}$$

in which h_f ($W\ m^{-2}K^{-1}$) is the heat transfer coefficient and T_a (K) the air temperature.

We give a detailed comparison between different approaches to model the heat transfer coefficient in Chapter 3.

1.2.2.d Storage heat flux ΔQ_S

The storage heat flux is a significant component of the energy balance (Grimmond and Oke, 1999b). Knowledge of the storage heat flux term is required in a variety of applications, for example to model evapotranspiration, sensible heat flux, boundary layer growth, etc. Furthermore, the thermal inertia provided by this storage term is often regarded as a key process in UHI. It accounts for 17% to 58% of the daytime net radiation, and is greater at the more urbanized sites (downtown and light industrial) (Grimmond and Oke, 1999b). Considered at the

hourly timescale ΔQ_S is variable. However, ΔQ_S is difficult to measure or model because of the complex three-dimensional (3D) structure of the urban surface and the diversity of materials. It is often determined as the residual of the surface energy balance equation (Grimmond and Oke, 1999b).

Camuffo and Bernardi (1982), Grimmond and Oke (1999b) suggest a hysteresis-type equation to characterize the storage heat flux as a linear function of Q^* and of the temporal variation of Q^*:

$$\Delta Q_S = a_1 Q^* + a_2 \frac{\partial Q^*}{\partial t} + a_3, \tag{1.8}$$

where t (s) is time. The parameter a_1 describes the overall strength of the dependence of the storage heat flux on net radiation. The parameter a_2 is the coefficient of retardation of ΔQ_S with respect to Q^*. The parameter a_3 is an intercept term that indicates the relative time when ΔQ_S and Q^* turn negative. Parameters a_1, a_2 and a_3 can be calculated through regression for hourly averaged data.

1.3 Objectives and structure of the thesis

This work aims to contribute to study the detailed energy exchanges between buildings and the urban atmosphere (the distribution of surface temperatures). It involves developing a model coupling thermal transfers involving the buildings and a Computational Fluid Dynamics (CFD) modeling of the atmosphere in an urban area. The numerical model used is the atmospheric module of the 3D open source CFD code *Code_Saturne* developed by EDF and CEREA. In previous work, a microscale 3D atmospheric radiative scheme has been implemented in the code to model the energy balance for complex geometries (Milliez, 2006). The surface temperature is modeled with a simple approach, the force-restore method. The new scheme has been validated with simple cases found in the literature (Milliez, 2006).

Four objectives of this research are as follows:

- The first objective of the thesis is to improve the heat transfer model in buildings, by testing two modeling approaches: the force-restore model and a one-dimensional (1D) conduction scheme. For both approaches, the aim is to perform sensitivity studies to thermal parameters and material properties and in particular to internal building temperature.

- The second objective is to compare with another 3D radiative model which uses the

geometric view factor approach: the SOLENE model (Miguet and Groleau, 2002). The comparisons are made for the short-wave direct and diffused fluxes, long-wave incoming fluxes and surface temperatures.

- The third objective is to study the full radiative-convective coupling. In most models taking into account the radiation in built-up environment (integrative or 3D models), the airflow, required for calculating the convective flux, is parameterized and rarely fully modeled. The radiative and thermal models implemented in the CFD code *Code_Saturne* has the advantage of being coupled with the dynamic module, in particular through the use of a common grid.

  However, in previous studies (Milliez, 2006), the radiative-dynamical interaction has been discussed in a simple way, using a constant pre-calculated and thus decoupled flow field. The full radiative-dynamical coupling is nevertheless already implemented, it needs to be studied in detail in this thesis, including the thermal impact on airflow and on surface temperatures of taking into account a 3D flow field for the computation of convective fluxes. Such a detailed study (which may be computationally expensive) may provide a better understanding of the phenomena at microscale.

- The last objective includes the validation of our approach with field measurements on an idealized urban environment as well as on a real city district. This requires a detailed analysis of the available data sets in order to identify the surface properties, the input and meteorological data (radiative fluxes and wind) as well as mesh generation of very complex geometries.

In Chapter 2, I first present some basic CFD aspects and urban energy models, then describe our radiative-dynamical coupled model. Chapter 3 presents a validation of the radiative-dynamical model with observations (MUST field experiment) and compares three schemes of increasing complexity for predicting convective flux (published paper). In Chapter 4, I compare our radiative model with the SOLENE model. Chapter 5 consists in a numerical investigation on the thermal impact on a low wind speed airflow within an idealized built-up area (submitted paper). In Chapter 6, I perform numerical simulation of a real urban area case (a district of Toulouse, CAPITOUL case) including data analysis, complex mesh generation and simulation results. Chapter 7 highlights the main conclusions and provides perspectives for future work.

CHAPTER 2

Model design

Contents

2.1 General CFD modeling approach for the urban environment

In the past decades, Computational Fluid Dynamics has been intensively used to evaluate the indoor environment of buildings and heat and mass transfer between the indoor environment and the building envelope (Loomans et al., 2008). It has also been used in research on wind flow and the related processes in the outdoor environment around buildings, including pedestrian

wind comfort (Blocken, 2009), wind-driven rain on building frontage (Briggen et al., 2009), pollutant dispersion (Hanna et al., 2006), exterior surface heat transfer (Blocken et al., 2009), natural ventilation and wind load of buildings (Cook et al., 2003). For both indoor and outdoor environment studies, the advances in computing performance and the development of efficient and powerful grid generation techniques and numerical solvers have led to the present situation in which CFD can technically be applied for study cases involving complex geometries and complex flow fields.

Numerical CFD modeling offers considerable advantages because it allows investigation where experimentation is not possible. It can provide a large amount of detail about a flow in the whole calculation domain, under varied conditions and without similarity constraints. The main limitations are the requirement of systematic and CFD solution verification and validation studies. The Navier-Stokes equations are commonly used to model the flow in the Atmospheric Boundary Layer (ABL) and the nature of the flow in an urban area, consisting of an arbitrary aggregation of buildings, is dominated by unsteady turbulent structures. Unfortunately, turbulent flow is one of the unsolved problems of classical physics. Despite many years of intensive research, a complete understanding of turbulent flow has not yet been attained (Davidson, 2004).

Several methods exist for predicting turbulent flows with CFD. Three most popular approaches are: Direct Numerical Simulation (DNS), Large Eddy Simulation (LES) and Reynolds-Averaged Navier-Stokes (RANS) simulation. The three approaches including the choice for our simulations have already been introduced in a previous work (see Milliez (2006) Chapter 2). Here, we just briefly present the advantages and weaknesses of each simulation approach.

Direct Numerical Simulation (DNS) DNS solves the exact Navier-Stokes equations by resolving all the scales of motion from the energetic large scales to the dissipative small scales, without any modeling. In consequence, DNS is expected to provide accurate predictions of the flow (Moin and Mahesh, 1998). However, the associated computational cost is extremely expensive in the case of urban flow problems. Indeed, the number of grid points required to simulate a 3D turbulent flow in DNS is proportional to $Re_L^{9/4}$, where Re_L is the Reynolds number based on the integral scale of the flow. Because the time step is related to the grid size, the total computational cost for DNS actually increases as Re_L^3. This rapid increase with Re_L

prohibits the application of DNS to high Reynolds number flows, such as the ones in the ABL. Despite of all progress in terms of computational power, DNS is still restricted to flows with low Reynolds numbers in relatively simple obstacles in urban areas because of the very large range of scales that have to be resolved (Coceal et al., 2007) .

Large Eddy Simulation (LES) The basic idea of LES is to solve 'filtered' Navier-Stokes equations, therefore to resolve only the large-scale motions in a turbulent flow and model the small-scale (unresolved) motions. The latter scales of motion are expected to be more universal and, hence, easier to model. Compared to DNS, LES is not an exact solution but is less computationally demanding. However, the application of LES to wall-bounded flows, particularly at high Reynolds numbers, is severely restricted owing to the grid resolution requirements for LES to resolve the viscous small-scale motions near the wall. Chapman (1979) estimated that the number of grid points needed for LES to resolve these near-wall small-scale motions is approximately proportional to $Re_L^{1.8}$. Several LES studies have been applied to study ABL flow and dispersion in urban areas (Kanda et al., 2004; Xie et al., 2008; Santiago et al., 2010). In spite of the fact that LES computations are feasible and more accurate than Reynolds-Averaged Navier-Stokes simulation (see next paragrah) but they are still very expensive.

Reynolds-Averaged Navier-Stokes simulation (RANS) As the name implies, the RANS approach solves the 'averaged' Navier-Stokes equations. In this approach, only the ensemble averaged flow properties are resolved with all other scales of eddies being modeled. The turbulent stresses required for the closure of the Reynolds-averaged momentum equation, known as the Reynolds stresses, represent the mean momentum fluxes induced by turbulence. The classical approach to model this term is to adopt the eddy viscosity concept originally proposed by Boussinesq (1877), which assumes a linear constitutive relationship between the turbulent stresses and the mean strain-rate tensors.

As additional equations, several types of turbulence models allow to obtain an estimate for the Reynolds stresses in the RANS equations: Mixing length model (Prandtl, 1925), $k-\varepsilon$ turbulence models (standard, renormalization group (RNG), realizable) (Launder and Spalding, 1974; Yakhot et al., 1992), $k-\omega$ turbulence models (Kato and Launder, 1993), Algebraic stress models (Baldwin and Lomax, 1978) and Reynolds stress models (Launder et al., 1975). The computational cost of RANS is independent of the Reynolds number, except for wall-

bounded flows where the number of grid points required in the near-wall region is proportional to $ln(Re_L)$ (Pope, 2000). Although RANS is less accurate, because of its computational efficiency, RANS is the most commonly used CFD methodology for the simulation of turbulent flows encountered in industrial and engineering applications. Note that there is no turbulence model that is universally valid. In our simulations, the turbulence is parameterized by the well known standard $k-\varepsilon$ closure.

2.1.1 Best practice guidelines

The accuracy of CFD is an important matter of concern. Care is required in the geometrical implementation of the model, in grid generation and in selecting proper solution set-up and parameters. Since a large number of choices needs to be made by the user in CFD simulations, some guidelines on industrial applications have been published in order to clarify the method for validation and verification of CFD results (e.g. ERCOFTAC (European Research Community on Fluids, Turbulence And Combustion) organizations' guidelines (Casey and Wintergerste, 2000)). In 2007, European Cooperation in Science and Technology (COST action 732 research group) (Franke et al., 2007) compiled a set of specific recommendations for the use of CFD in wind engineering from a detailed review of the literature. In 2008, a Working Group in the Architectural Institute of Japan (AIJ) (Tominaga et al., 2008), similar to COST 732, conducted extensive best practice advice for CFD prediction fo the pedestrian wind environment around buildings. These documents primarily focused on steady RANS simulations. Here, we briefly present some guidelines for CFD in urban aerodynamics which are mainly based on COST (Franke et al., 2007) and AIJ (Tominaga et al., 2008) recommendations.

2.1.1.a Error in CFD Simulations

In typical CFD simulations, different kinds of errors can have a very large impact on the results. Here we classify some sources of errors:

Physical modeling errors Physical modeling errors are due to uncertainties in the formulation and to deliberate simplifications of the model: for instance, the RANS equations in combination with a given turbulence model, the eddy viscosity model or Boussinesq hypothesis, use of specific constants in the $k-\varepsilon$ model, use of wall functions, modeling of the surface

roughness, simplifications of the geometry, etc. In general, physical modeling errors can be examined by performing validation studies that focus on certain phenomena (e.g. turbulent boundary layers).

Computer round-off errors Computer round-off errors develop with the representation of floating point numbers and the accuracy at which numbers are stored. With advanced computer resources, numbers are typically stored with 16, 32, or 64 bits. Computer round-off errors are not considered significant when compared with other errors. If they are suspected to be significant, one can perform a test by running the code at a higher precision. For simple flows, single precision runs (32 bit arithmetic) are usually adequate for convergence. In some more difficult cases, where there may be extremes of scales in the problem or very fine meshes, it can be required to use double precision (64 bit arithmetic). This will require more memory, but may not add a huge overhead on computational time, depending on the nature of the hardware being used. The computer numbering format in the CFD code *Code_Saturne* used in our simulations is double precision.

Iteration-convergence error This error is introduced because the iterative procedure to reach the steady state solution has to be stopped at a certain moment in time. The default values for convergence in most commercial codes are not strict because code vendors want to stress calculation efficiency. Therefore, stricter convergence criteria are required to check that there is no change in the solution. COST 732 (Franke et al., 2007) suggests that scaled residuals should drop by at least 4 orders of magnitude. AIJ (Tominaga et al., 2008) points that the suitable convergence values are largely dependent on flow configuration and boundary conditions, so it is better to check the solution directly using different convergence criteria. In our simulations with *Code_Saturne*, we keep a standard residual value (10^{-9}) and check the convergence of the solution with monitoring points.

Spatial and temporal discretization errors These errors are generated from representing the governing equations on a mesh that represents a discretized computational domain. For unsteady calculations also time discretization causes discretization errors. ERCOFTAC report (Casey and Wintergerste, 2000) indicates that the spatial and temporal discretization are probably the most crucial source of numerical errors. The COST 732 report (Franke et al., 2007)

advises that grid sensitivity analysis is a minimum requirement in a CFD simulation. In Section (2.1.2), we discuss in more detail the issues relative to the computational grid. To assess the influence of the time step on the results, a systematic reduction or increase of the time step should be made, and the simulation repeated. We investigate this point with the MUST experiment in Chapter 3. In advection dominated problems, the time step Δt (s) should satisfy the following criteria:

$$\Delta t = CFL\ \Delta x_{min}/U_{max} \tag{2.1}$$

where Δx_{min} (m) is the minimum grid width, U_{max} $(m\ s^{-1})$ is the maximum velocity and CFL is the Courant-Friedrichs-Lewy number (Courant et al., 1967). Choosing the minimum grid spacing and the maximum velocity makes this estimate conservative. The generally suggested criteria is that $CFL < 1$.

Besides the above mentioned errors, due to a lack of information about physical parameters used within the model, the influence of the unwise choice of these parameters can also lead to error on the results if the choice is inadequate (see the sensitivity study in Chapter 3).

Generally, many errors are made by CFD users because of lack of knowledge. As a result, simulation results can only be trusted or used if they have been performed on a mesh obtained by grid-sensitivity analysis, performed taking into account the proper guidelines that have been published in literature and carefully validated. Validation means systematically comparing CFD results with experiments to assess the performance of the physical modeling choices.

2.1.1.b Choice of the computational domain

The size of the entire computational domain in the vertical, lateral and flow directions depends on the area that shall be represented and on the boundary conditions that will be used. For urban areas with multiple buildings, both COST 732 (Franke et al., 2007) and AIJ (Tominaga et al., 2008) reports suggest that the top boundary should be set $5H_{max}$ or above the tallest building with height H_{max} (Fig. 2.1). The reason is that the large distances given above the obstacles are necessary to prevent an artificial acceleration of the flow over the buildings. After Franke et al. (2007), the lateral boundaries should be at a distance of $5H_{max}$ from the obstacles. Same distance should be set between the inlet boundary and the first building which allows for a fully developed flow (Fig. 2.1). The outflow boundary should be positioned at least $15H_{max}$ behind the last building to allow for flow re-development behind the wake region (Fig. 2.1). Similar

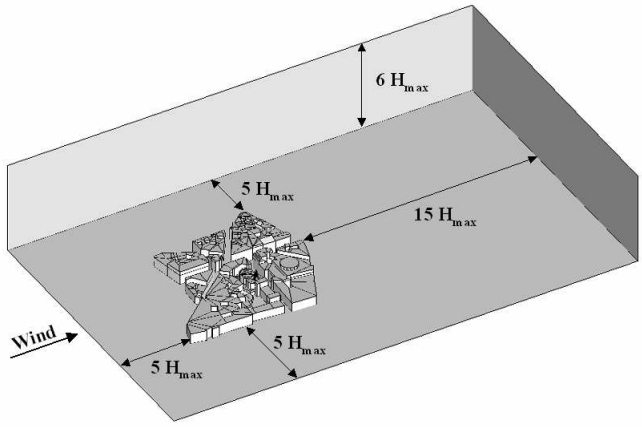

Figure 2.1: Recommended computational domain size where H_{max} refers the maximum height of the building, adapted after Franke et al. (2007) and Tominaga et al. (2008).

requirements for the lateral and the inlet boundaries were suggested by Tominaga et al. (2008). However, they report that there is a possibility of unrealistic results if the computational region is expanded without representation of surroundings, then the recommended outflow boundaries is at least $10H_{max}$.

2.1.1.c Initial and boundary conditions

Incorrect or inappropriate specification of initial or boundary conditions is a very common cause of errors. They may lead to the solution of the wrong problem as well as convergence difficulties.

Initial conditions Initial data and inflow data are very often chosen the same. This is a good starting point for most models. Initializing with the larger-scale field which is expected to be close to the final solution will reduce the computational efforts needed to reach stationary solutions. However, if these initial data are not close to the real initial conditions (e.g. wrong wind direction) then an accurate solution can not be expected. Since initial data are not known perfectly, but include uncertainties that result from lack of measurement or measurement inaccuracy, the initial input values are never perfectly known. Therefore Franke et al. (2007) advise to keep initial data uncertainty as little as possible and to keep in mind that the initial data influence the model results in unsteady simulations.

Inlet boundary conditions The proper choice of boundary conditions is very important. Since they represent the influence of the larger-scale surroundings and they determine to a large extent the solution inside the computational domain. At the inlet boundary, the mean velocity profile is often obtained from the academic logarithmic profile modeling the flow over the upwind terrain via the roughness length z_0 (m), or from the profiles of the wind tunnel simulations. In simulation of field experiments, available information from nearby meteorological stations is used to determine the wind speed U_{ref} $(m\ s^{-1})$ at a reference height z_{ref} (m) (Stull, 1988).

In the case the vertical distribution of turbulent energy $k(z)$ $(m^2\ s^{-2})$ is not available in the data set, Franke et al. (2007) assuming a constant friction velocity in ABL, suggest:

$$k(z) = \frac{U_{ABL}^{*2}}{\sqrt{C_\mu}}, \tag{2.2}$$

and the dissipation rate $\varepsilon(z)$ can be expressed as:

$$\varepsilon(z) = \frac{U_{ABL}^{*3}}{\kappa(z+z_0)}, \tag{2.3}$$

where U_{ABL}^{*} $(m\ s^{-1})$ represents the atmospheric boundary layer friction velocity, C_μ is a constant coefficient $(= 0.09)$, κ is the von Kármán constant $(= 0.4)$.

Nevertheless, Tominaga et al. (2008) point out that, in their recommendations, Franke et al. (2007) assume that the height of the computational domain is much lower than the atmospheric boundary layer height, since the assumption of a constant friction velocity is only valid in the lower part of the atmospheric boundary layer - surface boundary layer (Stull, 1988). Therefore, AIJ (Tominaga et al., 2008) proposes the following estimation equation between the vertical profile of turbulent intensity $I(z)$ and turbulent energy $k(z)$:

$$k(z) = I(z)^2 U(z)^2, \tag{2.4}$$

with

$$I(z) = 0.1\left(\frac{z}{z_G}\right)^{-\beta-0.05}, \tag{2.5}$$

where $U(z)$ is the vertical profile of velocity (ms^{-1}), z_G (m) is the boundary layer height and β is the power-law exponent. Both z_G and β are determined by terrain category (see Table 2.1),

Tominaga et al. (2008) also recommend that the values of the dissipation rate be given by assuming local equilibrium of production term for k equation. When the vertical gradient of

Table 2.1: Parameters determining $I(z)$; Modified after AIJ (2004); Category I: open, no significant obstruction, sea, lake; II: open, few obstructions, grassland, agricultural field; III: suburban, wooded terrain, few tall building (4 to 9-story); IV: city, tall buildings (4 to 9-story); V: city, heavy concentration of tall buildings (higher than 10-story).

Category	I	II	III	IV	V
z_G	250	350	450	550	650
β	0.1	0.15	0.2	0.27	0.35

velocity can be expressed by a power law with exponent β:

$$\varepsilon(z) = C_\mu^{1/2} k(z) \frac{U_{ref}}{z_{ref}} \beta \left(\frac{z}{z_{ref}}\right)^{\beta-1}. \tag{2.6}$$

Top boundary conditions AIJ (Tominaga et al., 2008) report that if the computational domain is large enough (Fig. 2.1), the boundary conditions for lateral and top boundaries do not have significant influences on the calculated results around the target buildings. However, the COST 732 (Franke et al., 2007) report stresses the importance of the choice of the top boundary condition and lateral boundary conditions. If symmetry boundary conditions are applied to the top boundary, these might enforce a parallel flow, by forcing the velocity component normal to the boundary to vanish. Furthermore, prescribing zero normal derivatives for all other flow variables may lead to a change from the inflow boundary profiles (which can have a non zero gradient at the height of the top of the domain). On the other hand, if the top boundary is handled as an outflow boundary, it can allow a normal velocity component at this boundary. In order to prevent a horizontal change from the inflow profiles, it is recommended to prescribe a constant shear stress (velocity gradient) at the top, corresponding to the inflow profiles. The latter option is taken in our simulations (see Chapter 5 and 6).

Lateral boundary conditions In the CFD codes, when the approach flow direction is parallel to the lateral boundaries, symmetry boundary conditions are frequently used at lateral boundaries. We use this option in an idealized case simulation (see Chapter 5). Franke et al. (2007) state that symmetry boundary conditions enforce a parallel flow by requiring a vanishing normal velocity component at the boundary. Therefore, the boundary should be positioned far

enough from the built-up area of interest in order not to lead to an artificial acceleration of the flow near the lateral boundaries (Fig. 2.1). In the case where different wind directions are to be simulated with the same computational domain, then the lateral boundaries become inflow or outflow boundaries. They are cases we present in Chapter 3 and 6.

Outlet boundary conditions At the boundary behind the obstacles (where all or most of the fluid leaves the computational domain), open boundary conditions are mostly used in CFD simulations. The open boundary conditions are either outflow or constant static pressure boundary conditions. We apply the outflow boundary conditions in our simulations. With an outflow boundary condition, the derivatives of all flow variables are forced to zero, corresponding to a fully developed flow. Franke et al. (2007) indicate that this boundary should be ideally far enough from the last building in order not to have any fluid re-entering into the computational domain. This also applies when using a constant static pressure at the outflow boundary, with the derivatives of all other flow variables forced to vanish. We note that imposed pressure at outlet is used in *Code_Saturne*.

Wall boundary conditions At solid walls, the no-slip boundary condition is used for the velocities. Franke et al. (2007) mention two different approaches to resolve the shear stress at smooth walls. The first one is the low-Reynolds number approach which resolves the viscous sublayer and computes the wall shear stress from the local velocity gradient normal to the wall. The equations for the turbulence quantities contain damping functions to reduce the influence of turbulence in this region dominated by molecular viscosity. The low-Reynolds number approach requires a very fine mesh resolution in the wall-normal direction. The first computational node should be positioned at a dimensionless wall distance z^+ given by:

$$z^+ = zu_*/\nu \approx 1, \tag{2.7}$$

where z (m) is the distance normal to the wall, ν ($m^2\ s^{-1}$) is the the kinematic viscosity and u_* ($m\ s^{-1}$) is the friction velocity, computed from the time averaged wall shear stress τ_w ($N\ m^{-2}$):

$$u_* = (\tau_w/\rho)^{1/2}, \tag{2.8}$$

with ρ ($kg\ m^{-3}$) the density.

To reduce the number of grid points in the wall-normal direction and therefore the computational costs, another approach called wall functions is applied as an alternative approach

to compute the wall shear stress. With the wall function approach, the wall shear stress is computed assuming a logarithmic velocity profile between the wall and the first computational node in the wall-normal direction. For the logarithmic profile to be valid, the first computational node should be placed at a dimensionless wall distance of z^+ between 30 and 500 for smooth walls. Also, for wall function modeling the turbulence quantities have to be modified at the first computational node. They are usually calculated assuming an equilibrium boundary layer, consistent with the logarithmic velocity profile. In spite of invalid in regions of flow separation, of reattachment and of strong pressure gradients and also unpredictable of the transition from laminar to turbulent boundary, the effect of wall functions on the solution away from the wall is however regarded as small in the built environment.

Furthermore, the wall function approach is also used for rough walls. Blocken et al. (2007) state different wall functions and demonstrate the importance of four basic requirements for CFD simulation of ABL flow with sand-grain wall functions. The four requirements are:

- a high mesh resolution in the vertical direction near the bottom of the computational domain,
- the horizontal homogeneity of ABL flow in the upstream and downstream region of the domain,
- a distance y_P (m) from the center point P of the wall-adjacent cell to the wall (bottom of the domain) that is larger than the physical roughness height k_S (m) of the terrain $(y_P > k_S)$,
- the relationship between the equivalent roughness height k_S and the corresponding aerodynamic roughness length z_0 (m).

In order to deal with the problem of the impossibility of simultaneously satisfying all four requirements in the k_s type wall functions for fully rough surfaces (i.e. standard wall functions modified for roughness based on experiments with sand-grain roughness), Blocken et al. (2007) consider that the best solution is to violate the third requirement $y_P > k_S$ and advise to assess the extent of horizontal inhomogeneity by a simulation in an empty computational domain prior to the simulation domain with obstacles. A roughness wall function is used in our simulations, and is presented in Section 2.3.5. We also apply the similar consideration to the thermal boundary

layer for heated walls. In this work, the dimensionless value z^+ is between 12.7 and 268 in Chapter 3 and 4, between 2.8 and 3.9 in Chapter 5, and between 0.2 and 14 in Chapter 6.

2.1.1.d Algorithmic Considerations

In order to be numerically solved, the basic equations have to be discretized and transformed into algebraic equations. For time-dependent problems, second-order methods should also be chosen for the approximation of the time derivatives. Higher order advection differencing schemes can lead to numerical oscillations that may cause poor convergence, or have quantities to overshoot. Running with first order upwind schemes may help to overcome this. However, it should be recalled that the spatial gradients of the transported quantities tend to become diffusive due to a large numerical viscosity of the upwind scheme. Both COST 732 (Franke et al., 2007) and AIJ (Tominaga et al., 2008) reports do not recommend the use of first-order methods like upwind scheme except in initial iterations.

In this research, I first performed the simulations which are presented in Chapter 3 with a center scheme. However, when the thermal effects are taken into account in a low wind speed case (Chapter 5), using a center scheme happens to create numerical instabilities, especially in the inflow region, thus an upwind scheme is used. We adopt the same choice for the simulation in Chapter 6.

2.1.2 Mesh issues

The discrete spatial domain (either for Finite-Difference, Finite-Volume or Finite-Element methods) is known as the mesh. Mesh generation is often considered as the most important and most time consuming part of CFD simulations. The quality of the mesh plays a direct role in the quality of the simulations, regardless of the flow solver used. Additionally, the solver will be more robust and efficient when using a well constructed mesh.

2.1.2.a Mesh classification

As CFD has developed, better algorithms and more computational power have become available, resulting in a diversification in solver techniques. One direct result of this development has been the expansion of available mesh elements and mesh connectivity (how cells are connected to one another). The elements in a mesh can be classified in various ways. Based on

the connectivity of the mesh, they can be classified: structured or unstructured. Structured grid generators are most commonly used when strict elemental alignment is mandated by the analysis code or is necessary to capture physical phenomenon. Unstructured mesh generation, on the other hand, relaxes the node valence requirement, allowing any number of elements to meet at a single node. *Code_Saturne* can work with both a structured grid and an unstructured mesh. Another mesh classification is based on the dimension and type of the elements. Common elements in 2D are triangles or rectangles, and common elements in 3D are tetrahedral or hexahedral. Here we briefly describe the types of meshes which are commonly used.

Hexahedral meshes Hexahedral meshes (either structured or unstructured grids) take their name from the fact that the mesh is characterized by a polyhedron with six faces. Although the element topology is fixed, the mesh can be shaped to be body fitted through stretching and twisting of the grid. Hexahedral meshes have the advantage of allowing a high degree of control. Indeed, hexahedral grids, which are very efficient at filling space, support a high degree of skewness and stretching before the solution is significantly affected. Also, the mesh can be flow-aligned, thereby yielding to greater accuracy of the solver. Hexahedral mesh flow solvers typically require lower amount of memory for a given mesh size and execute faster because they are optimized for the structured layout of the mesh. Lastly, post processing of the results on a hexahedral block mesh is typically a much easier task. Because the logical mesh planes make excellent reference points for examining the flow field and plotting the results.

Compared to tetrahedral meshes (see next paragraph), for the same cell count, hexahedral meshes will give more accurate solutions, especially if the grid lines are aligned with the flow. The major drawback of hexahedral meshes is the time and expertise required to lay out an optimal block structure for an entire model. Some complex geometries (see the CAPITOUL mesh in Chapter 6) are very hard even impossible to mesh with hexahedral block topologies. In these areas, the user is forced to stretch or twist the elements to a degree which drastically affects solver accuracy and performance. With the present computational power, mesh generation times are usually measured in hours if not days. We use this type of the mesh in the simple building geometry case (see Chapter 3 and 4 MUST mesh with about $55,000$ cells; Chapter 5 with about $253,000$ cells).

Tetrahedral meshes Tetrahedral meshes (always unstructured grids) are characterized by irregular connectivity which is not readily expressed as a three dimensional array in computer memory, but use an arbitrary collection of elements to fill the domain. Tetrahedral meshes can be stretched and twisted to fit the domain. These methods have the ability to be automated to a large degree. Given a good Computer-Aided Design (CAD) model, a good mesher can automatically place triangles on the surfaces and tetrahedral in the volume with very little input from the user. The advantage of tetrahedral mesh methods is that they are very automated and, therefore, require little user time or effort. And we do not need to worry about laying out block structure or connections. Mesh generation times are usually measured in minutes or hours.

The major drawback of tetrahedral meshes is the lack of user control when laying out the mesh. Typically any user involvement is limited to the boundaries of the mesh with the mesher automatically filling the interior. Triangle and tetrahedral elements have the problem that they do not stretch or twist well, therefore, the mesh is limited to being largely isotropic, i.e. all the elements have roughly the same size and shape. This is a major problem when trying to refine the mesh in a local area, often the entire mesh must be made much finer in order to get the point densities required locally. Another drawback of the methods is their reliance on good CAD data. Most meshing failures are due to some (possibly minuscule) error in the CAD model. Tetrahedral flow solvers typically require more memory and have longer execution times than structured hexahedral mesh solvers on a similar geometry. Post processing the solution on a tetrahedral mesh requires powerful tools for interpolating the results onto planes and surfaces of rotation for easier viewing. Since *Code_Saturne* accepts meshes with any type of cell and any type of grid structure and we have an available CAD data, we use this type of the mesh in CAPITOUL studies (see the CAPITOUL mesh in Chapter 6 with about 2 million cells).

Hybrid meshes A hybrid mesh is a mesh that contains hexahedral portions and tetrahedral portions. Hybrid meshes are designed to take advantage of the positive aspects of both hexahedral and tetrahedral meshes. They use some forms of hexahedral cells in local regions while using tetrahedral cells in the bulk of the domain. Hybrid meshes contain hexahedral, tetrahedral, prismatic, and pyramid elements in 3D and triangles and quadrilaterals in 2D. The various elements are used according to their strengths and weaknesses. Hexahedral elements are excellent near solid boundaries (where the gradients are high) and afford the user a high degree of control, but are time consuming to generate. Prismatic elements (usually triangles extruded

into wedges) are useful for resolving near wall gradients, but suffer from the fact that they are difficult to cluster in the lateral direction due to the underlying triangular structure. In almost all cases, tetrahedral elements are used to fill the remaining volume. Pyramid elements are used to transition from hexahedral elements to tetrahedral elements. Many codes try to automate the generation of prismatic meshes by allowing the user to define the surface mesh and then marching off the surface to create the 3D elements. While very useful and effective for smooth shapes, the extrusion process can break down near regions of high curvature or sharp discontinuities. The advantage of hybrid mesh methods is to control the shape and distribution of the grid locally, which can yield excellent meshes. The disadvantage is that they can be difficult to use and require user expertise in laying out the various grid locations and properties to get the best results. The generation of the hexahedral portions of the mesh will often fail due to complex geometry or user input errors. While the flow solver will use more resources than a structured hexahedral block code, it should be very similar to an unstructured tetrahedral code. Post processing the flow field solution on a hybrid grid suffers from the same disadvantages as a tetrahedral mesh. The time required for mesh generation is usually measured in hours or days.

2.1.2.b Choice of the computational mesh

With the Finite Volume, Finite Difference and Finite element methods the computational results depend crucially on the mesh that is used to discretise the computational domain. A high quality mesh should allow capturing the important physical phenomena like shear layers or vortices with sufficient resolution and no large errors introduced.

Geometrical representation of obstacles The level of details required for individual buildings or obstacles depends on their distance from the central area of interest. Franke et al. (2007) point out that the central area of interest should be reproduced with as much details as possible. This naturally increases the number of cells that are necessary to resolve the details. The available computational resources therefore limit the details which can be reproduced. Nevertheless, the numerical studies do not always require a very high degree of details. In our simulations, buildings will be represented as simple blocks (see Chapter 3, the MUST experiment or with more details in Chapter 6 the CAPITOUL experiment).

Mesh resolution When a global systematic mesh refinement is not possible due to resource limitations, at least a local mesh refinement should be used in the areas of interest. Grid stretching/compression should be small in regions of high gradients to keep the truncation error small. In these regions, both Franke et al. (2007) and Tominaga et al. (2008) advise an expansion ratio of 1.3 or less. Tominaga et al. (2008) suggest that the minimum grid resolution should be set to about $1/10$ of the building height scale (about 0.5 to 5.0 m) within the region including the evaluation points around the target building. Moreover, the evaluation height (1.5 to 5.0 m above ground) should be located at the third or higher grid cell from the ground surface. Franke et al. (2007) suggest that at least 10 cells should be used per building side and 10 cells per cube root of building volume as an initial choice. It is also recommended that pedestrian wind speeds at 1.5 to 2 m height should be calculated at the third or fourth cell above the ground. However, using only 5 cells per building side, our simulation results presented in Chapter 3 are still acceptable. For the results presented in Chapter 5 and 6, the simulations run on computer clusters, so we use at least 10 cells for the target building.

The mesh should be generated with consideration of such things as resolution, density, aspect ratio, stretching, orthogonality, grid singularities, and zonal boundary interfaces. However, the sensitivity of the results on the mesh resolution should be tested. Franke et al. (2007) and Tominaga et al. (2008) indicate that the number of fine meshes should be at least 1.5 times the number of coarse meshes in each dimension, and at least three refined meshes should be tested. Additionally, for the unstructured mesh, it is necessary to ensure that the aspect ratios do not become excessive in regions adjacent to coarse grids or near the surfaces of complex geometries. For improved accuracy, it is recommended to arrange the boundary layer elements (prismatic cells) parallel to the walls or the ground surfaces (Fig. 2). Both Franke et al. (2007) and Tominaga et al. (2008) introduce the same technique.

2.2 Review of some Urban Energy Balance Models

2.2.1 Urban Energy Balance Modeling

The behavior of the atmospheric Urban Canopy Layer (UCL) is the result of the interactions between atmospheric structures induced by the urban heterogeneities. One important feature of the UCL is the urban energy balance. The recent years, Surface Energy Balance (SEB)

models have evolved rapidly and increased in complexity, with increasing computer power and development of micrometeorological parameterizations.

A large number of models now exist with different assumptions about the important features of the surface and exchange processes that need to be incorporated. They can be classified into five categories, depending on the complexity of the parametrization, each one having its advantages and weaknesses (Masson, 2006; Milliez, 2006):

- Empirical models: this type of approach makes it possible to use extremely simple schemes. For instance, the Local-scale Urban Meteoro-logical Parameterization Scheme (LUMPS) (Grimmond and Oke, 2002) is a local-scale urban meteorological parameterization scheme capable of predicting the 1D spatial and temporal variability in heat fluxes in urban areas. Their main weakness is that they are based on statistics from field data, therefore they are limited to the range of conditions (land cover, climate, season, etc.) encountered in the original studies (Masson, 2006).

- Vegetation models without drag terms: this type of approach is based on the observation that roughness lengths and displacement heights are large over cities. Some refinement, depending on how the buildings are spatially organized, can be used to evaluate the roughness lengths. When coupled to an atmospheric model, the first atmospheric level is above the surface scheme, with all the friction located at this level. Grimmond and Oke (1999a) analyze the nature, sensitivity, and size of aerodynamic parameters obtained using morphometric methods, especially in the context of the physical structure of parts of North American cities.

- Vegetation models with drag terms: these models are derived from forest canopy parameterizations. A drag force is directly added in the equations of motions in the atmospheric model, up to the height of the highest buildings. For instance, reviewed Yamada's (1982) forest canopy parameterizations, Brown and Williams (1998) replace the fraction of the grid cell covered by trees with urban structures and use drag coefficients to incorporate the urban canopy parameterizations into a mesoscale code. Additional terms in the turbulence equation can also be taken into account. The main disadvantage of drag based schemes is that they imply direct modification of the equations of the atmospheric models to which they are coupled. A detailed urban and rural canopy parameterization developed inside the Penn State/NCAR Mesoscale Model (MM5) (Grell et al., 1994), DA-SM2-U

(Dupont et al., 2004) uses the drag-force approach to represent the dynamic and turbulent effects of the buildings and vegetation, and a modified version of the single layer scheme (see next paragraph), the Soil Model for Submesoscales, Urbanized Version (SM2-U) (Dupont et al., 2002; Dupont and Mestayer, 2006), to represent the thermodynamic effects of the canopy elements.

- Single layer schemes: in this approach, the exchanges between the surface and the atmosphere occur at the top of the canopy. This means that, when this scheme is coupled with an atmospheric model, the first level of the atmospheric model is located above the roof level. This has the advantage of simplicity and transferability. In this approach, the characteristics of the air in the canopy must be parametrized. Generally, the logarithmic law for wind is assumed above the top of the canopy, and an exponential law below. Air temperature and humidity are assumed to be uniform in the canyon. One of these models is SM2-U (Dupont et al., 2002; Dupont and Mestayer, 2006), includes a one-layer urban-and-vegetation canopy model to integrate the physical processes inside the urban canopy, such as heat exchanges, heat storage, radiation trapping, water interception, or surface water runoff, are integrated in a simple way (e.g. neither separated walls and roads energy budgets nor wind speed parameterization inside the canopy). Another example is the Town Energy Balance (TEB) scheme of Masson (2000). Although TEB is a simple approach with the use of only one roof, one generic wall and one generic road, it has been shown to reproduce accurately the SEB from regional to mesoscale and urban scales (Masson et al., 2002; Lemonsu et al., 2004).

- Mutlti-layer models: in these schemes, the wind and temperature are not uniform in the canopy, they depend on the interaction between the urban surfaces and the air at different levels in the roughness sub-layer. However, such a refinement is made at the cost of direct interaction with the atmospheric models because their equations are modified. Among these models, the Building Effect Parameterization model (Martilli et al., 2002) presents a high level of detail of the SEB, since any number of road and wall orientations are available, different building heights can be taken into account, and at each level of the wall intersecting an air level, there is a separate energy budget. This feature means this model is able to represent the differential heating of the wall when the sun is close to the horizon.

In addition, 3D models generally based on view factors calculation, compute for each urban sub-facet the incoming radiative fluxes and simple convection parameterization or coupled with CFD (e.g. SOLENE (Miguet and Groleau, 2002), TUF-3D (Krayenhoff and Voogt, 2007), DART (Gastellu-Etchegorry et al., 2004; Gastellu-Etchegorry, 2008). Some of them will be introduced in more details in Chapter 3.

In view of a wide range of urban energy balance models, it is not possible to single out one universal SEB model, which would be valid for all cases. However, a classification and a comparison of these models can be very helpful to identify the models for understanding the complexity required to model energy and water exchanges in urban areas. To do so, Grimmond et al. (2010, 2011) recently conducted an international Urban Energy Balance Models Comparison which we present in next section.

2.2.2 International Urban Energy Balance Models Comparison

Grimmond et al. (2010, 2011) conducted an international comparison of more than 30 models based on modeling the methodology and initial results with a same experimental data set. The fundamental requirement for the models to be included in this international comparison study is that they simulate urban energy balance fluxes. These schemes have varying levels of complexity, and model different fluxes. Table 2.2 refers to all the models (some models have different versions) involved in the international comparison study and Figure 2.2 illustrates the categories in which the different models were classified according to seven characteristics relating to: vegetation, anthropogenic heat flux, heat storage flux ΔQ_S, morphology, facets and orientations, reflection, albedo and emissivity. While all the models calculate the outgoing radiative fluxes $S^{\uparrow}$ and $L^{\uparrow}$, net all wave radiation Q^* and turbulent sensible heat flux Q_H, some do not model either turbulent latent heat flux Q_E or the additional sources of energy Q_F, and some model neither. It is noteworthy that some models solve the heat conduction equation using the force-restore method, while others solve the one-dimensional heat conduction equation. Both these two approaches have been implemented into our model (see section 2.3.4).

The evaluation of these models shows that they overall model accurately Q^*, while they are less capable of modeling Q_E. There is evidence that some classes of models perform better for individual fluxes but not overall. Typically, those that perform best during daytime do not perform best at night. For most models, the mean bias error (MBE) for sensible heat flux is

Table 2.2: Urban energy balance models with a given reference utilizing each model participating in the International Urban Balance Models Comparison Project. Modified after Grimmond et al. (2010)

Code	Model Name	References (e.g.)
BEP02	Building Effect Parameterization	Martilli et al. (2002)
BEP_BEM08	BEP coupled with Building Energy Model	Salamanca et al. (2009)
CLMU	Community Land Model - Urban	Oleson et al. (2008)
GCTTC	Green Cluster Thermal Time Constant model	Shashua-Bar and Hoffman (2004)
IISUCM	Institute of Industrial Science Urban Canopy Model	Kawamoto and Ooka (2009)
JULES	Joint UK Land Environment Simulator	Best et al. (2006)
LUMPS	Local-scale Urban Meteorological Parameterization Scheme	Offerle et al. (2003)
NKUA	University of Athens Model	Dandou et al. (2005)
MORUSES	Met Office Reading Urban Surface Exchange Scheme	Harman and Belcher (2004)
MUCM	Multi-layer Urban Canopy Model	Kondo et al. (2005)
NJU-UCM-S	Nanjing University Urban Canopy Model-single layer	Kusaka et al. (2001)
NJUC-UM-M	Nanjing University Urban Canopy Model-multiple layer	Kanda et al. (2005)
NSLUCM /NSLUCMK /NSLUCM-WRF	Noah land surface model/Single-layer Urban Canopy Model	Chen et al. (2009)
SM2U	Soil Model for Submesoscales (Urbanized)	Dupont and Mestayer (2006)
SNUUCM	Seoul National University Urban Canopy Model	Ryu et al. (2009)
SRUM2/SRUM4	Single Column Reading Urban Model tile version	Harman and Belcher (2006)
SUEB	Slab Urban Energy Balance Model	Fortuniak et al. (2005)
SUMM	Simple Urban Energy Balance Model for Mesoscale Simulation	Kawai et al. (2007)
TEB	Town Energy Balance	Masson (2000)
TEB07	Town Energy Balance	Hamdi and Masson (2008)
TUF2D	Temperatures of Urban Facets 2D	Krayenhoff and Voogt (2007)
TUF3D	Temperatures of Urban Facets 3D	Krayenhoff and Voogt (2007)
VUCM	Vegetated Urban Canopy Model	Lee and Park (2004)

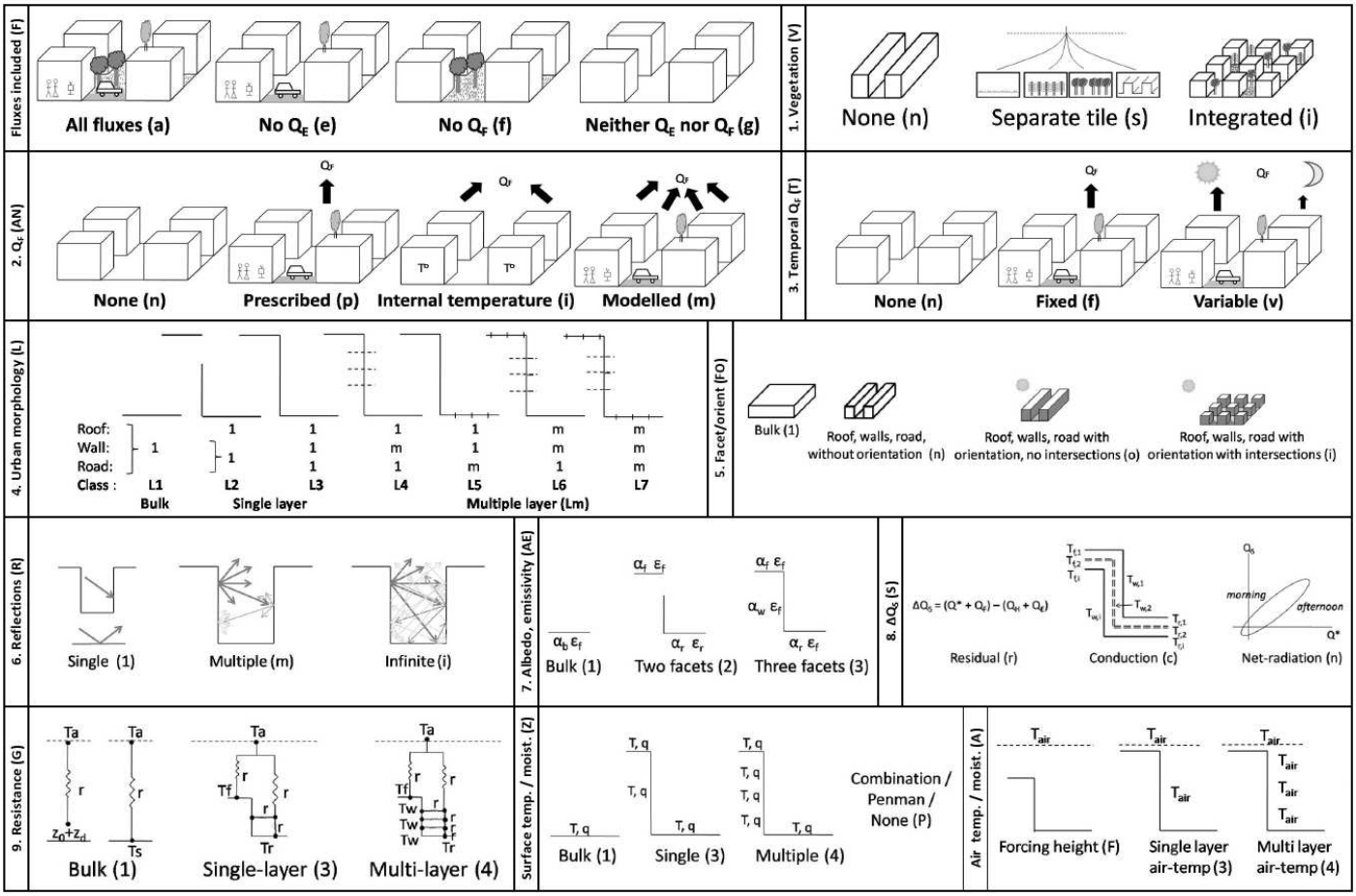

Figure 2.2: Model classifications in the International Urban Balance Models Comparison Project with their individual characteristics, after Grimmond et al. (2010).

positive, which might be explained by observational errors.

Some of the greatest differences in model performance are found between classes of model that treat vegetation and reflections differently. Some of the smallest differences relate to approaches used to calculate heat storage flux and urban morphology. Not including vegetation, even for a site with limited vegetation, results in the poorest performance for all fluxes during the day (in terms of the root mean square error (RMSE)) and for latent heat flux at night. In general, using a bulk albedo/emissivity results in better performance for all fluxes during the day.

Classifications show that no model include all the characteristics. In general, the simpler models perform as well as the more complex ones, based on all statistical measures, and no individual model performs best for all the fluxes. This finding has very significant implications for the applications of any model. It may also imply that, in some cases, models perform well but for the wrong physical reasons. For example, if a model overestimates the net short-wave radiation, but accurately models the sensible heat flux, it may indicate a problem in the physical representation of the heat exchanges between the surfaces and the atmosphere (since it needs to absorb more energy to get the right sensible heat flux).

When considering each individual characteristic, the models that best perform are those that are the simplest, since they need to assign only one parameter, which can be chosen close to the observed value. Considering all the characteristics together, the simplest and the most complex models have similar results and perform better than the medium complexity models. Additional surface information is important for improving model performance. Simpler models often show a net improvement with additional information; the more complex models do not. This may be because there was not enough additional detailed information provided, so it was more difficult for the users to decide how to properly use this information. It is expected that more complex models may have more potential for future improvements, as they are able to resolve more details without deteriorating their performance. The most complex models are more flexible and have the potential to describe the physical interactions between the atmosphere and the urban surfaces.

2.3 A new coupled radiative-dynamic 3D scheme in *Code_Saturne* for modeling urban areas

2.3.1 Choice of the model

Recent researches have sought to reconsider the problem of modeling the SEB, particularly to improve the modeling of the thermo-radiative and aerodynamic phenomena. For instance, in order to learn more about the impacts of different proportion of green area, Jesionek and Bruse (2003) developed a classification scheme for typical European urban building types and have simulated them systematically with the microscale climate model ENVI-met. The simulation results where analyzed primarily in view of thermal advantages and disadvantages of increased green area and its effects on pollution dispersion and accumulation. It is shown, that especially in densely build up block structures, greening with trees leads to higher pollution concentration, while in more open structures the thermal advantages of greening, due to shadow effects, can be fully used to improve of the microclimate. Chen et al. (2009) performed coupled simulations of convection, radiation and conduction to evaluate the outdoor thermal environment over different urban blocks, a high-rise area and a mid-rise area in the city of Tokyo in Japan, to compare the effects of measures such as the position of the heat release point of air-conditioning, greening, high surface albedo, and traffic volume. The results showed that the effectiveness of moderation countermeasures differed according to the configuration of the urban blocks. Bouyer (2009) presented the SOLENE-microclimate model including a soil model and a inner building thermal model, this last one allowing to compute the energy consumption of a building interacting with its urban environment. They are both integrated into the SOLENE (thermo-radiative simulation tool, see Chapter 4), then using the commercial CFD tool (Fluent) as a quasi-dynamic coupling to calculate the air temperature, mass concentrations of moisture and heat transfer coefficient. However, only the energy transport and moisture equations in the CFD tool are solved. Except for the initialization phase, the absence of resolution of momentum equations does not allow to take into account the movement of natural and mixed convection of the airflow in the canopy.

The present research aims to accurately simulate the atmosphere and surfaces in urban environments at microscale. The objective is to fully model the 3D airflow in the urban canopy in non neutral conditions and therefore to take into account atmospheric radiation and heat trans-

fers for complex geometries. A new 3D microscale radiative scheme has been previously implemented in the open-source CFD code *Code_Saturne*, described in details by Milliez (2006). As a full radiative-dynamic coupling, the model was evaluated with idealized cases, using as a first step, a constant 3D wind field (Milliez, 2006). In this section, we describe the main features of the model and some current improvements.

2.3.2 Presentation of the atmospheric module in *Code_Saturne*

Generality of *Code_Saturne* Developed by Électricité De France for laminar or turbulent flow, *Code_Saturne* is a CFD code which can handle complex geometry and complex physics (Archambeau et al., 2003). *Code_Saturne* solves the Navier-Stokes equations for 2D, 2D axisymmetric, or 3D, steady or unsteady, laminar or turbulent, incompressible or dilatable flows, with or without heat transfer, and with possible scalar fluctuations. Beside the atmospheric module, the code also includes a Lagrangian module, a semi-transparent radiation module, a gas combustion module, a coal combustion module, an electric module (Joule effect and electric arc) and a compressible module.

The code uses a Finite Volume discretization. A wide range of unstructured meshes, either hybrid (containing elements of different types) and/or non-conform, can be used. Within the framework of the Finite Volume approach, the numerical solver integrates the equations over each cell of the unstructured mesh. For RANS simulations, the time scheme is an implicit first order Euler approach. A fractional step scheme is used to solve the mass and momentum equations. The first step (predictor step) provides predicted velocity components: they are determined sequentially and without coupling between each other. The mass equation is taken into account during the second step (corrector step): a pressure Poisson equation is solved and the mass fluxes at the cell faces are updated.

Furthermore, the equations for the turbulent variables (turbulent kinetic energy and dissipation or Reynolds stresses and dissipation) are solved, using also the Euler approach. For the $k-\varepsilon$ model, an additional step is carried out to couple the source terms. Next, the equations for the scalars are solved, also with the Euler approach. Finally, all the variables are updated and another time step may start.

Specificity of the atmospheric module The atmospheric module is based on the former code *Mercure_Saturne* which was a peripheral version of *Code_Saturne* adapted for multi-scales at-

mospheric airflow (either neutral or stratified) and pollutant dispersion studies. Detailed described in Milliez and Carissimo (2007), the atmospheric module of *Code_Saturne* solves the Navier-Stokes equations for momentum and equations for additional scalars with an anelastic approximation (i.e. by filtering the acoustic waves while keeping an assumption of compressibility, by neglecting the variations in time of the density in the continuous equation). It can take into account larger scale meteorological conditions, by using a meteorological file that contains the wind velocity, turbulence kinetic energy, dissipation rate, and temperature profiles. As currently done in atmospheric models, the potential temperature is the thermodynamic variable in the energy conservation equation, which determines stratification effects on vertical turbulent transport and allows to estimate the surface-air thermal gradient that controls convective heat transfer. An ideal gas state equation is used to take into account the water vapor content.

Two turbulent approaches are available in the module, RANS and LES. As mentioned before, we choose the RANS approach with a $k-\varepsilon$ turbulence closure for our simulations. We stress that despite the fact that the $k-\varepsilon$ closure is generally unable to capture precisely the geometry dependent large eddies in many complex flows and overestimates the dissipated energy, it gives a fairly acceptable accuracy with a reasonable computational time for this research work.

The model can take into account the Coriolis effects, but in our simulations, we work at local scale and the Coriolis effects are neglected (i.e. the simulations are under large Rossby number conditions). In order to take into account the variation of density in the fluid, the Favre average is used in the model equations. For a variable v, the Favre average for RANS $\widetilde{v}$ and its fluctuation v' are defined as:

$$\widetilde{v} = \frac{\overline{\rho v}}{\overline{\rho}}, \; v' = v - \widetilde{v},$$

where $\overline{v}$ is the ensemble average.

The equations for mass, momentum and energy conservation that are solved in the atmo-

spheric module are:

$$\frac{\partial \overline{\rho}\widetilde{u_i}}{\partial x_i} = 0, \tag{2.9}$$

$$\overline{\rho}(\frac{\partial \widetilde{u_i}}{\partial t}+\widetilde{u_j}\frac{\partial \widetilde{u_i}}{\partial x_j}) = -\frac{\partial \widetilde{p}}{\partial x_i}+\frac{\partial}{\partial x_j}[\mu(\frac{\partial \widetilde{u_i}}{\partial x_j}+\frac{\partial \widetilde{u_j}}{\partial x_i})-\frac{2}{3}\mu\delta_{ij}\frac{\partial \widetilde{u_k}}{\partial x_k}] - \frac{\partial(\overline{\rho}\widetilde{u_i'u_j'})}{\partial x_j}+(\overline{\rho}-\rho_{ref})g_i, \tag{2.10}$$

$$\overline{\rho}(\frac{\partial \widetilde{\theta}}{\partial t}+\widetilde{u_j}\frac{\partial \widetilde{\theta}}{\partial x_j}) = \frac{\partial}{\partial x_j}(\frac{\lambda}{C_p}\frac{\partial \widetilde{\theta}}{\partial x_j})-\frac{\partial(\overline{\rho}\widetilde{\theta' u_j'})}{\partial x_j}+S_{rad}, \tag{2.11}$$

where u_i ($m\ s^{-1}$) is the speed for coordinate i, $\widetilde{p}$ (Pa) is the average pressure, μ ($kg\ m^{-1}s^{-1}$) is the viscosity of the fluid, g_i ($m\ s^{-2}$) the gravity for coordinate i, ρ ($kg\ m^{-3}$) the fluid density and ρ_{ref} ($kg\ m\ s^{-3}$) is the time dependent hydro-static reference state, λ ($W\ m^{-1}K^{-1}$) the thermal conductivity, θ (K) the potential temperature, C_p the specific heat capacity ($J\ kg^{-1}\ K^{-1}$) and S_{rad} ($J\ K\ m^{-5}s^{-1}$) an extra thermal source.

To close equations (2.9:2.11), the Favre-Reynolds stress and the heat flux are expressed according to Boussinesq's turbulent diffusivity model:

$$-\overline{\rho}\ \widetilde{u_i'u_j'} = \mu_t(\frac{\partial \widetilde{u_i}}{\partial x_j}+\frac{\partial \widetilde{u_j}}{\partial x_i})-\frac{2}{3}\mu_t\delta_{ij}\frac{\partial \widetilde{u_k}}{\partial x_k}-\overline{\rho}\ \frac{2}{3}\delta_{ij}k, \tag{2.12}$$

$$-\overline{\rho}\ \widetilde{\theta' u_j'} = \frac{\mu_t}{Pr_t}(\frac{\partial \widetilde{\theta}}{\partial x_j}), \tag{2.13}$$

with Pr_t the turbulent Prandtl number.

In the $k-\varepsilon$ model, μ_t is linked to the turbulent kinetic energy per unit mass k and the dissipation ε through:

$$\mu_t = C_\mu\overline{\rho}\frac{\widetilde{k}^2}{\varepsilon}, \tag{2.14}$$

with $C_\mu = 0.09$ as in Launder and Spalding (1974).

The equation for the turbulence and the dissipation are transport equations:

$$\overline{\rho}\left(\frac{\partial \widetilde{k}}{\partial t}+\widetilde{u_j}\frac{\partial \widetilde{k}}{\partial x_j}\right) = \frac{\partial}{\partial x_j}((\mu+\frac{\mu_t}{\sigma_k})\frac{\partial \widetilde{k}}{\partial x_j}) \tag{2.15}$$

$$+\widetilde{P}+\widetilde{G}-\overline{\rho}\varepsilon+S_k \tag{2.16}$$

$$\overline{\rho}\left(\frac{\partial \varepsilon}{\partial t}+\widetilde{u_j}\frac{\partial \varepsilon}{\partial x_j}\right) = \frac{\partial}{\partial x_j}((\mu+\frac{\mu_t}{\sigma_\varepsilon})\frac{\partial \varepsilon}{\partial x_j}) +C_{\varepsilon 1}\frac{\varepsilon}{k}(\widetilde{P}+C_{\varepsilon 3}\widetilde{G})-C_{\varepsilon 2}\ \overline{\rho}\frac{\varepsilon^2}{\widetilde{k}}+S_\varepsilon. \tag{2.17}$$

S_k and S_ε are extra source terms of turbulence and dissipation respectively that can be used for example in drag porosity models and $\widetilde{P}$ and $\widetilde{G}$ are respectively the production rate of k and the production or destruction rate due to buoyancy:

$$\widetilde{P} = -\overline{\rho}\,\widetilde{u_i'u_j'}\frac{\partial \widetilde{u_i}}{\partial x_j}, \tag{2.18}$$

$$\widetilde{G} = \frac{\mu_t}{Pr_t}\frac{1}{\overline{\theta}}\frac{\partial \overline{\theta}}{\partial x_j}g_j. \tag{2.19}$$

The parameters of the equation are: $\sigma_k = 1$, $\sigma_\varepsilon = 1.3$, $C_{\varepsilon 1} = 1.44$, $C_{\varepsilon 2} = 1.92$ and $C_{\varepsilon 3} = 0$ for a stable stratified atmosphere ($\widetilde{G} < 0$) and $C_{\varepsilon 3} = 1$ for an unstable stratified atmosphere ($\widetilde{G} > 0$).

2.3.3 3D Atmospheric Radiative model

In SEB models, different schemes have been developed to estimate the radiative balance (shading and trapping effect of the buildings). In a transparent media, numerous approaches employ the radiosity method (Krayenhoff and Voogt, 2007) to compute the radiative flux exchanges between any kinds of two surfaces by calculating the view factors or shape factors (sky-wall, wall-wall, sky-ground, wall-ground, ground-ground). Few approaches (Milliez, 2006; Gastellu-Etchegorry, 2008) estimate the radiative fluxes by solving the Radiation Transfer Equation (RTE). We compare in detail the two approaches in Chapter 4.

A radiative atmospheric model for flat homogeneous terrain is available in *Mercure_Saturne*. The principle of this model is described in detail in Stephens (1984), Musson-Genon (1993, 1994) and Milliez (2006). It solves the RTE for the short- and long-wave radiation on 1D vertical arrays. For applications in built-up areas, the basic idea for developing a new microscale 3D radiative atmospheric model was to meet the following requirements: explicitly resolve the buildings in 3D, accurately reproduce the complex urban morphology and easily couple the radiative scheme with the dynamic model (Milliez, 2006). Thus, adapting to the atmosphere a radiative heat transfer scheme available for complex geometry in *Code_Saturne*, a new atmospheric 3D radiative scheme was developed in *Code_Saturne* for the urban canopy (Milliez, 2006).

2.3.3.a Radiative Transfer Equation

The thermal radiation is an electromagnetic phenomenon for heat transfer. In a physical space discretized by the Finite Volume method, this means that each volume is not only in interaction with its direct neighbors but with all visible elements. An analytical solution of the equation describing the process of radiative transfer is not possible. However, numerical methods describing the radiative heat transfer have been developed fulfilling the main aim of computing the radiative source-term in the energy conservation equation. Assuming a gray non-diffusive semi-transparent media, the RTE can be written as follows (Douce and Méchitoua, 2003; Milliez, 2006):

$$div(I(\underline{x},\underline{D})\underline{D}) = -K_a(\underline{x})L(\underline{x},\underline{D}) + K_a(\underline{x})\sigma T_a^4(\underline{x})/\pi, \tag{2.20}$$

where $I(\underline{x},\underline{D})$ refers to the intensity of radiation at the location $(\underline{x})$ along the propagation direction with the vector $\underline{D}$, $K_a(\underline{x})$ is the absorption coefficient, $L(\underline{x},\underline{D})$ the monochromatic luminance ($W\ m^{-3}\ sr^{-1}$), σ the Stefan-Boltzmann constant ($5.66703 \times 10^{-8}\ W\ m^{-2}\ K^{-4}$) and T_a the air temperature (K). In a semi-transparent media, I ($W\ m^{-3}\ sr^{-1}$) and K_a can be considered independent of the wave length and are integrated over the spectrum.

The radiative heating rate q_{rad} ($W\ m^{-3}$) is given by:

$$q_{rad}(\underline{x}) = -div \int_0^{4\pi} I(\underline{x},\underline{D})\underline{D}d\Omega, \tag{2.21}$$

where $d\Omega$ represents the element of the solid angle (sr) around the direction $\underline{D}$.

Boundary Conditions For a solid surface, the outgoing long-wave radiative flux $L^{\uparrow}$ ($W\ m^{-2}$) at a location $\underline{x}$ is composed of a reflected and emitted part under the assumption of a gray, diffusive radiation of the surface. The boundary condition for a surface is given by:

$$L^{\uparrow}(\underline{x}) = \frac{\varepsilon\sigma T_{sfc}^4}{\pi} + \frac{1-\varepsilon}{\pi}\int_{\Omega=0}^{2\pi} I(\underline{x},\underline{D}) \mid \underline{D}.\underline{n} \mid d\Omega, \tag{2.22}$$

with ε the emissivity of the surface, T_{sfc} (K) the surface temperature.

Numerical methods The equation governing radiative transfer is of an integro-differential type. Some methods such as the zone method and the Monte Carlo method, may be excessively computing-time demanding and therefore currently not suitable for simulation of fluid flow, chemical reactions and heat transfer in large simulation domains. Approximate and rapid solution methods combining accuracy and computational efficiency are preferred especially for

3D simulations. To resolve the RTE, there are in general two different kinds of approximate numerical approaches: ray-tracing and differential methods. The essential difference of these two groups are the directions in which the transport equations are formulated.

- Ray-tracing method: 1D equations along a multitude of individual rays through the computational domain are solved. The formulation of the equations is made along straight, arbitrarily oriented rays, which are not inevitably aligned with the coordinate system of the fluid flow. Determining all traces of the rays and cells located along its way requires either a lot of computational time or a lot of memory. In addition, the vectorization and parallelization of the algorithms of ray-tracing radiation models is limited due to the different lengths of the individual rays (Knaus et al., 1997).

- Differential Methods: They are tools to transform the equation of radiative transfer (Eq. 2.20) into a set of partial differential equations which can be formulated in the Cartesian coordinate system of the fluid flow. After discretizing the equation with the Finite-Volume method, a fast iterative sparse matrix solvers can be used to compute the solution, and the code for the differential radiation models can effectively be vectorized without significant increase of memory. One of the differential methods is the Discrete Ordinates Method (DOM) (Fiveland, 1984; Truelove, 1987; Liu et al., 2000) which is used in our radiative model.

2.3.3.b Discrete Ordinates Method (DOM)

In the Discrete Ordinates Method, the radiative transport equation is solved for a set of n discrete directions (e.g. 32 or 128 in our model). Each direction is associated with a solid angle in which the intensity is assumed to be constant. All solid angles are non-overlapping and spanning the total angle range of 4π. The integrals over the direction are replaced by numerical quadrature summed over each ordinate. Thus, the RTE (Eq. 2.20) can be transformed into a set of partial differential equations which can be approximated by a set of differential equation. The quadrature weights are determined by an approximation, in which the number of ordinates is calculated by n^2+2n. Each direction is fixed by its direction cosines. The source term of the energy conservation equation can be computed from the difference of the intensities in all directions multiplied by the weights at the cell centers and the emissivity.

In the microscale, we assume that the atmosphere is not diffusive. In fact, the angular

discretization and the small number of directions make the DOM less accurate than view factor models. To illustrate this, in Chapter 4, we discuss the advantages and weaknesses of using DOM in our radiative model through a comparison with SOLENE model (Miguet and Groleau, 2002) which uses the calculation of view factors or form factors. We adapted the model to atmospheric radiation. Both short- and long-wave radiation are taken into account separately. For the short-wave radiation, we distinguish direct and diffuse solar fluxes. We note that the new radiative scheme is, initially, designed to be applied in the urban canopy. Consideration of the upper part of the atmosphere is then taken into account by the boundary conditions at the top of our domain. Section 2.3.3.c and 2.3.3.d present the simple models for upper boundary conditions when data are not available and when not coupled with the 1D radiative model of *Mercure_Saturne*.

2.3.3.c Global solar radiation model

When solar rays pass through the atmosphere, there are five main types of radiation-damping processes: Rayleigh scattering, diffusion by aerosols, absorption by ozone, water vapor absorption/diffusion and uniformly-mixed gas absorption. The model we use to evaluate the incoming global solar radiative flux is based on the Bird Clear Sky model (Bird and Hulstrom, 1981) and METSTAT model (Maxwell, 1998). The latter one is used to provide the solar radiation data for the United States.

In clear sky conditions, the direct normal solar flux S_{Dn} ($W\ m^{-2}$) is obtained as:

$$S_{Dn} = CS_0\tau_r\tau_a\tau_{oz}\tau_{aw}\tau_g, \tag{2.23}$$

where coefficient $C = 0.9751$ from METSTAT, $S_0 = 1370(W\ m^{-2})$ is the solar constant, τ_r the transmittance due to Rayleigh diffusion, τ_a the transmittance due to aerosol absorption and scattering, τ_{oz} the transmittance due to ozone absorption, τ_{aw} the transmittance due to water vapor absorption and τ_g the transmittance due to mixed gas absorption.

The solar diffusion flux by the atmosphere is considered to be isotropic and can be expressed with three terms: Rayleigh diffusion S_{dr} ($W\ m^{-2}$), aerosol diffusion S_{dae} ($W\ m^{-2}$) and reflection by the surface S_{dg} ($W\ m^{-2}$). Each term can be estimated by:

$$S_{dr} = 0.79S_0cos(Z)\tau_r\tau_{aa}\tau_{oz}\tau_{aw}\tau_g(1-\tau_r)\frac{0.5}{1-m+m^{1.02}}, \tag{2.24}$$

$$S_{dae} = 0.79S_0cos(Z)\tau_r\tau_a\tau_{oz}\tau_{aw}\tau_g(1-\tau_{ad})\frac{F_c}{1-m+m^{1.02}}, \tag{2.25}$$

$$S_{dg} = (S_{Dn}cos(Z) + S_{dr} + S_{ae})\frac{\alpha_g \alpha_s}{1 - \alpha_g \alpha_s}, \tag{2.26}$$

with Z (rad) the sun zenith angle, τ_{aa} and τ_{ad} are respectively the transmittance due to aerosol absorption and scattering, m air mass $(kg\ m^{-3})$ and F_c the ratio of the forward-scattered irradiance to the total scattered irradiance due to aerosols, α_g averaged ground albedo, α_s clear sky or atmospheric albedo.

All above expressions are in accordance with Milliez (2006). In this work, I made the following modifications. First, proposed by Yang et al. (2001), a different expression for the air mass is used:

$$m = (1 - 0.0001 z_g)/[sin(h) + 0.15(57.296h + 3.885)^{-1.253}], \tag{2.27}$$

where z_g (m) is ground level and h (rad) is the altitude angle of the sun.

Secondly, in equation 2.24, the expression of the transmittance due to aerosol absorption τ_{aa} is

$$\tau_{aa} = 1 - E_1(1 - m + m^{1.06})(1 - \tau_a), \tag{2.28}$$

with E_1 the constant used in the Bird model associated with aerosol absorption. After testing, I took the values of $F_c = 0.84$ and $E_1 = 0.1$ as in Bird and Hulstrom (1981) are more appropriate for our simulations than other suggested values.

2.3.3.d Incident long-wave radiation model

In the simulations presented in this thesis, the incident long-wave radiation is directly taken from the observed values. In the case where the measurement is not available, $L^{\downarrow}$ $(W\ m^{-2})$ is generally expressed in terms of the Stefan-Boltzmann Law:

$$L^{\downarrow} = \varepsilon_{atm} \sigma T_{atm}^4 = \varepsilon_{clr} F \sigma T_{atm}^4, \tag{2.29}$$

where $\varepsilon_{atm} = \varepsilon_{clr} F$ is referred to as the effective or apparent emissivity and generally varies between roughly 0.7 for clear skies to close to unity for completely overcast skies, with ε_{clr} the clear-sky atmospheric emissivity. F (always ≥ 1) is a cloud factor expressing the increase in clear-sky $L^{\downarrow}$ due to cloud emission, and T_{atm} (K) is the effective atmospheric temperature.

The simple model implemented in *Code_Saturne* is after by Prata (1996): T_{atm} is approximated by the air temperature T_a at reference height close to the surface, and ε_{clr} is estimated by:

$$\varepsilon_{clr} = 1 - [1 + w\ exp(-(1.2 + 3w)^{0.5})] \tag{2.30}$$

where the precipitation water content w equals $46(e_a/T_a)$ with e_a (Pa) the water vapor pressure.

2.3.4 Surface temperature models

The surface temperature T_{sfc} (K) is a key control for energy exchanges at the urban surfaces, particularly for the net long-wave radiation and turbulent energy fluxes. The surface temperature is controlled by the balance between the external net fluxes and the conductive heat flux through the wall, from the building inside to the outside. As a first step in our development, a simple surface temperature model, the force-restore approach (Deardorf, 1978) has previously been implemented in *Code_Saturne* by Milliez (2006). Because of the limiting hypotheses of this approach (more adapted for the soil model and does not explicitly take into account the conduction) and in order to more accurately calculate the surface temperature of buildings, I additionally test in this work a 1D surface temperature approach, called hereafter the wall thermal model. Thus, the surface temperature in the simulations is computed from either the force-restore scheme or the wall thermal scheme. In this section, we briefly describe these two approaches. A comparison of these two surface temperature models with simulation results and observation data is presented in Chapter 3. Actually, a hybrid approach taking the advantages of both the force-restore method and wall thermal scheme has also been tested at the end of this work (see Chapter 6).

2.3.4.a The Force-restore method

The force-restore approach (Deardorf, 1978) is commonly used in order to calculate the ground temperature in atmospheric models and is considered a very useful tool. In this approach, a prognostic equation for temperature is used to reproduce the response to periodic heating of the soil. The model is based on an analytical solution of a two-layer decomposition of a material considered homogeneous. The deep soil temperature calculation appears in the restore term of the force-restore equation. This model has been extended to urban surfaces (Johnson et al., 1991; Dupont and Mestayer, 2006). Hence, the prediction of the surface temperature is made by using following equation:

$$\frac{\partial T_{sfc}}{\partial t} = \frac{\sqrt{2\omega}}{\mu_t}(L^* + S^* - Q_H) - \omega(T_{sfc} - T_{g/b}) \tag{2.31}$$

where ω (Hz) is the Earth angular frequency, L^* ($W\ m^{-2}$), S^* ($W\ m^{-2}$), Q_H ($W\ m^{-2}$) are respectively net long-wave, net short-wave, and sensible heat flux, μ_t ($J\ m^{-2}\ s^{-0.5}\ K^{-1}$) the

thermal admittance and $T_{g/b}$ (K) either deep soil or internal building temperature.

This extension nevertheless supposes well insulated buildings with a nearly constant internal temperature and homogeneous material.

2.3.4.b Wall thermal model

Neglecting the anthropogenic flux and the latent heat flux terms, the simplified energy balance can read as:

$$Q_{cond} + Q_H = L^* + S^*, \tag{2.32}$$

with Q_{cond} $(W\ m^{-2})$ the conduction heat flux between the building and the underlying ground including net change of energy storage by the building materials and the the enclosed air volume.

1D conduction within the patch substrate is bounded by surface energy exchanges at the patch surface and by the internal building energy exchanges or a deep-soil temperature at the substrate base. In the hypothesis of a single layer to express the conduction term, equation 2.32 reads after expression of each term:

$$\frac{\lambda}{e}(T_{sfc} - T_{int}) + h_f(T_{sfc} - T_a) = \varepsilon(L_a + L_e - \sigma T_{sfc}^4) + (1-\alpha)(S_D + S_f + S_e) \tag{2.33}$$

where λ $(W\ K^{-1}\ m^{-1})$ is the average thermal conductivity of the wall [1], e (m) the thickness of the wall, T_{int} (K) the internal building or deep soil temperature, h_f $(W\ m^{-2}\ K^{-1})$ the heat transfer coefficient calculated from equation 2.36 and T_a the external air temperature (K).

2.3.4.c Internal building temperature model

In the previous work (Milliez, 2006), the internal building temperature was set to the constant value and computed by averaging the diurnal temperatures of all the building surfaces. However, in some cases, such as that the building is not well insulated; the variation of the internal building temperature can be important and may have a significant impact on the surface temperature (see Chapter 3). In fact, this variation may also depend on building's solarization, levels of inertia and air permeability. Moreover, the internal temperature is rarely measured in the experiment. Its variation may be characterized as compared to the outside surface temperature

[1] The average thermal conductivity is the notion for the one-layer wall model. For a multi-layer wall model, the notion of the equivalent conductivity or conductance $(W\ K^{-1})$ is more appropriate.

by three parameters: the mean value, amplitude and phase-change. In order to more accurately model the internal temperature and take into account its variation, in this work it is computed with an incremental-adjustment method modified after Masson et al. (2002) and similarly used by Krayenhoff and Voogt (2007):

$$T_{int}^{n+1} = T_{int}^{n-1}(\frac{\tau - \Delta\, t}{\tau}) + \overline{T}(\frac{\Delta t}{\tau}), \tag{2.34}$$

where T_{int}^{n+1} (K) and T_{int}^{n-1} (K) are the computed internal temperatures at the following and previous time step respectively, Δt is the time step (s), τ (s) refers to the number of seconds in a day, and $\overline{T}$ (K) is the average over all the outside building surface temperatures computed at time step n (MUST case in Chapter 3 and 4) or is set one by one surface temperature (CAPITOUL case in Chapter 6). For a diurnal simulation, the initialized internal temperature value can be considered as same as the initialized outside surface temperature (e.g. T_{sfc} at midnight) or the outside surface temperature at half hour ago if the observation data is available (MUST and CAPITOUL case).

A potential improvement would involve accounting for the full internal building energy balance proposed by Mills (1997) and also used in SOLENE (Miguet and Groleau, 2002), but is not included at present. In order to improve the results, we can replace in Eq.2.34 $\overline{T}$ from the calculation with the average of the measured outside surface temperatures, if available. The latter is included as a user-controlled option in our model.

A plot of internal temperature modeled by three methods in a building results in a diurnal variation profile is shown in Figure 2.3. We should note that the extrapolation of the internal temperature profile using evolution equation (red dashed line in Fig. 2.3) might be different in our simulation because $\overline{T}$ also depends on the resolution of the mesh. It should also be noted that a constant internal building temperature (blue line in Fig. 2.3) effectively represents the inclusion of an anthropogenic heating term when the external air is cooler than the interior one (Arnfield, 2003). On the other hand, it is an artificial heat sink when the external air is warmer than the building interior. In fact, the mean building outside surface temperatures are quite sensitive to the internal building temperature evolution, both in terms of magnitude and time-evolution of the diurnal pattern. I will further discuss this point in Chapter 3.

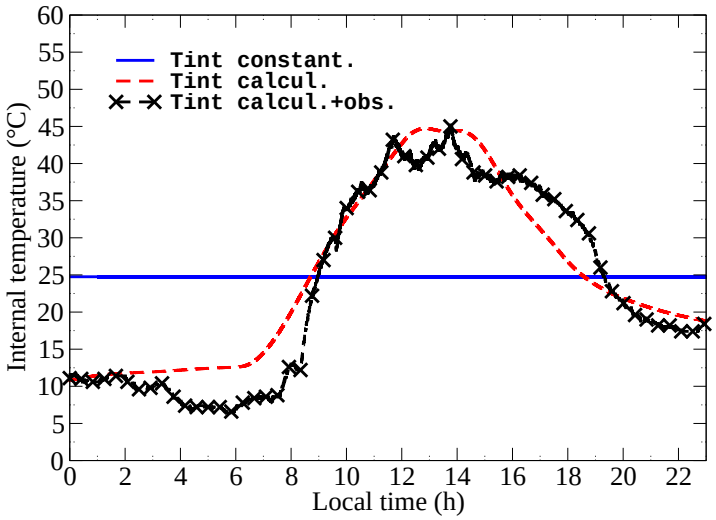

Figure 2.3: Different methods to model the internal building temperature T_{int} (°C) (Tint constant.: taking a constant value; Tint calcul.: using evolution equation; Tint calcul.+obs.: using evolution equation and taking the average outside building surface temperature from the measurements for $\overline{T}$.

2.3.4.d Brightness temperature

Many comparisons with observations are made in terms of brightness surface temperatures since it is the quantity measured by infrared thermometers (IRT) whilst model-calculated surface temperatures result from the solution of the surface energy balance (see Chapter 6). Brightness surface temperatures account for the surface emissivity and multiple reflections (together, effective emissivity) that are inherent in the observations. Surface brightness temperature (T_{br} (K)) is defined as the temperature that yields to an emitted broadband thermal radiance equivalent to the sum of the true broadband emitted radiance (with reduction due to gray body emissivity) and the broadband reflected radiance (after multiple reflections on canyon surfaces) (Krayenhoff and Voogt, 2007; Moscicki, 2007; Hénon, 2008):

$$T_{br} = \sqrt[4]{\varepsilon T_{sfc}^4 + \frac{(1-\varepsilon)L^{\downarrow}}{\sigma}}. \tag{2.35}$$

2.3.5 Convection model

The surface convective heat flux must be computed to both solve the surface energy balance (Eq.1.7) and determine the surface-air thermal gradient and therefore turbulent transport. In *Code_Saturne*, the convective heat transfer is computed in 3D for each surface patch. The buildings are explicitly defined in our simulations. Therefore, the detailed representation of the surface allows for a more complex 3D spatial representation of wind speed, turbulence, and temperature than simple canopy averages or vertical profiles. We use a rough wall boundary condition, based on the logarithmic law modified by the stratification. Usually these modified laws are based on the Monin-Obukov similarity but are implicit and therefore need to be solved iteratively. Here we use an explicit approach based on the work of Louis (1979) and described in Musson-Genon et al. (2007).

The heat transfer coefficient h_f in Eq.1.7 is computed for each solid sub-facet, depending on the local friction velocity u_* ($m\ s^{-1}$):

$$h_f = \frac{\rho C_p u_* \kappa f_h}{\sigma_t ln(\frac{d+z_0}{z_{0_T}})\sqrt{f_m}}, \tag{2.36}$$

where C_p is specific heat ($J\ kg^{-1}\ K^{-1}$), u_* is the friction velocity, κ is von Kármán constant, σ_t the turbulent Prandtl number, d (m) is the distance of the cell center to the wall, z_0 the roughness length (m), z_{0_T} the thermal roughness length (m), f_m and f_h are the Louis (1979) stability functions which take a value of 1 for neutral conditions. For vertical walls, the neutral conditions are applied.

In Chapter 3, I discuss different approaches to model the heat transfer coefficient.

CHAPTER 3

Micrometeorological modeling of radiative and convective effects with a building resolving code: published in Journal of Applied Meteorology and Climatology, 50 (8) (2011), 1713–1724

In the previous chapter, we introduced the new coupled radiative-dynamic 3D scheme in *Code_Saturne*. To ensure modeling accuracy, validating the model results with experimental data is necessary. The paper presented here shows the first evaluation of the coupling with data from the Mock Urban Setting Test (MUST) field experiment. In MUST, the buildings are idealized by an array of shipping containers. We have simulated a moderate wind speed day by modeling a detailed flow field. The simulations results showed a significant impact of the convective flux on the surface temperatures. Furthermore, the discussion about the comparison of three schemes of increasing complexity for predicting surface sensible heat flux also emphasize the contribution of modeling the detailed flow field.

Micrometeorological Modeling of Radiative and Convective Effects with a Building-Resolving Code

YONGFENG QU, MAYA MILLIEZ, LUC MUSSON-GENON, AND BERTRAND CARISSIMO

Teaching and Research Center in Atmospheric Environment (CEREA), Champs-sur-Marne, France

(Manuscript received 10 August 2010, in final form 14 March 2011)

ABSTRACT

In many micrometeorological studies with computational fluid dynamics, building-resolving models usually assume a neutral atmosphere. Nevertheless, urban radiative transfers play an important role because of their influence on the energy budget. To take into account atmospheric radiation and the thermal effects of the buildings in simulations of atmospheric flow and pollutant dispersion in urban areas, a three-dimensional (3D) atmospheric radiative scheme has been developed in the atmospheric module of the Code_Saturne 3D computational fluid dynamic model. On the basis of the discrete ordinate method, the radiative model solves the radiative transfer equation in a semitransparent medium for complex geometries. The spatial mesh discretization is the same as the one used for the dynamics. This paper describes ongoing work with the development of this model. The radiative scheme was previously validated with idealized cases. Here, results of the full coupling of the radiative and thermal schemes with the 3D dynamical model are presented and are compared with measurements from the Mock Urban Setting Test (MUST) and with simpler modeling approaches found in the literature. The model is able to globally reproduce the differences in diurnal evolution of the surface temperatures of the different walls and roof. The inhomogeneous wall temperature is only seen when using the 3D dynamical model for the convective scheme.

1. Introduction

Interest in urban climatology has increased in the past decade. It corresponds to the thermal and dynamical airflow response to the urban system solicitations, resulting in radiative transfers and convective exchanges within the urban air and with the building walls (Grimmond and Oke 1999; Arnfield 2003). In the past few years, numerical studies have been conducted to solve the surface energy balance (SEB) in urban canopies, with different degrees of simplification, using either an integrated representation of the urban canopy (Masson 2000) or a three-dimensional approach (Mills 1996; Miguet and Groleau 2002; Kanda et al. 2005; Krayenhoff and Voogt 2007; Gastellu-Etchegorry 2008; Asawa et al. 2008). Those models share the following parameterizations in their design: the schemes possess separate energy budgets for roofs, roads, and walls; radiative interactions between roads and walls are explicitly treated.

The Town Energy Balance (TEB) scheme of Masson (2000) consists of a facet-averaged scheme with one generic roof, one generic wall, and one generic road. The advantage of the integrated resolution is that few individual SEBs need to be resolved and therefore computation time is kept low, with a simple approach to model the inner-canopy wind flow. TEB has been shown to reproduce accurately the SEB from regional to mesoscale and urban scales (Masson et al. 2002; Lemonsu et al. 2004). Mills (1996) developed the Urban Canopy-Layer Climate Model, which has a detailed representation of the canyon with a highly simplified wind parameterization. The "SOLENE" (Miguet and Groleau 2002) and 3D-Computer Aided Design (Asawa et al. 2008) models are based on a realistic description of the canopy structure using a geometrical 3D surface model assigning radiative and thermal properties to each subfacet of the model and a constant transfer coefficient for each class of elements. The model is originally designed for simulating sunshade, natural lighting, and heat transfers for architectural purposes. The Discrete Anisotropic Radiative Transfer (DART) model (Gastellu-Etchegorry et al. 2004) simulates the radiative transfer in the whole optical domain simultaneously in the atmosphere and in

Corresponding author address: Yongfeng Qu, Teaching and Research Center in Atmospheric Environment (CEREA) (ENPC/EDF R&D), 6–8 avenue Blaise Pascal, 77455 Champs-sur-Marne, France. E-mail: yongfeng.qu@cerea.enpc.fr

DOI: 10.1175/2011JAMC2620.1

the urban and vegetated landscapes, with or without topography. A major feature of DART is that it can simulate images in the plane of the sensor, for different altitudes from the bottom to the top of the atmosphere. The new version of the DART model, DART-EB, (Gastellu-Etchegorry 2008) includes an energy balance component. In the case of urban canopies, turbulent fluxes and conduction are computed with classical boundary layer laws, using the equations of the TEB model (Masson 2000). The Simple Urban Energy Balance Model for Mesoscale Simulations (SUMM; Kanda et al. 2005), which represents the urban canopy with an infinitely extended regular array of uniform buildings, is more adapted for the mesoscale. The Temperatures of Urban Facets in 3D (TUF-3D) model (Krayenhoff and Voogt 2007) uses the radiosity approach based on interpatch view factors to model radiative exchange between the identical square patches that compose the simplified 3D urban geometry. An exponential inner-canopy wind speed profile is employed. TUF-3D has applications in both surface temperature distributions and thermal remote sensing anisotropy at several scales.

Previously described models have all put a strong emphasis on radiative exchanges but not on a detailed flow field. In this work, in addition to the above applications, we are also interested in applying the model to pollutant dispersion in low–wind speed conditions, when the thermal effects have a strong influence on the flow.

To model the airflow in the urban canopy in nonneutral conditions more accurately and to take into account the 3D convective exchanges, we developed a 3D microscale radiative model coupled with a 3D computational fluid dynamics (CFD) code for complex geometries to simulate dynamics and thermodynamics of the urban atmosphere (Milliez 2006). Differing from other radiative models that calculate the view factors to estimate the incoming radiative fluxes on urban surfaces, our model directly solves the 3D radiative transfer equation in the whole fluid domain. This approach allows us to determine the radiation flux not only on the facets of the urban landscape but also in each fluid grid cell between the buildings. The difference could become important in the case of smoke or fog between the buildings. The model was evaluated with idealized cases, using as a first step a constant 3D wind field (Milliez et al. 2006). The purpose of the work presented here is to study the full radiative–dynamical coupling, using an evolving 3D flow field. First we present the model, and then we discuss in detail the results of the full coupling. We further discuss the influence on the surface temperature of the internal building temperature and the wall thermal modeling, comparing the 3D resolution with the approaches used in other models.

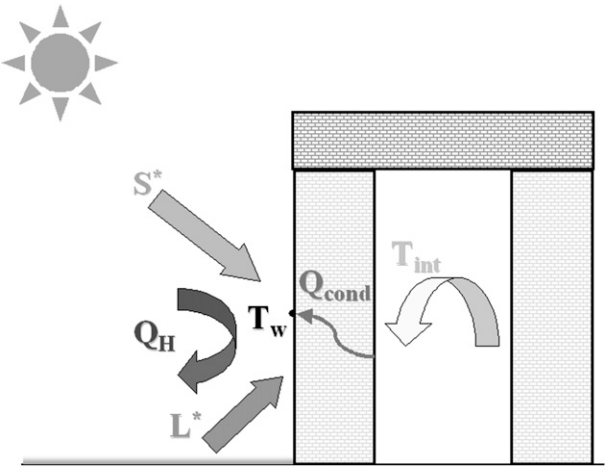

FIG. 1. Schematic representation of the energy exchanges at an urban surface (cross section of a building) (S^*: net shortwave radiative flux; L^*: net longwave radiative flux; Q_H: sensible heat flux; Q_{cond}: conduction heat flux; T_W: wall surface temperature; T_{int}: internal building temperature).

2. Equations and model design

As a key parameter, surface temperature T_{sfc} is determined by the SEB, which governs the energy exchange processes between each urban surface and the atmosphere (Fig. 1). It is given by

$$Q_{\text{cond}} + Q_H = L^* + S^*, \tag{1}$$

where Q_{cond} is the conductive heat flux (W m^{-2}) within the building or the ground subsurface that links the surface temperature to the internal-building or the deep-soil temperature, Q_H is the sensible heat flux (W m^{-2}) and depends on the local wind intensity, S^* is the net shortwave radiative flux (W m^{-2}), and L^* is the net longwave radiative flux (W m^{-2}). We neglect in this study the other energy fluxes such as the anthropogenic flux and the latent heat flux. In our model the advection fluxes are taken into account by the full resolution of the flow field.

a. CFD model

To solve the dynamics and therefore to resolve the Q_H term explicitly, simulations are performed with the 3D open-source CFD code known as Code_Saturne (Archambeau et al. 2003), which can handle complex geometry and complex physics. The flow features in built-up areas make the modeling within the urban canopy difficult. Some typical effects that we have to handle are 3D vortices behind the buildings, high wind speed near the edges of the upwind face, wake effects, and modified turbulence.

In this work, we use the atmospheric module of Code_Saturne, described in detail in Milliez and Carissimo (2007), which takes into account the larger-scale meteorological conditions and the thermal stratification of the atmosphere. In our simulations, we use a Reynolds-averaged Navier–Stokes (RANS) approach with a k–ε turbulence closure. The numerical solver is based on a finite-volume approach for collocated variables on an unstructured grid. Time discretization is achieved through a fractional step scheme, with a prediction–correction step.

b. Radiative model

A new atmospheric 3D radiative scheme was developed in Code_Saturne for the urban canopy (Milliez 2006). We have adapted to the atmosphere a radiative heat transfer scheme available for complex geometry in Code_Saturne that solves the radiative transfer equation for a gray nondiffusive semitransparent media:

$$\mathrm{div}[I(\underline{x}, \underline{D})\underline{D}] = -K(\underline{x})L(\underline{x}, \underline{D}) + K(\underline{x})\sigma T_a^4(\underline{x})/\pi, \quad (2)$$

where $I(\underline{x}, \underline{D})$ is the intensity of radiation at the point $\underline{x}$ and for the propagation direction $\underline{D}$, $K(\underline{x})$ is the absorption coefficient, $L(x, \underline{D})$ is the luminance (W m^{-3} sr^{-1}), and T_a is the air temperature (K). In a semitransparent media, I (W m^{-3} sr^{-1}) and K can be considered to be independent of the wavelength and are integrated over the spectrum. The rate of radiation heating S_{rad} (W m^{-3}) is then given by

$$S_{\mathrm{rad}} = -\mathrm{div}\int_0^{4\pi} I(\underline{x}, \underline{D})\underline{D}\, d\Omega, \quad (3)$$

where $d\Omega$ is the element of the solid angle (sr) around the direction.

1) Discrete ordinate method (DOM)

To solve the radiative transfer equation, we chose the discrete ordinate method (Fiveland 1984; Truelove 1987; Liu et al. 2000), which is based on the directional propagation of the radiative wave. The spatial discretization uses the same mesh as the CFD model. The angular discretization has two resolutions: 32 or 128 directions.

2) Shortwave and longwave radiation

As is usually done, we separate the atmospheric radiation into shortwave and longwave radiation. The total incoming and outgoing shortwave radiative fluxes for each solid surface are given by

$$S^{\downarrow} = S_D + S_f + S_e \quad \text{and} \quad (4)$$

$$S^{\uparrow} = \alpha S^{\downarrow}, \quad (5)$$

where $S^{\downarrow}$ and $S^{\uparrow}$ are respectively the incoming and outgoing shortwave radiative fluxes (W m^{-2}), S_D is the direct solar flux (W m^{-2}), S_f is the solar flux diffused by the atmosphere above our simulation domain (W m^{-2}), S_e is the flux diffused by the environment, that is, resulting from the multireflections on the other subfacets (W m^{-2}), and α is the albedo of the surface.

We express the longwave radiation flux for each surface as

$$L^{\downarrow} = L_a + L_e \quad \text{and} \quad (6)$$

$$L^{\uparrow} = \varepsilon\sigma T_{\mathrm{sfc}}^4 + (1 - \varepsilon)(L_a + L_e), \quad (7)$$

where $L^{\downarrow}$ and $L^{\uparrow}$ are respectively incoming and outgoing longwave radiation flux (W m^{-2}), ε is emissivity of the surface; σ is the Stefan–Boltzmann constant ($5.667\ 03 \times 10^{-8}$ W m^{-2} K^{-4}), T_{sfc} is the surface temperature (K), and L_a and L_e are the longwave radiation flux from the atmosphere and from the multireflection on the other surface. As the first step of validation, we assume that, at the scale of our simulations, the atmosphere between the buildings is transparent and set the absorption coefficient to 0 for both the longwave and shortwave radiation.

3) Surface temperature model

The force–restore approach (Deardorf 1978) is commonly used to calculate the ground temperature in meteorological models. This approach is considered to be a very useful tool because a prognostic equation for temperature is used to reproduce the response to periodic heating of the soil. This model has been extended to urban surfaces (Johnson et al. 1991; Dupont and Mestayer 2006). This extension nevertheless supposes well-insulated buildings with a nearly constant internal temperature and homogeneous material. In our model, the force–restore method has been available for some time in simple geometries and has been extended to complex geometries. Because of the limiting hypotheses built into the method, however, especially concerning the deep-soil temperature, we have also tested a simple wall thermal model with a given thickness and an average thermal conductivity.

(i) Force–restore model

The force–restore model is based on a two-layer decomposition of a material considered to be homogeneous: the surface-layer temperature T_{sfc} responding to external forcing and the deeper layer independent of the diurnal variation. It reads

$$\frac{\partial T_{\text{sfc}}}{\partial t} = \frac{\sqrt{2\omega}}{\mu}(L^* + S^* - Q_H) - \omega(T_{\text{sfc}} - T_{g/b}), \quad (8)$$

where ω is the Earth angular frequency (Hz), μ is the thermal admittance (J m^{-2} s$^{-0.5}$ K^{-1}), and $T_{g/b}$ is either deep-soil or internal building temperature (K).

(ii) Wall thermal model

This model solves the conduction equation to compute the wall temperature. It reads, after expressing each term in Eq. (1), as

$$\frac{\lambda}{e}(T_{\text{sfc}} - T_{\text{int}}) + h_f(T_{\text{sfc}} - T_a) = \varepsilon(L_a + L_e - \sigma T_{\text{sfc}}^4) + (1 - \alpha)(S_D + S_f + S_e), \quad (9)$$

where λ is the average thermal conductivity of the wall (W K^{-1} m^{-1}), e is the thickness of the wall (m), T_{int} is the internal air temperature (K), h_f is the heat transfer coefficient (W m^{-2} K^{-1}) computed from local flow parameters, and T_a is the external air temperature (K).

4) INTERNAL BUILDING TEMPERATURE

In a real building with good insulation, the variation of the internal building temperature is small. In the experiment we simulate (see section 3), however, the buildings are represented by poorly insulated shipping containers. In this case, the variation of the internal temperature is important and has a great influence on the surface temperature. The internal temperature was not measured in the experiment, however and we computed it with one of the following methods.

(i) Constant T

In this case, the internal building temperature is set to a constant and is computed by averaging the diurnal temperatures of all of the building surfaces.

(ii) Evolution equation

A temperature evolution equation, as in Masson et al. (2002), is used to represent the temperature inside the buildings:

$$T_{\text{int}}^{n+1} = T_{\text{int}}^{n-1}\left(\frac{\tau - \Delta t}{\tau}\right) + \overline{T}\left(\frac{\Delta t}{\tau}\right), \quad (10)$$

where T_{int}^{n+1} and T_{int}^{n-1} are the computed internal temperatures (K) at the following and previous time step, respectively, Δt is the time step (s), τ is the period (equal to 1 day; (s), and $\overline{T}$ is the average over all of the surface temperatures (K) computed at time step n.

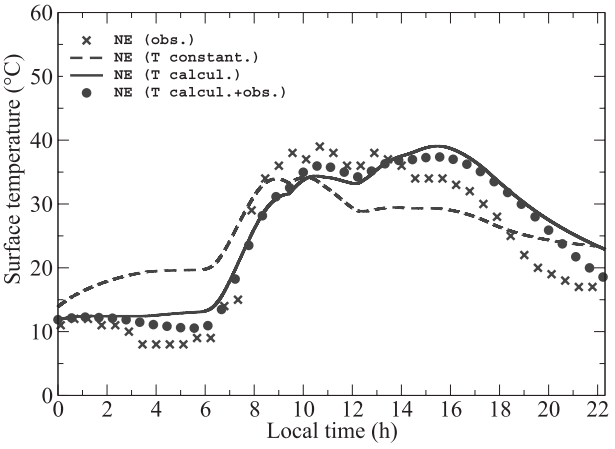

FIG. 2. Comparison of the diurnal evolution of the surface temperature of a northeast-oriented wall computed with three different models for the internal temperature (times signs: surface temperature from the measurements; dashed line: taking a constant internal building temperature; solid line: taking an evolution equation; filled circles: taking the average surface temperature from the measurements and then using the result in the evolution equation).

(iii) Evolution equation with $\overline{T}$ interpolated from measurements

We use the previous formula [Eq. (10)] and replace $\overline{T}$ from the calculation with the average of the measured surface temperatures.

Figure 2 compares the northeast wall surface temperature of a shipping container computed with the three different internal temperature models and the measurements from the Mock Urban Setting Test experiment (see section 3). The value of the constant average internal temperature model is 24°C, which is approximately 2 times the initial values in the other two internal temperature models. Before sunrise, this high value of the constant internal temperature induces a too-rapid heating of the northeast wall. At midday, the constant internal temperature is too low to account for the warming of the surface by the interior air heated by the other sunlit surfaces of the container. Computing the internal temperature with an evolution equation model decreases the heating of the northeast wall before sunrise and improves the results at midday. The differences in the results obtained by using the two evolution equation models (with $\overline{T}$ from computation and $\overline{T}$ from measurements) are small, which was expected because $\Delta t/\tau$ is small. Nevertheless, using the observed average temperature slightly improves the results, especially during the night, when the atmospheric radiative fluxes decrease. The same conclusion applies for the other sides of the containers, which are not shown here. We stress that this may be relevant only in the case of metal containers.

5) CONVECTION MODEL

The thermal energy equation of the flow must be solved, both to determine stratification effects on vertical turbulent transport and to estimate the surface–air thermal gradient that controls convective heat transfer. The sensible heat flux Q_H is given by

$$Q_H = h_f(T_a - T_{\text{sfc}}). \tag{11}$$

Detailed comparisons between different approaches to model the heat transfer coefficient will be discussed in section 5. Our CFD model solves in 3D the RANS equations in the entire fluid domain. In our simulations, we use a rough-wall boundary condition. The h_f is computed for each solid subfacet, depending on the local friction velocity:

$$h_f = \frac{\rho C_p u_* \kappa f_m}{\sigma_t \ln\left(\dfrac{d + z_0}{z_{0_T}}\right)\sqrt{f_h}}, \tag{12}$$

where ρ is flow density (kg m^{-3}), C_p is specific heat (J kg^{-1} K^{-1}), u_* is the friction velocity, κ is the von Kármán constant, σ_t is the turbulent Prandtl number, d is the distance (m) to the wall, z_0 is the roughness length (m), z_{0_T} is the thermal roughness length (m), and f_m and f_h are the Louis (1979) stability functions.

3. Study case: The Mock Urban Setting Test

a. Configuration of the experiment

The Mock Urban Setting Test (MUST; Biltoft 2001; Yee and Biltoft 2004) conducted in the Utah desert is a near-full-scale experiment that consists of measurements in an idealized urban area represented by 120 shipping containers (length L × width W × height H = 12.2 m × 2.42 m × 2.54 m) arranged in a regular array. MUST has already been used to validate dynamics and dispersion models (Brook et al. 2002; Hanna et al. 2002; Camelli et al. 2005; Milliez and Carissimo 2007, 2008). Because temperature data are also provided, we used the MUST field experiment to study in detail the dynamic–radiative coupling. We focused our study on one instrumented container within the array, and therefore the computational domain was reduced to three rows of three containers (Fig. 3).

From the MUST experiment, we selected the day of 25 September 2001. Despite a fairly strong wind (U_{mean} = 7 m s^{-1}), we selected this day because it has already been partly simulated for studies on dispersion (Milliez and Carissimo 2007) and moreover because a complete 24-h dataset for the upstream wind and the surface temperature was available (which was not the case for other days). During this day (Fig. 4), the wind velocity varied from U_{min} = 3 m s^{-1} to U_{max} = 11.5 m s^{-1} and the average diurnal air temperature was about 24°C (measured at 10 m). For our coupling study, the wind speed may be a little high to test strong radiative effects on the airflow, but it emphasizes the convective effects on the surface temperature.

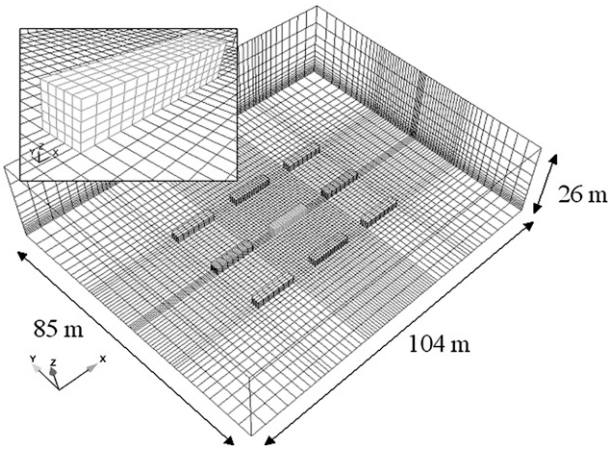

FIG. 3. Mesh of the domain and the subdomain for the 0.8 m × 0.5 m × 0.5 m resolution.

b. Boundary conditions and surface parameters

Table 1 gives the parameters used in the simulation. To be consistent with the experiment, the wind inlet boundary conditions are determined from measurements, using a meteorological file that contains the wind velocity, turbulence kinetic energy, dissipation rate, and temperature profiles for every 2 h. The variation of the deep-soil temperature is neglected. The internal building temperature is computed by the evolution equation with $\overline{T}$ from measurements. We take the same value of the roughness length z_0 as in Eichhorn and Balczo (2008). The thermal roughness length z_{0_T} is considered to be 1/10 of z_0 (Garratt 1992). Because some thermal properties were not determined during the experiment, their values were taken from the literature: we took the values of the albedo and emissivity of the wall to be those of corrugated iron (Oke 1987). The thermal admittance was taken assuming an insulating material in the walls, as observed in some pictures. The ground albedo α_s that was input to the model was evaluated from the incoming and outgoing solar fluxes measured upstream by pyranometers and depends on the zenith angle.

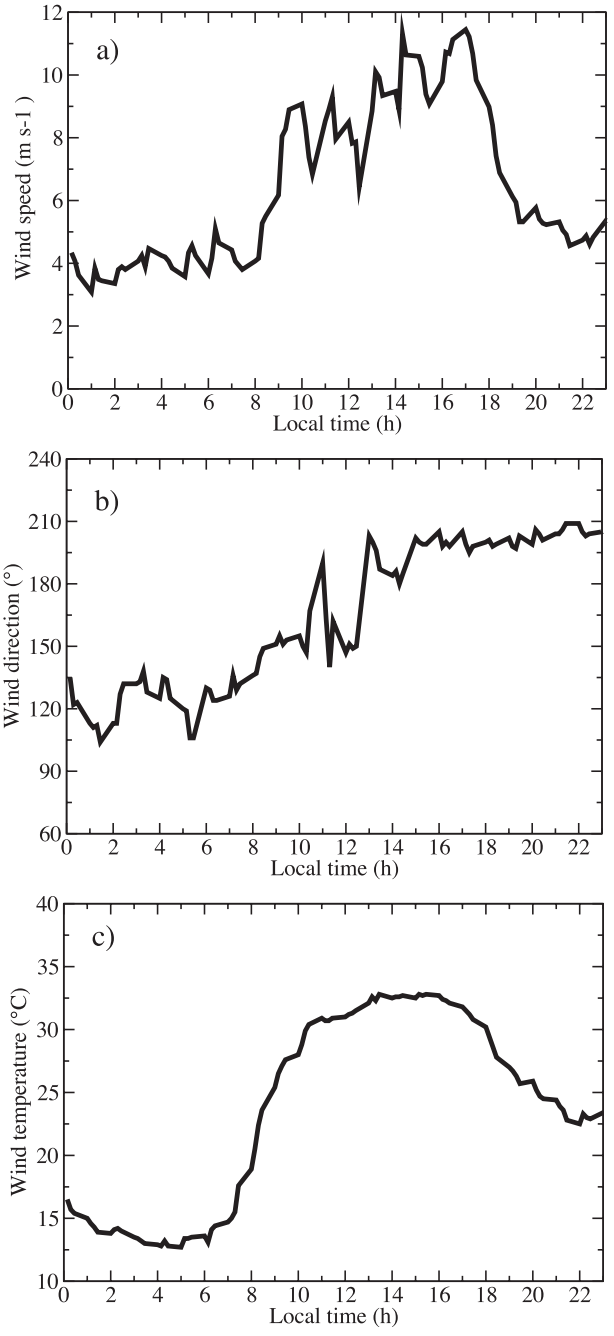

FIG. 4. Meteorological data at 10 m from the MUST experiment for 25 Sep 2001: (a) wind speed (m s^{-1}), (b) meteorological wind direction (°), and (c) wind (air) temperature (°C).

TABLE 1. Parameters employed in the MUST simulations, with Z_{ref} being the reference height for forcing data, U_{ref} being the initial wind speed at Z_{ref}, and θ being the initial wind angle. Soil z_0, wall z_0, and roof z_0 are respectively the roughness length for momentum of soil, walls, and roofs. Soil z_{0_T}, wall z_{0_T}, and roof z_{0_T} are respectively the roughness length for heat of soil, walls, and roofs; α_S, α_W, and α_R are respectively the shortwave albedo of soil, walls, and roofs; ε_S, ε_w, and ε_R are respectively the longwave emissivity of soil, walls, and roofs; μ_S, μ_W, and μ_R are respectively the admittance of soil, walls, and roofs; T_{air} is the initial air temperature at Z_{ref}; T_S and T_{Sint} are respectively the initial soil temperature and deep-soil temperature; T_{Top}, T_{NW}, T_{SE}, T_{NE}, and T_{SW} are initial individual surface temperature; T_{Wint} and T_{Rint} are respectively the building and roof internal temperature.

Parameter	Unit	Value
Dynamic		
Time step	s	0.1
Z_{ref}	m	10
U_{ref}	m s^{-1}	4.27
θ	°	135
Soil z_0	cm	2
Wall z_0 = roof z_0	cm	0.2
Radiative		
Time step	min	5
Soil z_0	cm	0.2
Wall z_{0_T} = roof z_{0_T}	cm	0.02
α_S		From measurements
$\alpha_W = \alpha_R$		0.1
ε_s		0.8
$\varepsilon_w = \varepsilon_R$		0.13
μ_S	J m^{-2} $s^{-0.5}$ K^{-1}	1200
$\mu_W = \mu_R$	J m^{-2} $s^{-0.5}$ K^{-1}	1600
Initial values		
T_{air}	°C	16.45
T_S	°C	15.88
T_{Sint}	°C	24.28
T_{Top}	°C	9.28
T_{NW}	°C	10.50
T_{SE}	°C	11.68
T_{NE}	°C	11.87
T_{SW}	°C	12.37
$T_{Wint} = T_{Rint}$	°C	11.11

c. *Numerical sensitivity*

Before starting our simulations, we performed a numerical sensitivity study for the grid size, the number of directions in the discrete ordinate method, and the radiative time step. We focus here on the radiative aspects because a sensitivity study of the dynamical part has already been performed (Milliez and Carissimo 2007, 2008).

Figure 5 shows surface temperature evolution with grids of different resolutions. The fine (~55 000 cells) and the refined grids (~173 000 cells) give similar results, and the coarse grid (~4000 cells) overestimates or underestimates temperatures, and therefore the fine grid is used in the remaining simulations. Among these three resolutions, we also observe that the coarse grid largely underestimates the southwest surface temperature at about 16 h. The reason is that this surface receives less direct solar flux in the coarse grid than in the fine grid as shown on (Fig. 6). In addition, the thermal boundary layer close to the heated surface may need a sufficient resolution to be captured in such a canopy.

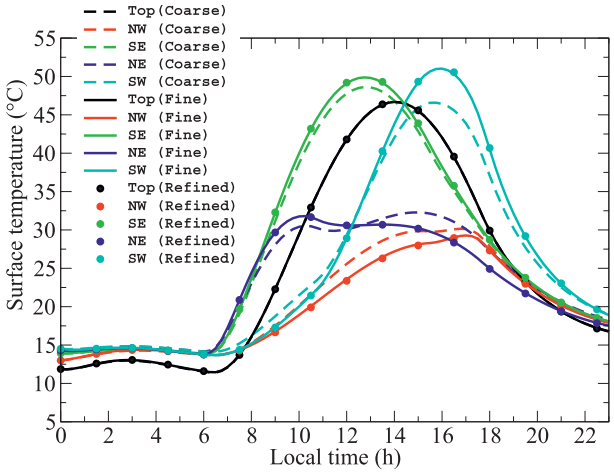

FIG. 5. Surface temperature evolution during a diurnal cycle for different mesh resolutions: dashed lines: coarse grid of ~4000 cells; solid lines: fine grid of ~55 000 cells; filled circles: refined grid about 173 000 cells.

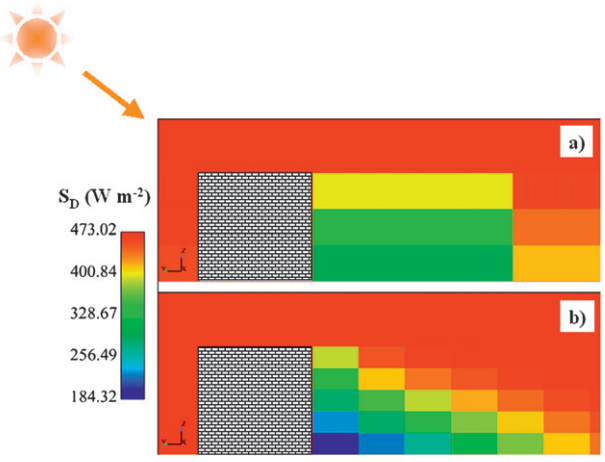

FIG. 6. Vertical cross section of the direct solar flux in the fluid domain around a building at 16 h for different spatial resolutions: (a) coarse grid and (b) fine grid.

Hence, we verified that the fine resolution (0.5 m) in the canopy is enough to reproduce a thermal boundary layer thickness of about 2 m.

In our model, the DOM was implemented with two angular discretizations: 32 or 128 directions, which influence the prediction of the diffuse solar flux and the infrared flux. In this case, the results obtained with 32 directions are very close to the ones with 128 directions, but the calculation is faster by a factor of 5. So we took 32 directions in the remaining simulations. A time step was introduced for the radiative scheme that is different from the one used for the dynamics. We have tested several radiative time steps: 1, 5, 15, and 30 min and 1 h for a diurnal cycle simulation. The resulting difference between a time step of 1 min and 5 min is small, being less than 1°C. We considered that 5 min was an optimum radiative time step for our simulations. The time step for the dynamics was set to 0.1 s after Milliez and Carissimo (2007). The 24-h simulation in parallel computing on a workstation with eight processors took approximately 4.5 days. We have also tested a dynamical time step of 0.5 s, which reduces the computational time to less than 1 day: the results are close to the ones obtained with a dynamical time step of 0.1 s from 0 to 9 h, but after 10 h an important difference (12%–30%) appears when the wind speed exceeds 6 m s^{-1} (Fig. 4). In cases in which the wind speed is small, we could set up the dynamical time step to 0.5 s to reduce significantly the CPU time. The full radiative–dynamic coupling remains computationally expensive, in comparison with simpler models, but at this stage the model is intended for research and not for operational applications.

4. Results

a. *Simulation of 25 September*

Figure 7 shows the evolution of modeled and measured surface temperatures using the force–restore method, with two modeling approaches: 1) radiative only and no convection model (meaning with the convective flux set to zero) and 2) coupled radiative and dynamical model. The diurnal evolutions of the surface temperatures of the top face, southeast face, and northeast face are correctly reproduced by our coupled model. For the northwest face and the southwest face, the simulations show a delay in the morning warming. This delay in warming can be explained by the conduction between the container walls, which contributes to the fast warming in the northwest and southwest faces before they are in the sun but which is neglected in the simulations. In addition, this delay may be inherent to the force–restore method, which overestimates in this case the relaxation to the internal temperature and therefore enhances the thermal inertia. This inertia effect is also observed after sunset for the simulated northwest surface temperature, which shows a delay in cooling. In the afternoon when the atmospheric radiative forcing increases, however, the modeled surface temperatures compare well to the measurements. The comparison with measurements shows a large improvement for the coupled model as compared with the radiative-only model, underlining the importance of accurately including the effect of convection in microscale modeling.

b. *Sensitivity to the surface parameters and surface temperature models*

The values of the surface parameters were taken from the literature. The values for the thermal properties of

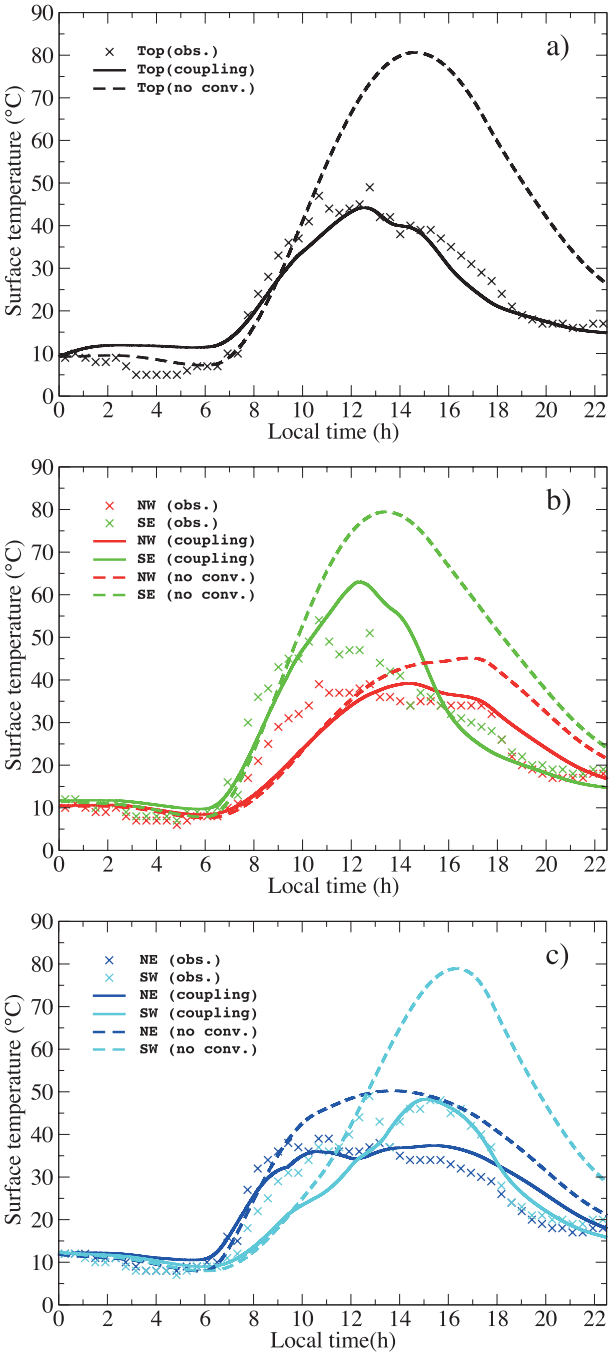

FIG. 7. Evolution of surface temperature of (a) roof (top), (b) northwest, southeast, (c) northeast, and southwest faces modeled using the force–restore method during a diurnal cycle (crosses: measurements; dashed lines: simulation with radiation only; solid lines: simulation with the dynamic–radiative coupling).

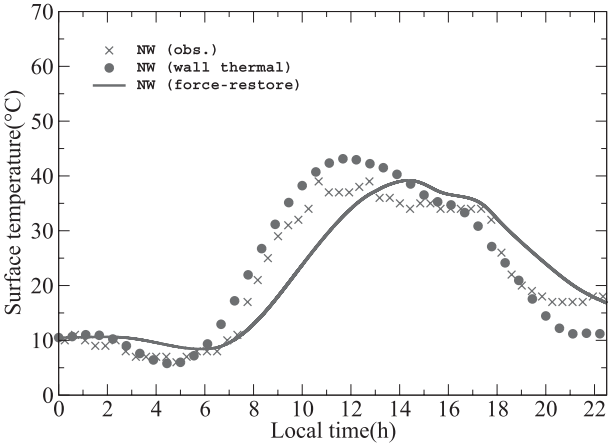

FIG. 8. The northwest wall temperature evolutions obtained with different surface temperature models (crosses: measurements; filled circles: wall thermal model; solid line: force–restore method).

metal cover a wide range (Oke 1987), however, and we performed a sensitivity study of the variation of the surface temperatures when varying the parameters in the range given by the literature. Table 2 illustrates that a change in albedo, emissivity, or admittance, in the range given by the literature, can make a difference of about 1°–10°C for the surface temperature. Because the southeast wall is the most exposed to the sun all day, the deviation of the temperature on this wall is the most important.

The results presented above were obtained by using the force–restore method and are now compared with those obtained with the wall thermal model [see section 2b(3)]. The emissivity was chosen after Oke (1987) for corrugated iron. Because some of the containers in the MUST array were painted, we also made a test taking a much higher emissivity (i.e., 0.9). It results in a decrease in surface temperature. This decrease is greater when using the force–restore method, about 10°C for the southeast wall and 5°C for rest of the walls. For the wall thermal model, the influence of higher emissivity on the surface temperature is less significant, the difference being less than 2°C for all of the faces. This is can be explained the fact that the internal temperature has a greater influence than the other surface parameters. The wall thermal model also requires the characteristics of the surface material and the thickness and the thermal conductivity of the wall which were not provided in the data. When choosing a thermal conductivity of 26 W K^{-1} m^{-1} for the walls, the resulting conduction remains too high, resulting in an homogenization of the temperature of the five walls (not shown here). To improve the comparisons with the observations, we adjusted the value of the conductivity to 6 W K^{-1} m^{-1}, which is not that of pure metal, but may be set by assuming an insulating material in the walls. In Fig. 8, we display the evolution of the northwest wall temperature where we used a conductivity of 6 W K^{-1} m^{-1} and

TABLE 2. Deviation of the surface temperatures (°C) during a diurnal cycle by varying albedo, emissivity, and thermal admittance (J m^{-2} s$^{-0.5}$ K^{-1}), respectively.

Parameter	Variation	Top	Northwest	Southeast	Northeast	Southwest
Albedo	+0.1	−2.6	−1	−4.5	−1.5	−2.3
Emissivity	+0.15	−1.3	−1.2	−3.5	−1	−3.2
Admittance	−400	+1.8	+2	+10.1	+2.6	+2.5

a thickness of 10 cm for the wall and compare it with the observations and that obtained with the force–restore method. In the morning, the wall thermal model (represented by the circles) is able to simulate accurately the increase in the northwest wall surface temperature at 0600 LT, with no delay, as opposed to the force–restore model (represented by the solid line). An overcooling of the surface temperature appears after sunset, however. This overcooling may be explained by a wrong estimation of the internal temperature by the evolution equation, which is highly dependent on the other computed surface temperatures. Another reason could be an overestimation of the mixing by the turbulence scheme, but we expect this deficiency to be weak. Indeed, the turbulence scheme, which takes into account the stability effects, has been extensively used and was previously validated (Buty et al. 1988; Milliez and Carissimo 2008). The wall thermal model seems more adapted to shipping containers than is the force–restore method, however, and a perspective would be to improve the conduction model by, for instance, implementing a multilayer wall model.

5. Discussion: Comparison of three schemes of increasing complexity for predicting surface sensible heat flux

In this section, sensitivity testing is done to compare three schemes used for predicting surface sensible heat flux. The simulated case is based on the MUST geometry with an upstream wind direction of −45°, a reference 10-m wind speed $U_{\text{ref}} = 4$ m s^{-1}, and an initial air temperature of 18°C. The simulation starts at 1200 LT for period of 30 min.

a. Constant h_f model

This scheme is usually used in architecture simulation tools (Miguet and Groleau 2002; Asawa et al. 2008). The radiative model in this type of tool is very accurate, usually using a detailed 3D geometry. The convective model is very simplified, however, and the scheme considers a constant transfer coefficient. For the comparison, we take the constant h_f as the average value on each wall from the 3D convection model that we presented in section 2b(5). Here, we take h_f equal 14.45 W m^{-2} K^{-1} for the roof and 6.12 W m^{-2} K^{-1} for the walls.

In fact, if instead of taking the same constant h_f for all of the walls, we take separate transfer coefficients for each surface (roof 14.45; northwest face 3.94; southeast face 10.78; northeast face 1.38; southwest face 8.35), we can better take into account the orientation of the surface in the wind flow, which decreases the wall surface temperatures by about 2–4 K.

b. One-dimensional h_f model (1D h_f)

In this model employed in TUF-3D (Krayenhoff and Voogt 2007) and similar to the one used in Masson (2000), the transfer coefficient is calculated based on a simple relationship (Martilli et al. 2002):

$$h_f(z) = 11.8 + 4.2u(z) - 4.0, \tag{13}$$

with $u(z)$ being the vertical wind profile within the canopy. Many authors model this wind profile within the canopy with an exponential law (Cionco 1965; Rotach 1995; Krayenhoff and Voogt 2007). For instance, in TUF-3D, Krayenhoff and Voogt (2007) used an iterative way to find a profile of the exponential form with three coefficients. Here, we model the vertical velocity with the exponential profile of Macdonald (2000), which is well adapted to low-density arrays:

$$u(z) = u_H \exp[a(z/H - 1)], \tag{14}$$

where u_H is the mean velocity at the top of the obstacles and the constant a is the attenuation coefficient, which is determined by fitting the average wind profile within the obstacle array.

c. Three-dimensional h_f model (3D h_f)

The full model is three dimensional not only in terms of the radiative exchanges but also the convective exchanges. In this approach, h_f is computed by resolving the 3D RANS and energy equations in the whole fluid domain. Coefficient h_f is calculated for each subfacet depending on the local friction velocity [Eq. (12)], and the sensible heat flux is calculated with the local air temperature [Eq. (11)].

d. Discussion

Figure 9 illustrates the effect of the three convective schemes by visualizing, successively, the transfer

coefficient, the sensible heat flux, and the surface temperature. The three convective schemes show a difference of the sensible flux of approximately 100–240 W m^{-2} for the southeast face and northeast face. With the constant h_f model, the surface temperatures are more homogeneous than in the other two cases. In the MUST configuration, the building array is not dense, and therefore the effects of the shadow and the multireflections are small. That is the reason why the temperatures in the constant h_f approach show little difference within each wall. With the 1D h_f model, we can obviously see the 1D inhomogeneity of the surface temperatures, which is linked to the exponential law wind profile. The 3D h_f model results show the 3D inhomogeneity of the surface temperatures, linked to the inhomogeneity of the 3D wind. On the same face with the same material, we can have a difference of temperature of about 4 K. These results demonstrate the effects of realistically computing the convection fluxes on the surface temperature in the urban areas. Note that in the comparison of the three convective schemes we change only the transfer coefficient and not the air temperature (which is computed for each grid cell of the fluid domain in three dimensions). A simple air temperature model could lead to additional differences.

6. Conclusions and perspectives

New atmospheric radiative and thermal schemes were implemented in the atmospheric module of the three-dimensional CFD code known as Code_Saturne. The purpose of this paper was to study in detail the coupling between the radiative scheme and the 3D dynamical model. The model was evaluated with the field measurements from an idealized urban area, the MUST experiment. The coupled model is able to reproduce the evolution of the surface temperatures for different sides of a container within the MUST canopy during a diurnal cycle despite a delay in warming for the northwest and southwest faces at sunrise. The simulations also showed a significant impact of the convective flux on the surface temperatures.

Because the thermal information available in the MUST field is insufficient, sensitivity studies were performed that emphasized the dependence of the model on the parameters describing the building: the properties of the material. In addition, the internal building temperature shows great importance because the buildings are made of metal.

We compared two ways of computing the surface temperature: the force–restore method and a wall thermal model. Because the force–restore method may be more suited for insulated buildings with a near-constant internal temperature (which is not very representative of the MUST containers), we have also tested a one-layer wall model. Using an appropriate evolution equation for the interior buildings, the force–restore shows

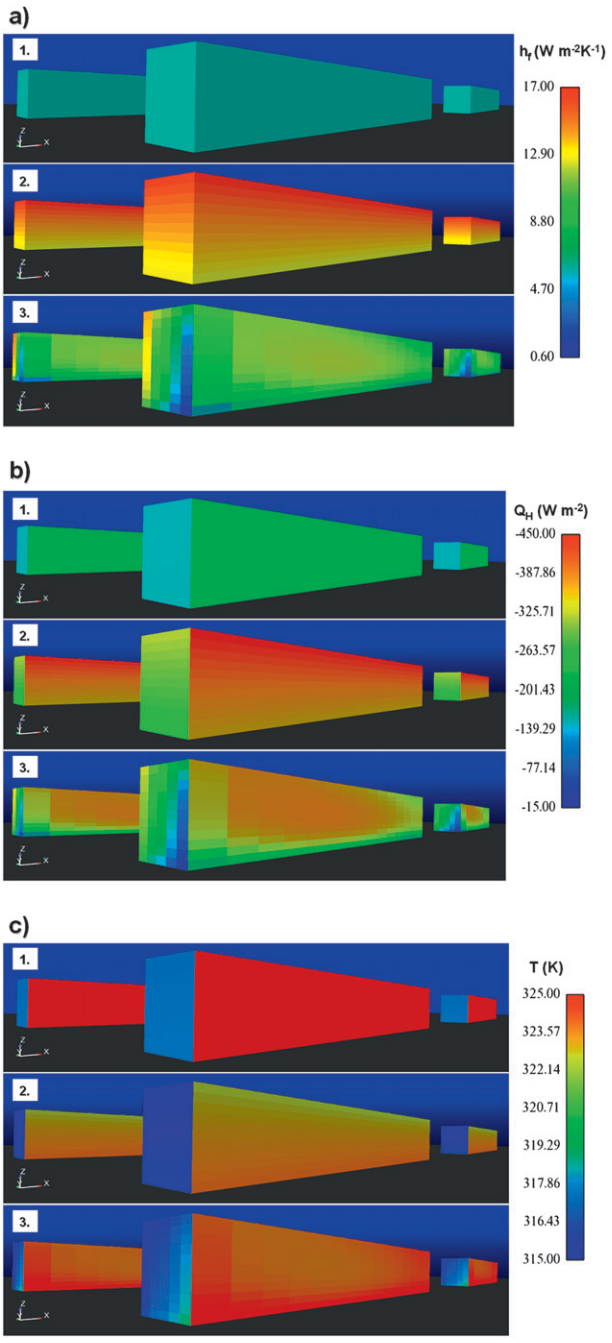

FIG. 9. Comparison of three convective models with visualization of the southeast and northeast walls at 1230 LT: (a) transfer coefficient h_f (W m^{-2} K^{-1}), (b) sensible heat flux Q_H (W m^2), (c) surface temperature T (K). Label 1 indicates the constant h_f model, label 2 is for the 1D h_f model, and label 3 represents the 3D h_f model.

good results during the afternoon. It induces a delay in warming at sunset, however, and for the northwest wall a delay in cooling, because of the thermal inertia inherent to the method. The one-layer wall thermal model we tested also show some weakness, since it can reproduce the diurnal cycle of the different surface temperature only with a very low thermal conductivity. Nevertheless, it seems more adapted to model shipping containers than is the force–restore method. One proposed improvement is to implement a multilayer 1D thermal model for the walls, as in Masson (2000) or Krayenhoff and Voogt (2007), which may be more adequate for such surfaces. In fact, shipping-container surface temperatures appear difficult to predict with classical urban models, which for instance do not take into account the conduction between the walls, which can be neglected for real buildings but should not be for metal containers, and a 3D conduction wall model may in this case be necessary.

We also compared our 3D modeling approach to estimate the convective exchanges at the surface (which consists of solving the 3D RANS equations in the whole fluid domain) with two modeling approaches found in the literature: the first approach consists in using a constant heat transfer coefficient, and the second approach is to use a 1D equation based on a vertical wind profile within the canopy. The comparisons are made in terms of the convective transfer coefficients, sensible heat fluxes, and surface temperatures. The three schemes give values of the same order of magnitude for the average surface temperature; nevertheless, only the 3D approach can reproduce the inhomogeneous effect on the wind on a surface: the difference of the same wall can reach 4 K.

The simulation of realistic atmospheric conditions in the urban areas made possible by this work can be used for various applications. A first example is to study pollutant dispersal in a low-wind case. A good description of the heat transfer is essential to describe the convective movement of the air in the streets and is very important for air pollution investigations. A second example is the energy balance of buildings. Estimating the convection fluxes in simple models can keep the computing time low and has application in mesoscale studies; nevertheless, at microscale, it can lead to misleading values in the estimation of the energy loss from the buildings to the atmosphere. In this case, a good prediction of the convective flux can be helpful to the management of the energy consumption and a useful tool in building design. The simulations' results show a significant difference of the parameterizations between taking a simple convection model and describing the physical processes in a realistic way, coupling the 3D dynamics and the radiative processes. The simulations point out the larger difference in surface temperatures at different locations on the same wall.

This study is the first step to validate our dynamic–radiative coupling model. This 3D modeling investigation can bring more detailed information both on radiative and convective fluxes in very local-scale studies. In the MUST case, however, the urban area is idealized. At microscales, small irregularities can break the repeated flow patterns found in a regular array of containers with identical shape. In addition, uncertainties associated with the thickness and the properties of the material of the container wall limit our ability to validate the results. There are also still challenges for modeling in this area. The comparison of three different modeling approaches to estimate the convective exchanges at the surface could be compared with observations if thermal images are available. That is the reason why we will evaluate the coupled dynamic–radiative model on a district of a real urban area with the Canopy and Aerosol Particles Interactions in Toulouse Urban Layer (CAPITOUL) experiment (in the city of Toulouse, France) (Masson et al. 2008; Lagouarde et al. 2010) for which thermal infrared images are available.

Another perspective of this work is to apply the 3D radiative scheme to nontransparent media. Indeed, in many urban applications, the atmosphere between the boundaries can be considered to be transparent and nondiffusive. Nevertheless, when studying smoke dispersion or fog formation and dissipation, absorption and diffusion play an important role. Absorption can already be taken into account by our scheme, and one important perspective of this work is to study radiation in 3D nontransparent media and add the diffusion term in the resolution of the radiative transfer equation.

Acknowledgments. The authors thank the Defense Threat Reduction Agency (DTRA) for providing access to the MUST data.

REFERENCES

Archambeau, F., N. Méchitoua, and M. Sakiz, 2003: Code_Saturne: A finite volume code for the computation of turbulent incompressible flows—Industrial applications. *Int. J. Finite Vol.,* **1,** 1–62.

Arnfield, A. J., 2003: Two decades of urban climate research: A review of turbulence, exchanges of energy and water, and the urban heat island. *Int. J. Climatol.,* **23,** 1–26.

Asawa, T., A. Hoyano, and K. Nakaohkubo, 2008: Thermal design tool for outdoor space based on a numerical simulation system using 3D-CAD. *Build. Environ.,* **43,** 2112–2123.

Biltoft, C. A., 2001: Customer report for Mock Urban Setting Test. West Desert Test Center, U.S. Army Dugway Proving Ground, DPG Doc. WDTC-FR-01-121, 58 pp.

Brook, D. R., N. V. Beck, C. M. Clem, D. C. Strickland, I. H. Griffits, D. J. Hall, R. D. Kingdon, and J. M. Hargrave, 2002: Validation of the Urban Dispersion Model (UDM). *Proc. Eighth Int. Conf. on Harmonisation within Atmospheric Dispersion Modelling for Regulatory Purposes,* Sofia, Bulgaria, National Institute of Meteorology and Hydrology of Bulgaria, 8–12.

Buty, D., J. Y. Caneill, and B. Carissimo, 1988: Simulation numerique de la couche limite atmospherique en terrain complexe au moyen d'un modele mesometeorologique non hydrostatique: Le code mercure (Numerical simulation of the atmospheric boundary layer in complex terrain by means of a nonhydrostatic model: The Mercury code). *J. Theor. Appl. Mech.,* **7,** 35–62.

Camelli, F. E., R. Lohner, and S. R. Hanna, 2005: VLES study of MUST experiment. *Proc. 43rd AIAA Aerospace Sciences Meeting and Exhibit,* Reno, Nevada, American Institute of Aeronautics and Astronautics, 1–19.

Cionco, R. M., 1965: A mathematical model for air flow in a vegetative canopy. *J. Appl. Meteor.,* **4,** 517–522.

Deardorf, J. W., 1978: Efficient prediction of ground surface temperature and moisture with inclusion of a layer of vegetation. *J. Geophys. Res.,* **83,** 1889–1903.

Dupont, S., and P. Mestayer, 2006: Parameterization of the urban energy budget with the submesoscale soil model. *J. Appl. Meteor. Climatol.,* **45,** 1744–1765.

Eichhorn, J., and M. Balczo, 2008: Flow and dispersal simulations of the Mock Urban Setting Test. *Proc. 12th Int. Conf. on Harmonisation within Atmospheric Dispersion Modelling for Regulatory Purposes,* Cavtat, Croatia, Meteorological and Hydrological Service of Croatia, 67–72.

Fiveland, W. A., 1984: Discrete-ordinates solutions of the radiative transport equation for rectangular enclosure. *J. Heat Transfer,* **106,** 699–706.

Garratt, J. R., 1992: *The Atmospheric Boundary Layer*. Cambridge University Press, 316 pp.

Gastellu-Etchegorry, J., 2008: 3D modeling of satellite spectral images, radiation budget and energy budget of urban landscapes. *Meteor. Atmos. Phys.,* **102,** 187–207.

——, E. Martin, and F. Gascon, 2004: DART: A 3-D model for simulating satellite images and surface radiation budget. *Int. J. Remote Sens.,* **25,** 75–96.

Grimmond, C. S. B., and T. R. Oke, 1999: Heat storage in urban areas: Local-scale observations and evaluation of a simple model. *J. Appl. Meteor.,* **38,** 922–940.

Hanna, S. R., S. Tehranian, B. Carissimo, R. W. Macdonald, and R. Lohner, 2002: Comparisons of model simulations with observations of mean flow and turbulence within simple obstacle arrays. *Atmos. Environ.,* **36,** 5067–5079.

Johnson, G. T., T. R. Oke, T. J. Lyons, D. G. Steyn, I. D. Watson, and J. A. Voogt, 1991: Simulation of surface urban heat islands under 'ideal' conditions at night. Part I: Theory and tests against field data. *Bound.-Layer Meteor.,* **56,** 275–294.

Kanda, M., T. Kawai, M. Kanega, R. Moriwaki, K. Narita, and A. Hagishima, 2005: A simple energy balance model for regular building arrays. *Bound.-Layer Meteor.,* **116,** 423–443.

Krayenhoff, E. S., and J. A. Voogt, 2007: A microscale three-dimensional urban energy balance model for studying surface temperatures. *Bound.-Layer Meteor.,* **123,** 433–461.

Lagouarde, J. P., A. Hénon, B. Kurz, P. Moreau, M. Irvine, J. Voogt, and P. Mestayer, 2010: Modelling daytime thermal infrared directional anisotropy over Toulouse city centre. *Remote Sens. Environ.,* **114,** 87–105.

Lemonsu, A., C. S. B. Grimmond, and V. Masson, 2004: Modelling the surface energy balance of an old Mediterranean city core. *J. Appl. Meteor.,* **43,** 312–327.

Liu, J., H. M. Shang, and Y. S. Chen, 2000: Development of an unstructured radiation model applicable for two-dimensional planar, axisymmetric, and three-dimensional geometries. *J. Heat Transfer,* **66,** 17–33.

Louis, J., 1979: A parametric model of vertical eddy fluxes in the atmosphere. *Bound.-Layer Meteor.,* **17,** 187–202.

Macdonald, R. W., 2000: Modelling the mean velocity profile in the urban canopy layer. *Bound.-Layer Meteor.,* **197,** 25–45.

Martilli, A., A. Clappier, and M. W. Rotach, 2002: An urban surface exchange parameterisation for mesoscale models. *Bound.-Layer Meteor.,* **104,** 261–304.

Masson, V., 2000: A physically based scheme for the urban energy budget in atmospheric models. *Bound.-Layer Meteor.,* **94,** 357–397.

——, C. S. B. Grimmond, and T. R. Oke, 2002: Evaluation of the Town Energy Balance (TEB) scheme with direct measurements from dry districts in two cities. *J. Appl. Meteor.,* **41,** 1011–1026.

——, and Coauthors, 2008: The Canopy and Aerosol Particles Interactions in Toulouse Urban Layer (CAPITOUL) experiment. *Meteor. Atmos. Phys.,* **102,** 135–157.

Miguet, F., and D. Groleau, 2002: A daylight simulation tool for urban and architectural spaces—Application to transmitted direct and diffuse light through glazing. *Build. Environ.,* **37,** 833–843.

Milliez, M., 2006: Modélisation micro-météorologique en milieu urbain: Dispersion des polluants et prise en compte des effets radiatifs (Micrometeorological modeling in urban environment. Dispersion of pollutants and the taking into account of radiative effects). Ph.D. thesis, École des Ponts ParisTech, 228 pp. [Available online at http://cerea.enpc.fr/fich/these_milliez.pdf.]

——, and B. Carissimo, 2007: Numerical simulations of pollutant dispersion in an idealized urban area, for different meteorological conditions. *Bound.-Layer Meteor.,* **122,** 321–342.

——, and ——, 2008: CFD modelling of concentration fluctuations in an idealized urban area, for different meteorological conditions. *Bound.-Layer Meteor.,* **127,** 241–259.

——, L. Musson-Genon, and B. Carissimo, 2006: Validation of a radiative scheme for CFD modelling of heat transfers between buildings and flow in urban canopies. Preprints, *Sixth Int. Conf. on Urban Climate,* Göteborg, Sweden, International Association of Urban Climate, 266–269.

Mills, G., 1996: An urban canopy-layer climate model. *Theor. Appl. Climatol.,* **1997,** 229–244.

Oke, T. R., 1987: *Boundary Layer Climates*. 2nd ed. Routledge, 435 pp.

Rotach, M. W., 1995: Profiles of turbulence statistics in and above an urban street canyon. *Atmos. Environ.,* **29,** 1473–1486.

Truelove, J. S., 1987: Discrete-ordinates solutions of the radiative transport equation. *J. Heat Transfer,* **109,** 1048–1051.

Yee, E., and C. A. Biltoft, 2004: Concentration fluctuations measurements in a plume dispersing through a regular array of obstacles. *Bound.-Layer Meteor.,* **111,** 363–415.

CHAPTER 4

A comparison of two radiation models: *Code_Saturne* and SOLENE

Contents

4.1 Introduction

In order to more accurately model the physics of an urban canopy, new concepts in surface modeling have been developed. We have mentioned several canopy models (see Chapter 2 and 3) which aim to solve the Surface Energy Balance (SEB) for different applications, such as TEB (Masson, 2000), UCLCM (Mills, 1997), SOLENE (Miguet and Groleau, 2002), 3D-CAD (Asawa et al., 2008), DART-EB (Gastellu-Etchegorry, 2008), TUF-3D (Krayenhoff and Voogt,

2007) and SUMM (Kanda et al., 2005). In order to model the radiation exchanges, many SEB models (e.g. Miguet and Groleau (2002); Asawa et al. (2008); Krayenhoff and Voogt (2007)) employ the radiosity method. That is, all radiative reflection and emission is assumed in a transparent medium. The effects of surface morphology on the radiative exchange between a closed system of surfaces surrounding a non-absorbing medium are expressed in terms of the view factors or shape factors for the system of surfaces. Surface morphology affects the radiation balance by altering the magnitude and source of the radiative flux densities incident on each surface. The view factors or shape factors are required when applying the radiosity method to an urban street canyon which are between two equally sized, in-line, parallel planes and between two perpendicular planes sharing a common edge (A_1 and A_2), as shown in Figure 4.1.

Shape factors for the radiative exchange between any two of the canyon surfaces can be derived from one of these two generic types. In general, the radiation is reflected multiple times until the remaining unabsorbed radiation is below a user-defined threshold. Short- and long-wave reflection and absorption are modeled with the same method, but are initialized differently to properly account for shading of direct solar, diffuse solar, and for long-wave emitted from both the sky and the urban surfaces. Each patch requires an albedo and an emissivity as input, while outputs for both wavelength ranges include total reflected radiation, total reflected radiation escaping to the sky, and total absorbed radiation by surfaces.

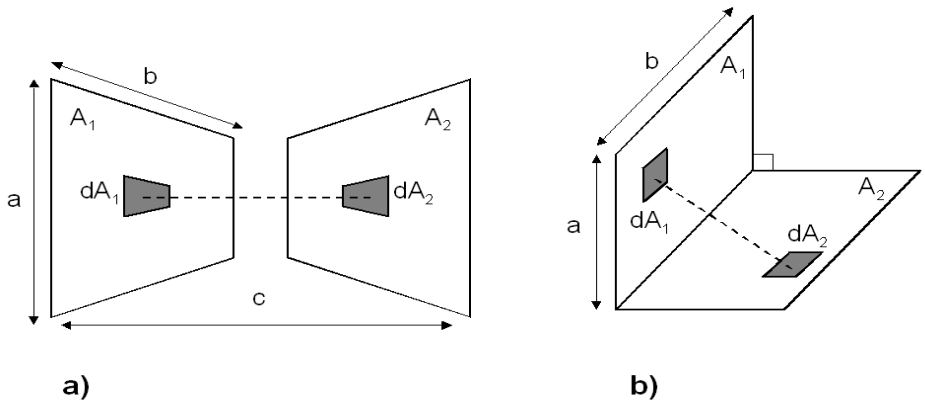

Figure 4.1: Schematics of the view factors or shape factors for the idealized urban street canyons. (a) two parallel in-line planes; (b) two perpendicular planes.

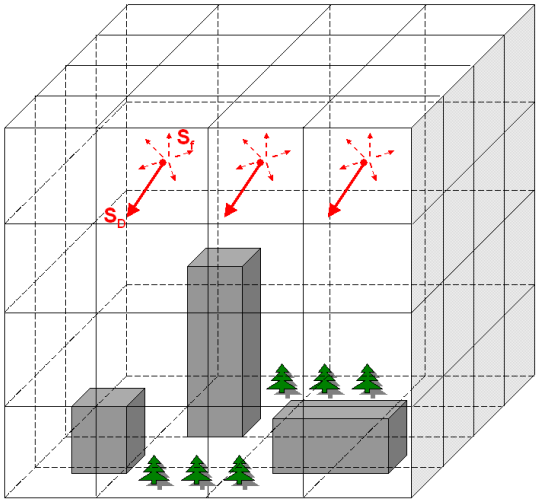

Figure 4.2: Schematics of the radiative model for *Code_Saturne* with: S_D direct solar flux, S_f diffuse solar flux

Since our aim is to model radiative exchange in the ABL ($0 \sim 200\ m$), for instance, eventually with the smoke or fog between the buildings, we chose the Discrete Ordinate Method to solve the radiative transfer equation in the whole fluid domain for *Code_Saturne*. This approach is less precise than the radiosity method to estimate the incoming radiative fluxes on urban surfaces, but we can calculate the radiation flux not only on the facets of the urban landscape but also in each fluid grid cell between the buildings in non-transparent medium (Fig. 4.2). Moreover, as we mentioned in Chapter 2, the mesh is the same in the radiative model and in the CFD model, which makes the dynamic-radiative coupling computation more simple and convenient.

Therefore, it is interesting to discuss different approaches of the radiative heat transfer models. Here we compare the radiative models in *Code_Saturne* and SOLENE with MUST experimental data set.

4.2 Description of SOLENE model

Initially designed for simulating sunshine, natural lighting and thermal radiation over buildings or urban blocks for architectural projects, SOLENE software is developed by CERMA laboratory (http://solene.cerma.archi.fr/) and has been applied in many works (e.g. Ringenbach (2004); Robitu (2005); Hénon (2008); Kurz (2009); Bouyer (2009); Hénon et al. (2011a,b,c) etc.).

4.2.1 Geometry and mesh

With no particular restriction about the geometry and size, taking into account the urban morphology, SOLENE allows simulating different quantities and phenomena, such as the sunshine features (lighting and mask), the various components of solar radiation (direct and diffuse flux incident on each element with multiple reflections between surface features) and thermal infrared radiation. With the 'contour integration' method (e.g. Soux et al. (2004)) the view factors method implemented in SOLENE may be rapidly and precisely calculated between four-sided surfaces of any orientation.

In SOLENE, a geometry is defined by a set of unconnected plane faces, with oriented normal (in general, outward). Each face is constituted itself one or more plane facets. These facets have known contours, which are polygons defined by the coordinates of each vertex relative to the origin, and by the components of the vector normal. For a same face, the contours are connected and they correspond to the cell of the computational model. Through the 3D geometric modeling of urban morphology, SOLENE triangulates the computational object to a shell mesh. The sky vault is considered as a hemisphere of infinite radius, with the scene to be simulated located at its center. This hemisphere is meshed with a geodesic triangulation of 4^n elements (e.g. 1024 is a good compromise between precision and speed most of the time (Miguet and Groleau, 2002)). The sky is considered as a source of diffuse energy with a non-uniform solar radiation or luminance distribution (e.g. in Fig. 4.3). Different atmosphere and cloud cover conditions are defined by two coefficients, epsilon and delta from a sky model of Perez et al. (1993). Epsilon is in the range from 1 to 12 which defines the cloud coverage (more than 6 for clear sky) and delta from 0.01 to 0.6 which defines the opacity linked to the thickness of the clouds, from highly sombre to very shiny. The information assigned to the cell is organized as a descriptor. A descriptor is a set of numerical values assigned to a single cell. Thus, each parameter describing the scene has an associated description file. In addition, for the variables over time, we need a description file per time step.

4.2.2 Thermo-radiative model

Net short-wave radiative flux The direct solar radiation is emitted by the sky in the sun direction while the diffuse solar radiation emission is distributed on all sky facets according to the sky radiance model. In a given scene, SOLENE starts the computation with view factors,

incident solar flux and inputs the albedo of each facet. From the incident short-wave radiative flux, the model calculates the total solar flux reflected by the scene and then distribute it to other facets. The contribution of a facet on others is determined by a progressive refinement method: we consider the maximal short-wave radiative flux reflected by a facet, then distribute on other facets and determine the new maximal reflected solar flux and so on. The process continues until the difference in the distribution of the solar flux reaches a threshold defined by the user (e.g. 5 W) or other convergence criteria (e.g. the number of iterations).

Net long-wave radiative flux In SOLENE, the treatment of the infrared flux is similar to the solar flux by using the progressive radiosity algorithm. The model use an empirical equation (Monteith and Unsworth, 1990) to estimate the incident infrared flux:

$$L^{\downarrow} = 213 + 5.5T_a, \tag{4.1}$$

where $L^{\downarrow}$ ($W\ m^{-2}$) and T_a (K) are respectively incoming long-wave radiation flux from the atmosphere and air temperature.

However, for the long-wave radiative flux, the facets not only absorb and reflect infrared flux but they also emit. The emission term is determined through the Stefan-Boltzmann law $\varepsilon\sigma T_{sfc}^4$

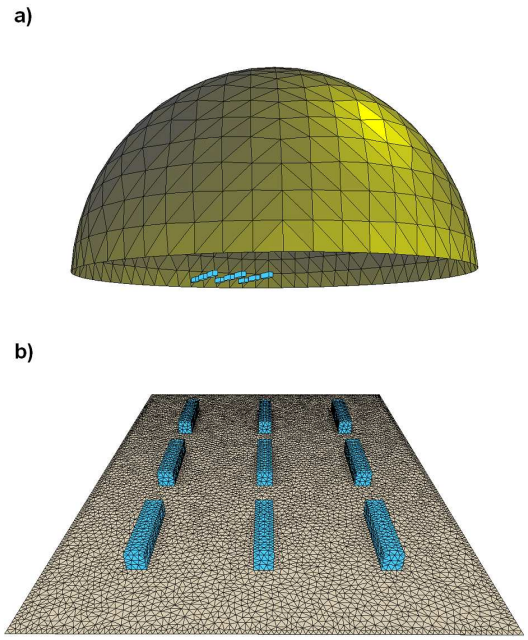

Figure 4.3: Visualization in SOLENE of: a) a dimensionless clear sky hemisphere exhibiting 1024 patches with a radiance distribution at 1500 LST; b) the triangularized shell meshing MUST geometry.

which depends on the surface temperature T_{sfc} (see Chapter 2 radiative model). SOLENE can read the atmospheric radiative fluxes and the air temperature meteorological data as input which is the case in this comparison.

Surface temperature model A multi-layers wall model (one or two layers) is implemented in SOLENE to determine temperature, over time, at the surface and inside the wall. Thus, for single layer wall, the external surface node, with $1/10$ of the heat capacity of the wall reflects the relatively rapid thermal response of external variations (air, solar and infrared radiation) while the internal node with $9/10$ of the heat capacity plays the inertial role. The two layers wall is built on the same bases.

As shown in Figure 4.4, the conductance (K) and heat capacity (C) are characteristic of the material related to the thickness of the layer (e). For the interior nodes of the layers, we consider that the conductance is identical on each side:

$$K_1 = 2\lambda_1/e_1; \;\; K_2 = 2\lambda_2/e_2, \tag{4.2}$$

where K ($W\ K^{-1}\ m^{-2}$), λ ($W\ K^{-1}\ m^{-1}$) and e (m) are respectively the conductance, the thermal conductivity and the thickness of the layer associated to the first node or second node.

The heat capacity is evaluated as:

$$C_1 = \rho_1 C_{m1} e_1; \;\; C_2 = \rho_2 C_{m2} e_2, \tag{4.3}$$

where C ($J\ K^{-1}\ m^{-2}$), ρ ($kg\ m^{-3}$) and C_m ($J\ kg^{-1}\ K^{-1}$) are respectively the heat capacity, the density and the mass-specific heat capacity associated to the node 1 or 2.

Hence, the thermal budget of each node is computed as follows (Antoine and Groleau, 1998; Hénon, 2008) for the external node *se* linking to external surface temperature T_{se} (K):

$$0.1C_1 \frac{dT_{se}}{dt} + K_1(T_{se} - T_{n1}) + Q_H + L^* = S^*, \tag{4.4}$$

where dt (s) the time step, T_{n1} (K) the temperature at node $n1$, Q_H ($W\ m^2$) the sensible heat flux estimated with equation 1.7, L^* ($W\ m^2$) and S^* ($W\ m^2$) are respectively the net long-wave and short-wave radiation flux.

For the node $s1$ linking to the surface temperature T_{s1} (K):

$$0.9C_1 \frac{dT_{n1}}{dt} + K_1(T_{n1} - T_{se}) + K_1(T_{n1} - T_{s1}) = 0, \tag{4.5}$$

for the node $n2$ linking to the internal temperature T_{n2} (K):

$$C_2 \frac{dT_{n2}}{dt} + K_2(T_{n2} - T_{s1}) + K_2(T_{n2} - T_{s2}) = 0, \tag{4.6}$$

for the node $s2$ linking to the wall temperature T_{s2} (K), not to the ground (same as in *Code_Saturne*, a constant temperature applied to deep soil)

$$K_2(T_{s2} - T_{n2}) + h_{int}(T_{s2} - T_{int}) = 0, \tag{4.7}$$

where h_i $(W\ m^{-2}K^{-1})$ is a global internal building heat transfer coefficient and T_{int} (K) the internal building temperature.

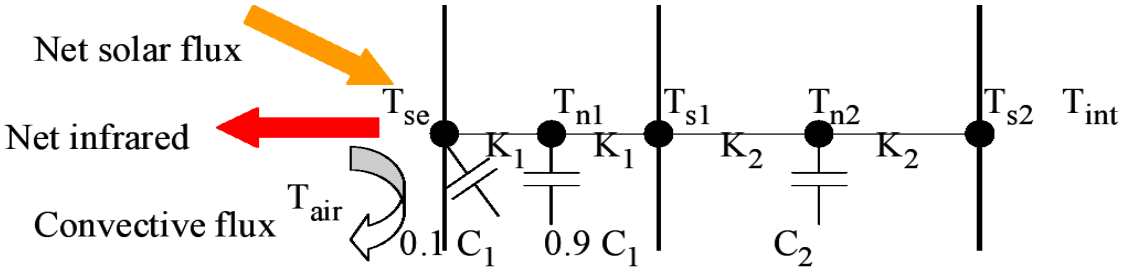

Figure 4.4: Schematic representation of the energy exchanges at an urban surface for SOLENE simulation, after Antoine and Groleau (1998); Hénon et al. (2011a). K_i and C_i represent respectively the conductance and heat capacity.

4.3 Radiation analyses

4.3.1 Set-up for radiation computation

The simulations are performed with SOLENE version 1.82. The computational effort in time and memory is not comparable. Because the two models are developed with different operating systems (Windows for SOLENE with sequential computing, Linux for *Code_Saturne* with parallel computing). Since no CFD quality criteria needs to be respected for the mesh in SOLENE, we reduced the horizontal size from MUST full radiative-dynamic coupling validation to save computational time. A standard clear sky model is created with 1024 elements for the SOLENE simulations. We set a 15 *mn* radiative time step both in SOLENE and *Code_Saturne* models. Furthermore, when we take into account the multi-refections, 5 iterations is considered for consistency in both models. Based on MUST full dynamic-radiative coupling validation case (see

Chapter 3, Table 1), we summarize the main parameters used in the simulation for the comparison in Table 4.1. We keep in mind that all the following comparisons are for the center building in the domain.

4.3.2 Comparison of direct solar flux

We start with the comparison of direct solar flux before and after multi-reflection by the urban canopy. Through Figure 4.5a, 4.5b, we find that the two models agree quite well with each other. The estimation of the direct solar flux is slightly higher (by less than 10%) for the SOLENE model with and without multi-reflection. These relatively slight visible differences appear only at the south wall (SE and SW faces) and roof which are the most exposed to the sun during the daytime. Moreover, it seems that SOLENE model has a small delay on sunrise. This may be due to the difference on the accuracy of estimating the time of sunrise and the precision of the specified latitude.

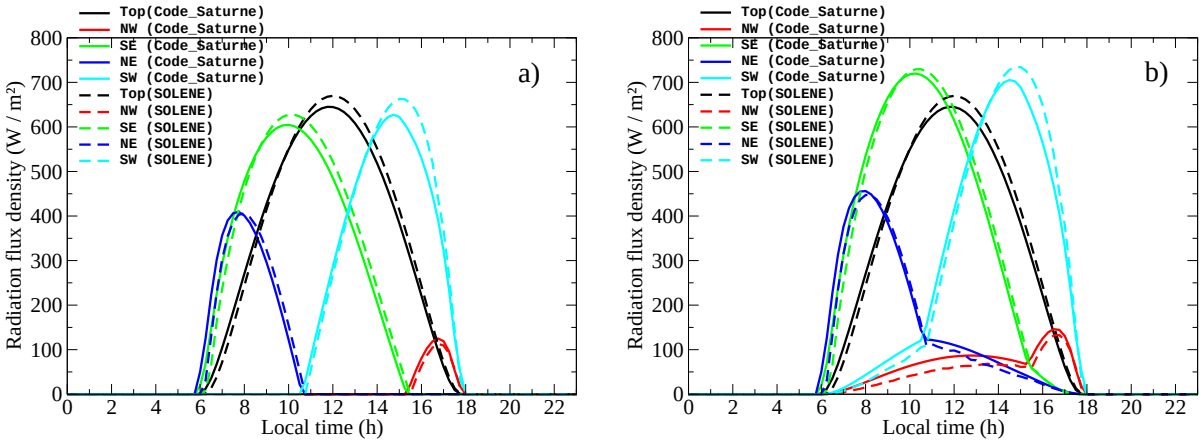

Figure 4.5: Comparison for the central container of the MUST field experiment of direct solar radiation flux on roof (top), N-W, S-E, N-E and S-W walls during a diurnal cycle between *Code_Saturne* (Solid lines) and SOLENE (Dashed lines): a) incident direct solar flux; b) direct solar flux after multi-reflections.

Table 4.1: Parameters used in the comparison between *Code_Saturne* and SOLENE for MUST simulations; α_S, α_W and α_R are respectively the short-wave albedo of soil, walls and roofs; ε_S, ε_W and ε_R are respectively the long-wave emissivity of soil, walls and roofs; λ_S, λ_W and λ_R are respectively the thermal conductivity of soil, walls and roofs; e is the thickness; T_{air} the initial air temperature; T_S and T_{Sint} are respectively the initial soil temperature and deep-soil temperature; T_{Top}, T_{NW}, T_{SE}, T_{NE} and T_{SW} are initial individual surface temperature; T_{Wint} and T_{Rint} are respectively building and roof internal temperature; h_f is the heat transfer coefficient; C_p is the specific heat capacity; ρ is the density; h_{int} is the internal transfer coefficient.

Parameter	Unit	Value
Time-step	*min*	15
α_S		0.55
$\alpha_W = \alpha_R$		0.1
ε_S		0.8
$\varepsilon_W = \varepsilon_R$		0.13
$\lambda_W = \lambda_R$	$W\ K^{-1}\ m^{-1}$	6
λ_S	$W\ K^{-1}\ m^{-1}$	0.75
Wall e = Roof e = Soil e	m	0.1
Initial values		
T_{air}	°C	16.45
T_S	°C	15.88
T_{Sint}	°C	24.28
T_{Top}	°C	9.28
T_{NW}	°C	10.50
T_{SE}	°C	11.68
T_{NE}	°C	11.87
T_{SW}	°C	12.37
$T_{Wint} = T_{Rint}$	°C	11.11
Top h_f	$W\ m^{-2}\ K^{-1}$	25.32
NW h_f	$W\ m^{-2}\ K^{-1}$	10.08
SE h_f	$W\ m^{-2}\ K^{-1}$	10.83
NE h_f	$W\ m^{-2}\ K^{-1}$	20.29
SW h_f	$W\ m^{-2}\ K^{-1}$	17.79
Soil h_f	$W\ m^{-2}\ K^{-1}$	51.76
Additional values for SOLENE		
Wall C_p = Roof C_p	$J\ m^{-3}\ K^{-1}$	650
Soil C_p	$J\ m^{-3}\ K^{-1}$	800
Wall ρ = Roof ρ	$kg\ m^{-3}$	7000
Soil ρ	$kg\ m^{-3}$	1600
h_{int}	$W\ m^{-2}\ K^{-1}$	1000

4.3.3 Comparison of diffuse solar flux

With regard to the diffuse solar flux the differences between SOLENE and *Code_Saturne* are significant (Fig. 4.7a), in particular at the four walls, where *Code_Saturne* model predicts the same average diffuse solar flux (superimposed lines in Fig. 4.7a). This can be explained by the fact that the simple clear sky model, Bird Clear Sky model (Bird and Hulstrom, 1981), implemented in *Code_Saturne* assumes the homogeneous and isotropic intensity distribution of diffuse solar flux at inlet boundaries (see Chapter 2 section 2.3.3.c).

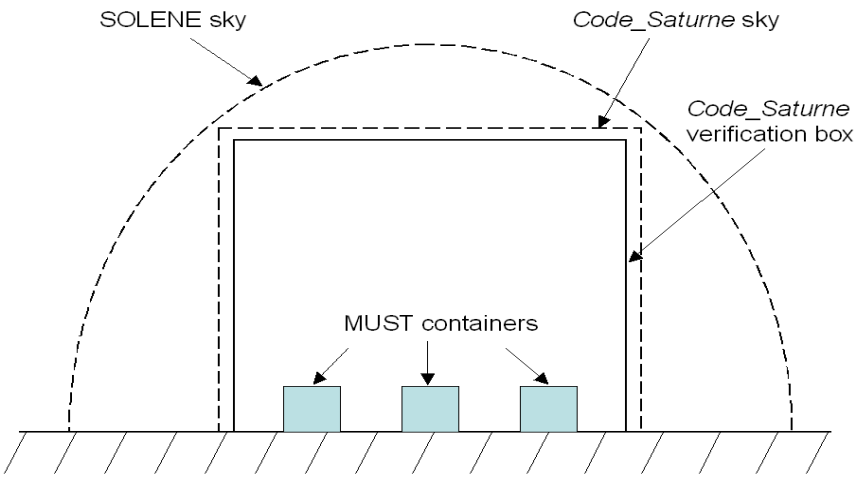

Figure 4.6: Schematics of the procedure to impose the SOLENE values of diffuse solar flux as boundary conditions in *Code_Saturne*. The verification box is used to check the calculated values in *Code_Saturne*.

In order to analyze the difference further we have introduced the SOLENE inhomogeneous diffuse solar flux as the boundary conditions in *Code_Saturne*, using the following procedure (Fig. 4.6):

1. In SOLENE, we create a 'rectangular building' as large as the computational domain of *Code_Saturne* (box with dashed lines in Fig. 4.6) and afterwards, compute the average diffuse solar flux for each face of this large building using SOLENE.

2. Make a second large 'rectangular building' which is just a little smaller ($-1m$) than the previous one which will be used as verification box for both SOLENE and *Code_Saturne* (box with full lines in Fig. 4.6). Use the average diffuse flux value from the previous step as inlet boundary conditions for each boundary of the computational domain in

Code_Saturne. Compute the diffuse flux for each face of the second building in SOLENE and *Code_Saturne* (box with full lines in Fig. 4.6). Compare the results to check if the boundary condition is correctly set in *Code_Saturne* (Fig. 4.7b).

3. Apply the diffuse flux value from SOLENE to the MUST reference geometry in *Code_Saturne* (small blue boxes in Fig. 4.6) and compare the values for the container walls (Fig. 4.7(c)).

As shown in Figure 4.7b, taking the average diffuse solar flux value from SOLENE as inlet boundary condition gives a very good agreement between SOLENE and *Code_Saturne*. However, the comparison for the container walls is not enough as satisfactory as expected. As shown in Figure 4.7c, the diffuse flux of each side of the wall reproduced by *Code_Saturne* differ a lot. Only the roof matches well, but all the sides wall exhibit over- or under-estimation. One reason for this maybe due to the different numerical methods implemented in two models. Our numerical scheme is diffusive, especially in transparent medium case (see Fig. 6 in Chapter 3). Another reason can be explained by recalling that the Discrete Ordinates Method has a quite limited angular at any discretization resolution (32 or 128 directions in *Code_Saturne*). Since the incident diffuse radiation is restricted to propagate in a finite number of directions with an angular sector width (128 directions in this case) from the boundary into the domain, they may not all reach the vertical building surfaces but somewhere else in the domain, except for the roof which is a horizontal surface and at the highest level can receive the diffuse flux from all the directions. This is also proved by the result shown in Figure 4.7b where the distance from boundary to building surface is very short. Since the direct solar flux is unidirectional, the distance between the building and the boundary does not have the same influence on the results in *Code_Saturne* (Fig. 4.5).

Nevertheless, using the diffuse flux value from SOLENE in *Code_Saturne* still shows an improvement. Moreover, since the diffuse solar flux value is much smaller than the direct flux in clear sky condition, thus it plays a minor role in the surface energy balance.

4.3.4 Comparison of long-wave radiation flux

Since the observation of the 180° incident long-wave radiation flux is available in the MUST data, we use it as sky boundary conditions for both *Code_Saturne* and SOLENE. Moreover, due to the long-wave radiative emission highly depends on the surface temperature (Eq. 1.6)

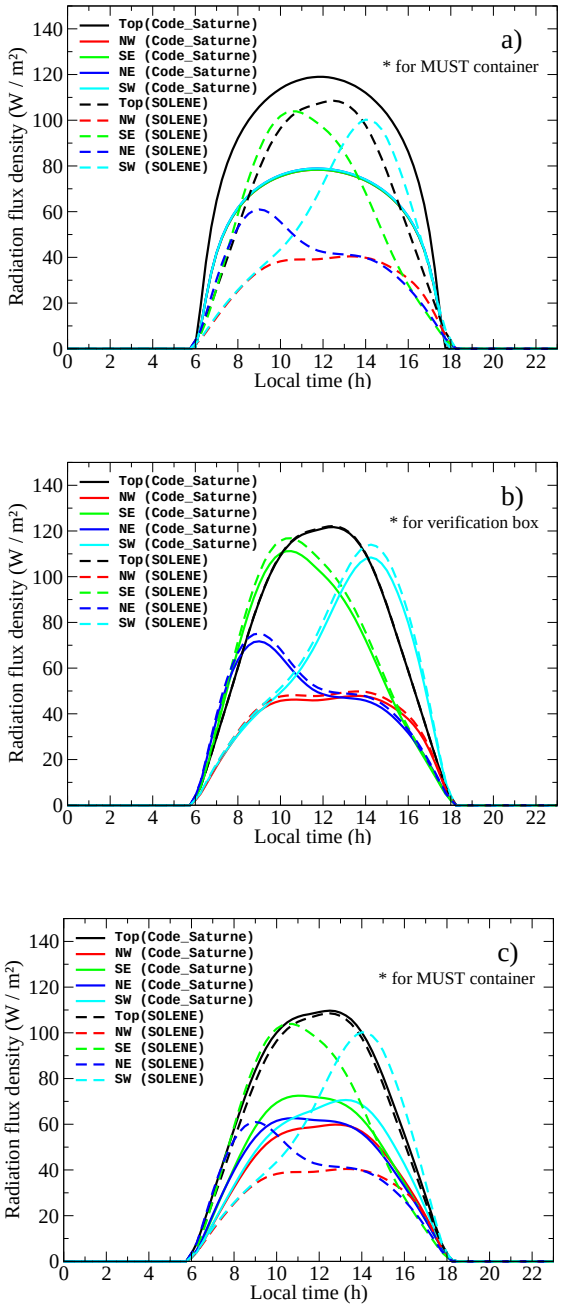

Figure 4.7: Comparison between SOLENE and *Code_Saturne* for incident diffuse solar flux: a) for the container walls with Bird Clear Sky model in *Code_Saturne*; b) using the SOLENE diffuse flux values from SOLENE model as boundary conditions to the *Code_Saturne* for walls of the verification box (see Fig. 4.6); c) for the container walls with SOLENE boundary conditions applied in *Code_Saturne*.

which introduces more complexities (see next section), here we compare only the output of the average incident long-wave radiation flux at each face of the building for the two models. Figure 4.8 indicates that the prediction of the incident long-wave radiation agrees very well with two models (black dashed line and black solid line are superimposed.). The average incident long-wave radiation flux on the four sides of building wall exhibits an isotropic behavior (solid/dashed lines are all superimposed and solid lines are very close to dashed lines). Unlike the distribution of the diffuse solar flux which depends on the position of the sun, the distribution of the incident infrared flux at each boundary is isotropic. Therefore the symmetric building geometry makes each wall receive the same quantity of the average infrared flux. Thus, *Code_Saturne* calculates the incident infrared radiation as well as SOLENE.

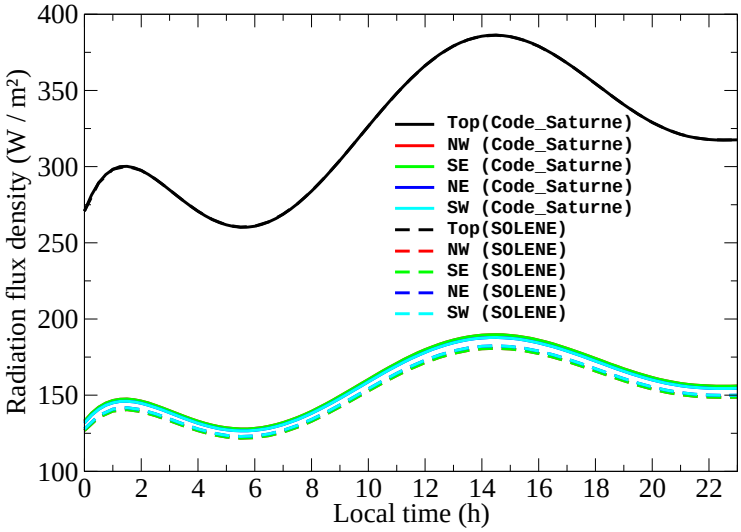

Figure 4.8: Same as Fig. 4.5 but for incident long-wave radiation flux.

4.3.5 Comparison of surface temperatures

Up to now, we have compared the atmospheric radiation flux term by term. Since the primary aim of our radiative model is to calculate the exterior surface temperatures of the facets, finally we discuss the prediction of the surface temperatures by the two models. Focusing on radiative aspects, the computation of the sensible heat flux is strongly idealized for this test. The simulations are based on a given constant h_f for each face of the buildings and ground every two hours. The constant h_f values are obtained by averaging the result of our dynamic-radiative

full coupling model in moderate wind condition (see Chapter 3). Thus, no conservation equations for mass, momentum and energy are solved and therefore the influence of a model other than the radiation model can be excluded. We use the wall thermal model from *Code_Saturne* (see Chapter 2) and consider one-layer wall from SOLENE to calculate the surface temperature. The air temperature and incident long-wave radiation are directly imposed from meteorological data. Since the influence of the internal building temperature on the external surface temperature is quite important in the MUST case (see Chapter 3), we update the diurnal variation of the interior temperature every half hour. Furthermore, we estimate the values for the specific heat capacity C_p and the density ρ in SOLENE (Tab. 4.1) which are close to the MUST experimental field. In the SOLENE models the internal building energy balance, and the internal transfer coefficient h_{int} must to be set. In order to keep an equivalent heating configuration, after testing some values of h_{int} (e.g. 10, 100, 1000) in SOLENE, we find that the higher h_{int} is, the better the agreement with the surface temperature. Thus, h_{int} is set to 1000.

Figure 4.9 displays the time evolution of modeled surface temperatures using the *Code_Saturne* and SOLENE, and the observation data as reference. As mentioned above, the h_f is only changed every two hours for this moderate wind speed case, this simplification miss the variations of the wind. As a consequence, the corresponding surface temperature profile may change sharply. This undesired behavior is more remarkable from the simulation of *Code_Saturne* (e.g. NE face in Fig. 4.9c). Overall, the mean surface temperatures are rather well reproduced by both models. The diurnal cycle is also well simulated and the variability of the two models and the observations are comparable. On the other hand, this good result is also consistent with the ability of our full dynamic-radiative coupling to estimate good average h_f values.

The surface temperature is better simulated by *Code_Saturne* with a bias smaller than 5°C. This may be due to a lack of information on some thermal properties in the experiment. The estimated parameters in the simulation might be better adapted for the one-layer wall thermal model in *Code_Saturne*. Additionally unknown parameters (C_p and ρ) used in SOLENE may lead to more uncertainties. However, it can be seen that SOLENE overestimate the surface temperatures starting from the middle of the day. This behavior of the model is probably associated with a strong contribution of the thermal inertia leading to a delay in warming with storage in the morning then heat releases from the middle of the day.

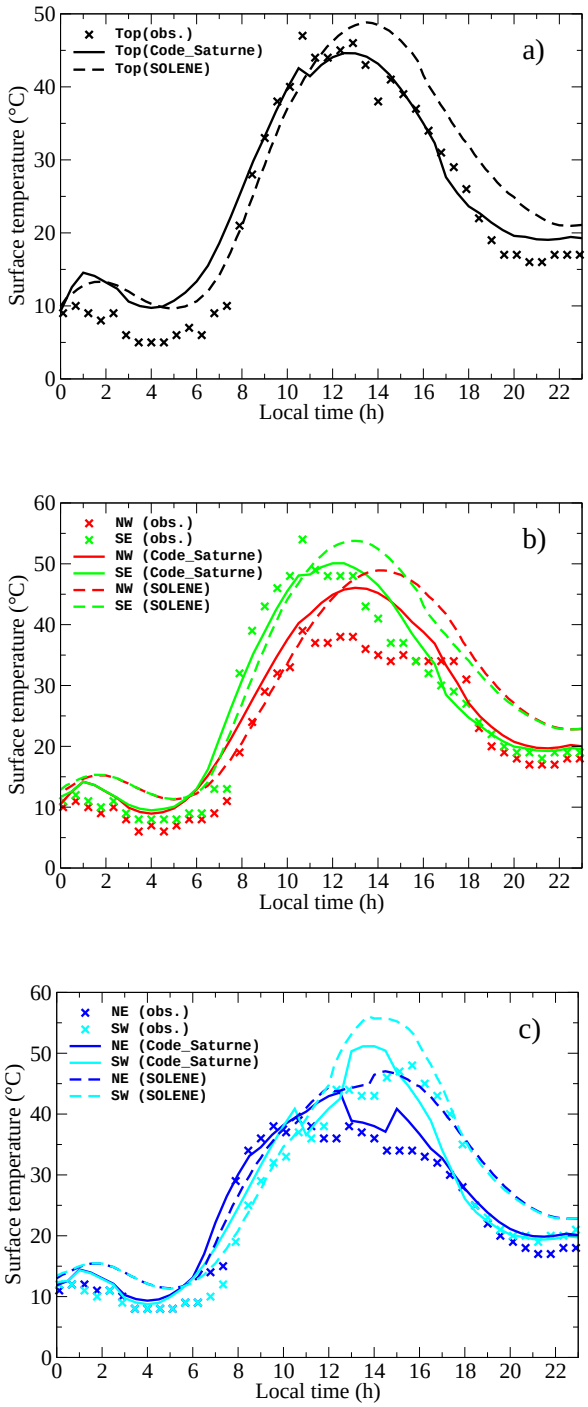

Figure 4.9: Evolution of surface temperature of different faces of the central container in MUST field experiment during a diurnal cycle (cross symbol: Measurements; Solid lines: Simulation with *Code_Saturne*; Dashed lines: Simulation with SOLENE).

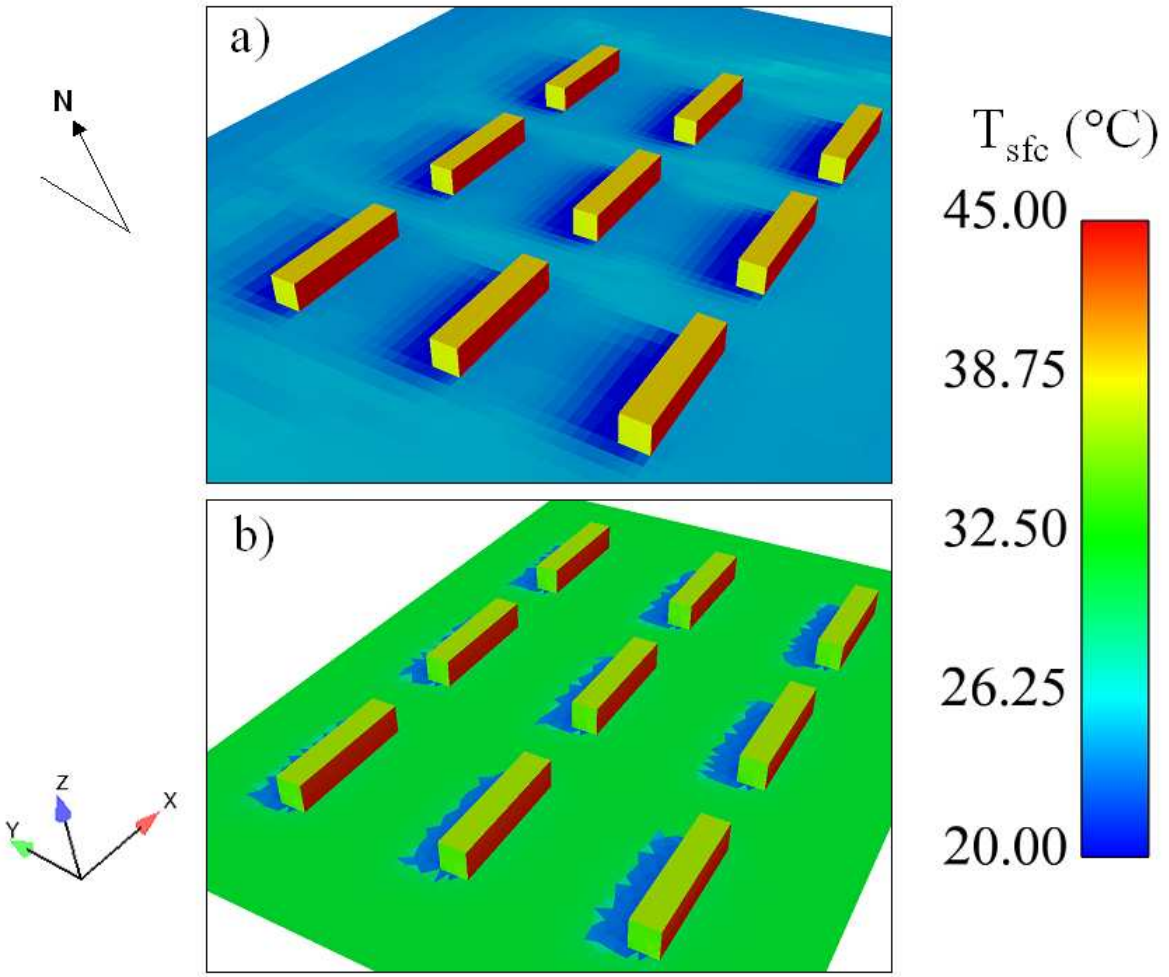

Figure 4.10: Comparison of two radiative models with visualization of surface temperatures (T_{sfc}) (°C) of ground, roof, SE and NE wall at 1000 LST: a) *Code_Saturne*; b) SOLENE.

In addition, both *Code_Saturne* and SOLENE can produce a visualization of the 3D field. For instance, the distribution of the surface temperatures at 1000 LST is pictured in Figure 4.10. The visualization of the building temperatures is consistent with the above discussion. Moreover, the ground temperature reproduced by SOLENE (Fig. 4.10b) is higher than by *Code_Saturne* (Fig. 4.10b) ($\sim> 5°C$). The degradation of the shadow seems more observable from *Code_Saturne* than from SOLENE. This is due to the chosen color scale and by recalling that our scheme has an additional numerical diffusion. Difference with the MUST shipping container surface temperatures are highly dependent on the evolution of the internal temperature, the diurnal variation of the deep ground temperature being insignificant. So one reason for the ground to appear warmer in SOLENE maybe the estimation of the value of C_p and ρ for the soil. By using an one-layer wall scheme, they may be sensitive to the solution of the ground temperature in SOLENE for this particular case.

4.4 Conclusions and perspectives

In this study, we have compared the atmospheric radiation fluxes and the container walls surface temperature simulated by *Code_Saturne* and SOLENE models with the MUST experimental data set. It has been found that both two models give similar mean daily cycle of radiation fluxes. For the direct solar flux and incident infrared flux, *Code_Saturne* is in very good correspondence with the SOLENE model. The prediction of the diffuse solar flux by the Discrete Ordinate Method of *Code_Saturne* is poorer, due to an assumption of isotropy uniform sky and the different characteristics of the numerical method. One perspective is to implement a similar sky model as SOLENE in *Code_Saturne* to take into account the non-uniform of the distribution of the diffuse solar flux at inlet boundaries. The diffuse flux reproduced by *Code_Saturne* in this chapter has already used the higher angular resolution (128 directions) in the current model. It may be worth to test by increasing much more the angular resolution in the model to get some improvements.

Concerning the surface temperature, with imposed heat transfer coefficients, the average diurnal cycle of the surface temperature of different building sides is well reproduced by both models. The difference between two models is more significant from afternoon. For this reason, the comparison of the emission and reflection of the IR flux reproduced by two models are not discussed because of high dependance on the surface temperature. Incertitude related to

additional thermal parameters, C_p and ρ, is more pronounced for the ground temperature in SOLENE. Both of them have facility to the visualization of the 3D field. They can be useful tools for simulating the outdoor thermal environment.

Further, only one-layer wall thermal model is tested here. Using a multi-layer scheme and including C_p and ρ with more detailed information on properties of the material may be appropriate to compare SOLENE and *Code_Saturne*. In case where the diffuse flux data is not available or in cloudy sky weather conditions, calculating the diffuse flux value from SOLENE with a domain size box then set as inlet boundary conditions lead to improvements in *Code_Saturne* results. Conversely, using a CFD code to more accurately model the h_f is helpful to SOLENE for predicting the sensible heat flux under moderate wind speed condition.

CHAPTER 5

Numerical study of the thermal effects of buildings on low-speed airflow taking into account 3D atmospheric radiation in urban canopy: paper submitted to Journal of Wind Engineering & Industrial Aerodynamics

---

In the two previous chapters, we discussed the impact of the convective flux on the surface temperatures by modeling a detailed wind field. Then, on the radiation aspect, we discussed the performance of the radiative model in comparison to SOLENE model. In this submitted paper, in order to improve the model, we extend the work of Chapter 3 and 4. We present different numerical simulations for low wind speed and higher building density than in MUST, varying the thermal exchange model and analyzing the differences. On one hand, this assess the thermal impact on the flow field in different conditions. On the other hand, it illustrates the use of the 3D radiative scheme.

Numerical study of the thermal effects of buildings on low-speed airflow taking into account 3D atmospheric radiation in urban canopy

Yongfeng QU[1,*], Maya MILLIEZ, Luc MUSSON-GENON and Bertrand CARISSIMO

CEREA, 6-8 avenue Blaise Pascal, 77455 Champs-sur-Marne, France

Abstract

A three-dimensional atmospheric radiative model which enables to evaluate the thermal-radiative transfers in the lower atmosphere was implemented in the atmospheric module of a Computational Fluid Dynamics code. This model can study the thermal effects of buildings on the local atmospheric flow with a coupled dynamic-radiative model. Previously, we have validated this approach by comparison with several surface wall temperatures from the Mock Urban Setting Test experiment. This paper presents idealized simulations with a lower wind speed and a higher building density and discusses the impact of albedo (dark/white walls). In order to further analyze the contribution of the 3D radiative transfers, a comparison of the thermal impact on the airflow under different thermal conditions for the ground and the walls is made: no heating, imposed temperatures and 3D radiative transfer heating. The results show that taking into account the

[*]Corresponding author. Tel. +33 130877217
Email address: yongfeng.qu@cerea.enpc.fr (Yongfeng QU)
[1]CEREA Teaching and Research Center in Atmospheric Environment, (Ecole des Ponts ParisTech / EDF R&D)

thermal stratification has a significant influence on the wind field. The difference between the imposed temperatures case and the 3D radiative transfer case can also be important. Furthermore, the influence of the different radiative transfer conditions and parameters are also discussed: a 0900 LST sun position with an albedo of 0.1 for the building walls, a 0900 LST sun position with an increased value of the albedo (0.6) and a 1600 LST sun position with an albedo of 0.1 are compared.
Keywords: Thermal transfer, 3D atmospheric radiation, Computational Fluid Dynamics, Urban canopy

1. Introduction

The influence, on the airflow pattern, of the incident atmospheric radiation on the canyon walls and ground surfaces under conditions of low wind speed can be important and should not be neglected in pollutant dispersion or urban design studies. Solar heating of the building walls and the ground during the day warms the air near the wall or above the ground, which can cause strong thermally induced air motion. This thermal effects on the airflow, including building geometry and architecture as well as street canyon dimensions, have been mainly studied with wind-tunnel experiments (Uehara et al., 2000; Kovar-Panskus et al., 2002; Richards et al., 2006) and numerical models (Sini et al., 1996; Kim and Baik, 2001; Louka et al., 2001; Xie et al., 2007) and fewer with full-scale or near full-scale experiments (Louka et al., 2001; Kanda, 2006; Niachou et al., 2008). In general, field and wind-tunnel experimentalists stress the technical difficulties in controlling air and surface temperatures and various air or surface temperatures gradients. Moreover, in order to obtain significant thermal effects and respect the similarity with a real building, usually a very high surface temperature

($100 - 400\ ^{\circ}C$) has to be applied in wind-tunnel experiments (Uehara et al., 2000; Kovar-Panskus et al., 2002; Richards et al., 2006).

To overcome this limitation, numerical studies were performed. Sini et al. (1996) first numerically showed that the thermal forcing could markedly influence the air motions and the wind structure. Later, Kim and Baik (2001) simulated the flow in an urban street canyon with various aspect ratios and with street bottom heating using a two-dimensional (2D, hereafter) Computational Fluid Dynamics (CFD, hereafter) model with a k-ε turbulence closure. Kovar-Panskus et al. (2002) identified the differences in the airflow regimes between the cases with and without wall heating. Xie et al. (2007) investigated the influence of the multi-surface heating configuration on the flow field and pollutant transport problems with the wind-tunnel experiment of Uehara et al. (2000).

However, most of previous research works considered a 2D computational domain and assumed idealized sunlit wall configurations (uniform sunlight on one surface of the canyon and no sunlight on any other solid surfaces) without including a realistic radiative model. Further research work is therefore necessary to improve our knowledge about the thermal effects on local atmospheric environment. On the basis of this background, the aim of this work is to perform three-dimensional (3D, hereafter) numerical simulations in order to evaluate the effects of non-uniform wall-heating on the airflow pattern using a 3D radiative model developed in the CFD code *Code_Saturne* which is adapted to complex geometry. Milliez (2006) first evaluated the model with idealized cases, using a constant 3D wind field. Then, Qu et al. (2011) compared this model with measurements of surface temperature for different wall orientation in the Mock Urban Setting Test (MUST, hereafter) field campaign (Yee and Biltoft, 2004; Milliez and Carissimo,

2007). They have also discussed the influence on the surface temperatures of the internal building temperature and the wall thermal modeling, and compared the 3D modeling of the convective exchanges to simpler approaches used in other models. In this paper, we extend the work of Qu et al. (2011) to lower wind speed and a higher building density than in MUST. First, we briefly describe the model and discuss the thermal exchange modeling of buildings. Then we present different numerical simulations for low wind speed in this idealized urban area with a high building density, varying the thermal exchange model and analyzing the differences.

2. Equations and Model design

The model used in this study is the open-source CFD code *Code_Saturne* (Archambeau et al., 2004) which can handle complex geometry and physics. Taking into account the larger scale meteorological conditions and the thermal stratification of the atmosphere, the atmospheric module of *Code_Saturne*, described in Milliez and Carissimo (2007), uses a detailed representation of the surfaces allowing a complex 3D spatial representation of wind speed, turbulence, and temperature. The numerical solver employs a finite-volume approach for co-located variables on an unstructured mesh. Time discretization is achieved through a fractional step scheme, with a prediction-correction step. In our simulations, the turbulence in the entire fluid domain is parameterized with the standard $k-\varepsilon$ formulation.

2.1. Surface energy balance

To take into account the thermal effects of buildings, we model the surface energy balance (SEB, hereafter). In this study, we neglect the anthropogenic heat

flux and the latent heat flux. The advection fluxes are obtained by the resolution of the entire flow field. Thus, for each surface the SEB is expressed as:

$$Q_{cond} + Q_H = Q^*, \tag{1}$$

where Q_{cond} is the conductive heat flux ($W\ m^{-2}$) within the building or the ground subsurface, which links the surface temperature to the internal building or the deep soil temperature, Q_H is the sensible heat flux ($W\ m^{-2}$) which depends on the local airflow intensity, Q^* is the net radiative flux ($W\ m^{-2}$).

2.2. Radiative model: Q^*

2.2.1. Solar and infrared radiation

The net atmospheric radiation Q^* is the net or resultant value of the short- and long-wave radiation. The total incoming and outgoing short-wave radiative fluxes for each solid surface are expressed as:

$$S^{\downarrow} = S_D + S_f + S_e, \tag{2}$$

$$S^{\uparrow} = \alpha S^{\downarrow}, \tag{3}$$

where $S^{\downarrow}$ and $S^{\uparrow}$ are respectively the incoming and outgoing short-wave radiative fluxes ($W\ m^{-2}$), S_D the direct solar flux ($W\ m^{-2}$), S_f the solar flux diffused by the atmosphere above our simulation domain ($W\ m^{-2}$), S_e the flux diffused by the environment, i.e. resulting from the multi-reflections on the other sub-facets ($W\ m^{-2}$) and α the albedo of the surface.

Then, the long-wave radiation flux for each surface reads:

$$L^{\downarrow} = L_a + L_e, \tag{4}$$

$$L^{\uparrow} = \varepsilon\sigma T_{sfc}^4 + (1-\varepsilon)(L_a + L_e), \tag{5}$$

where $L^{\downarrow}$ and $L^{\uparrow}$ are respectively the incoming and outgoing long-wave radiative fluxes ($W\ m^{-2}$), ε the emissivity of the surface, σ the Stefan-Boltzmann constant ($5.66703 \times 10^{-8}\ W\ m^{-2}\ K^{-4}$), T_{sfc} (K) the surface temperature, L_a ($W\ m^{-2}$) and L_e ($W\ m^{-2}$) are respectively the long-wave radiation flux from the atmosphere and from the multi-reflection on the other surfaces.

2.2.2. Discrete Ordinate Method (DOM)

The radiative fluxes are computed using the Discrete Ordinate Method (DOM) (Fiveland, 1984; Truelove, 1987; Liu et al., 2000) which solves the radiative transfer equation for a gray non-diffusive semi-transparent media by the directional propagation of the radiative wave. In our models, the angular discretization has two resolutions: 32 or 128 directions and the spatial discretization uses the same mesh as the CFD model. Taking into account both short- and long-wave radiation separately, we have adapted a radiative heat transfer scheme available for combustion in *Code_Saturne*. Described in detail by Milliez (2006), the new atmospheric 3D radiative approach was developed in *Code_Saturne* for built-up areas. The main advantage of this model is that the radiative transfer equations is solved in the whole fluid domain and not only at solid faces (such as when using view factors), but also can be applied to non-transparent media (e.g. fog or pollution). In this work, we consider a transparent atmosphere between the building at the microscale of our simulations.

2.3. Convective model: Q_H

The sensible heat flux Q_H term in the equation (1) is calculated from:

$$Q_H = h_f(T_a - T_{sfc}), \tag{6}$$

with h_f is the heat transfer coefficient ($W\ m^{-2}K^{-1}$). T_a (K) is the external air temperature.

In order to effectively model airflow features, the estimation of the stratification effects on vertical turbulent transport and the surface-air thermal gradient that controls convective heat transfer are determined from the thermal energy equation of the flow. In our simulations, momentum and heat transfer from horizontal surfaces follows a rough wall law modified by stratification. Convection from vertical surfaces defaults to the neutral wall law. Depending on the local friction velocity u_* (ms^{-1}) and the thermal stratification, the local heat transfer coefficient h_f for each solid sub-facet is defined here as:

$$h_f = \frac{\rho C_p u_* \kappa f_h}{\sigma_t ln(\frac{d+z_0}{z_{0_T}})\sqrt{f_m}}, \tag{7}$$

where ρ is the flow density ($kg\ m^{-3}$), C_p the specific heat ($J\ kg^{-1}\ K^{-1}$), κ is the von Karman constant, σ_t the turbulent Prandtl number, d is the distance (m) to the wall, z_0 is the roughness length (m), z_{0_T} is the thermal roughness length (m), f_m and f_h are the Louis (1979) stability dependent surface layer functions.

2.4. Modeling surface temperature: wall thermal model Q_{cond}

As shown in equation (1), the solution of the surface energy balance for each surface cell at each time step requires the calculation of the heat conduction (Q_{cond}) which links the internal temperature to the surface temperature. Conduction between surface layers spatially varying in thickness e (m) and thermal conductivity λ ($W\ K^{-1}\ m^{-1}$), as typical for building walls, necessitates a sophisticated approach. Yet, the simulations are short-term in this study. So we adopted one-dimensional conduction scheme with an average thermal conductivity of the

wall and a constant value to the internal building temperature T_{int} (K). Hence, the solution for the surface temperature is calculated from:

$$\frac{\lambda}{e}(T_{sfc}-T_{int})+h_f(T_{sfc}-T_a)=\varepsilon(L_a+L_e-\sigma T_{sfc}^4)+(1-\alpha)(S_D+S_f+S_e), \quad (8)$$

where the heat transfer coefficient h_f is computed from local flow parameters as shown in equation (7).

3. Numerical simulations set-up: initial and boundary conditions

The computational domain is three-dimensional (Fig. 1) and a Dirichlet boundary condition is applied at the inlet (East) and the top, a symmetry condition at the lateral boundaries (North and South) and free outflow at the outlet (West) boundary. The buildings have the same dimensions ($L \times W \times H$: $12.2 \times 2.42 \times 2.54$ m) as the MUST experiment shipping containers (Yee and Biltoft, 2004; Milliez and Carissimo, 2007; Qu et al., 2011) and the orientation of the canopy is -90° relative to the geographic north. In addition, we modified the aspect ratio (H/W, where H is the building height and W is the along-wind spacing) to 1 in order to increase the density of the urban canopy and therefore to emphasizing the thermal impact on the wind. The run takes place from 0900 LST to 0910 LST. The meteorological initial and inlet boundary conditions are a neutrally stratified logarithmic wind profile blowing westward, associated with a neutral potential temperature profile of 30 °C with both dynamical and thermal roughness lengths set to 4 cm. Since the thermal effects are expected to be of substantial importance for low wind speeds, certainly below 3 ms^{-1} when the urban dome regime dominates (Oke, 1987; Kovar-Panskus et al., 2002), the 10 m high wind speed is set to 1 ms^{-1}. Low wind conditions and large surface-air temperature differences cause

large thermal effects. Different differential temperatures between the heated surfaces and the air were simulated in numerical studies (5 °C in Sini et al. (1996), 10 °C in Xie et al. (2007), 32 °C between the windward wall and the air, 53 °C between the leeward wall and the air in Onomura et al. (2009)). In general, a surface-air temperature difference of 5 to 10 °C is considered to be close to the one of a wall heated by solar radiation. Thus, in our study, the initial air, soil and wall/roof temperatures are set to 30, 32 and 36 °C respectively.

In order to study the contribution of atmospheric radiation on the airflow, we simulated three cases: a reference case without heat transfer, i.e. with a neutral stratification of the atmosphere - called hereafter 'neutral case', a case with heat transfer but where the surface temperatures are imposed - called hereafter 'imposed temperatures case', and a case with the 3D atmospheric radiative model coupled to the dynamical one - called hereafter 'radiative transfer case'.

For the second case, the imposed wall/roof temperature is set to the one used to initialize the surface temperatures in the radiative transfer case (36 °C). For the ground, two imposed temperatures are used, which are obtained by averaging the results of the radiative transfer case: one (lower) for the ground inside the canyons (11.30 °C) (in order to take into account the shading effects) and another one for the area outside the array (35.15 °C).

After a sensitivity study, the time-steps for the dynamical model and the radiative one were respectively set to 0.05 *s* and 2 *min*. In the two last cases, a buffer zone is included to remove any numerical perturbation due to the difference between the ground-level temperature of the inlet meteorological profile and the imposed or initial ground temperature inside the domain. The numerical simulation features, including initial and wall boundary conditions are summarized in

Table 1.

4. Results and discussion

The numerical simulation results are analyzed at $t = 600s$, when the mean flows in the entire simulated urban canopy reaches a quasi-steady state. Figure 2 presents at 0900 LST the direct solar flux received by the surfaces from the radiative model. We observe that the distribution of the shadow in the canyons is mainly behind the leeward walls and the most heated walls are at windward sides.

4.1. Comparison of three thermal conditions: neutral, imposed temperatures and 3D radiative transfer cases

Figure 3a and b show the mean Turbulent Kinetic Energy (TKE, hereafter) fields at roof level and half building height level for three thermal conditions. In all conditions, due to the presence of the buildings creating mechanically induced turbulence, more TKE is found at roof level than in the canopy. Compared to the neutral case (Fig. 3a.1, b.1), the presence of heat transfer (Fig. 3a.2, a.3, b.2, b.3) enhances the TKE in the whole domain due to a large thermal production, in particular near the windward side of the first array (the most heated wall) and in the wake zone (accumulated thermal production). Similar TKE distributions in the street canyons are found in the two cases with heat transfer (Fig. 3a.2, a.3, b.2, b.3) due to surface temperatures on the same order of magnitude, generating similar thermal production. However, the non-uniform surface heating in the radiative transfer case shows an asymmetry in the TKE distribution. This asymmetry obviously shows smaller values in the center and larger values on the right side of the wake zone.

The asymmetrical TKE distribution and the larger TKE in the wake zone can be better understood by looking at the dominating vortex structure in the cross-section $5H$ behind the array, as shown in Figure 4. Consistent with Figure 3a, three different vortex regimes are found above the roof (Fig. 4), with larger TKE values in the case with heat transfer (Fig. 4.2 and Fig. 4.3). In comparison to neutral and imposed temperatures cases (Fig. 4.1 and Fig. 4.2), involving shadowing and radiation trapping effects in the radiative transfer case induces a different TKE contour in the right side part of the wake zone (Fig. 4.3).

The motion in the canyon induced by thermal effects is substantially vertical. Figure 5 compares the distribution of the mean airflow potential temperature and velocity vector maps for the three cases. Velocity vectors are normalized by the reference velocity (i.e. 1 ms^{-1}) and projected onto the center-plane. Without surface heating (neutral case, Fig. 5.1), due to the building density ($H/W = 1$), the airflow pattern in the canopy is a classic skimming flow regime as described by Oke (1987): a clockwise wind flow structure develops in the center of the street canyon. Taking into account surface heating (either imposed temperatures or radiative transfer conditions), the potential temperature is increased mainly at the roof level and windward wall (Fig. 5.2 and Fig. 5.3). As a result, the airflow structure is characterized by a significant air motion along the windward faces in the cavities. As mentioned previously, the initial ground temperature outside the canyon in the imposed temperatures case is set to a constant value (35.15°C) estimated by averaging the results of the radiative transfer computation. In fact, in the radiative transfer case, the ground temperature close to the first building is higher (+2°C) as a result of short- and long-wave reflections and long-wave emissions between the soil and the first windward face. Behind the last building,

the soil temperature in the shaded area is much lower in the radiative transfer case ($12-24^{\circ}$C not shown here) than in the imposed temperatures case (35.15°C), which results in significant difference in potential temperature.

To further investigate the contribution of the radiative model, Figure 6 shows the vertical velocity difference (Fig. 6.1) and the potential temperature difference (Fig. 6.2) in the center-plane between the radiative transfer case and the imposed temperatures case. We notice that taking into account the non-uniform surface heating by 3D atmospheric radiation transfer can substantially modify the distribution of the vertical velocity and potential temperature patterns in the streets, in comparison to simply setting constant surface temperatures: close to the leeward sides, the differences are between -0.3 and $0.05 m\,s^{-1}$ for the vertical airflow pattern, and between -2 and 1.5°C for the potential temperature in our study case (Fig. 6).

4.2. Comparison of the different radiative transfer conditions

Up to now, we have seen that the difference between the imposed temperatures and the radiative transfer case is already complex. In fact, depending on the position of the sun and the shadows, the walls and the soil are not heated uniformly, modifying the stratification of the flow and hence the buoyancy forces. Furthermore, even in the same sunlit configuration (i.e. same orientation, same time of the day), the results can be different depending on the values of the parameters used to describe the material physical properties of the building walls or the ground; for instance, the albedo, which may be increased when painting the surface with a light color. In Figure 7, using the radiative heat transfer model, we present the surface temperatures for three radiative transfer conditions: a 0900 LST sun position with a higher albedo value (0.6 instead of 0.1) for the building

walls (Fig. 7.1), a reference case same as Fig. 7.1 but with an albedo of 0.1 for the building walls (Fig. 7.2), and same as Fig. 7.2 but for a 1600 LST sun position (Fig. 7.3). As in Section 4.1, all analyses are made after 10 minutes of simulation. Increasing the albedo without changing the daytime, since the building surfaces reflect more solar radiation, results in a decrease in wall temperatures (comparison of Fig. 7.1 and Fig. 7.2). In the late afternoon (1600 LST), the sun has almost shifted around to the opposite position, therefore the shaded zones appear in front of the windward side and the heated walls are mostly the leeward sides.

Figure 8 compares the distribution of the potential temperature and the normalized velocity vector maps projected onto the center-plane under the three radiative transfer conditions listed above. In the morning, when increasing the albedo, the sunlit surfaces (windward walls and roofs) are less heated, and consequently the airflow is fairly less heated close to these areas (Fig. 8.1 and Fig. 8.2). To emphasize this further, we have plotted the differences between the case with an increased albedo of the building walls case and the reference one: in vertical velocity (Fig. 9.1) and potential temperature (Fig. 9.2). The ground close to the first windward wall and the last leeward wall is more heated because it receives more reflected solar radiation from the building walls. As a result, the potential temperature is locally increased. Increasing the albedo of the walls not only locally changes the airflow pattern ($-0.05 \sim 0.30 ms^{-1}$) but also the heating pattern: warmer ground and cooler windward walls and roofs.

In the late afternoon (1600 LST), in comparison to 0900 LST, the leeward walls are sunlit and are more heated than windward walls (Fig. 8.3). In comparison to the neutral case (Fig. 5.1), the airflow structure seems to be less disturbed than when the sun shines on the windward side and the potential temperature is

not increased significantly.

4.3. Quantitative analysis

In order to clarify and quantitatively analyze the thermal impact on the airflow, we have plotted several vertical profiles of different variables at different positions in the domain. In Figure 10a-f, we compare the vertical profiles of potential temperature, normalized vertical velocity and TKE, respectively, near the windward side and behind the leeward wall of the last building (from left-hand side to right-hand side) under different thermal models (i.e. neutral, imposed temperatures and different radiative transfer parameters). Taking into account the thermal stratification in the non neutral cases, the airflow shows a large variability (Fig. 10a-f). Close to the windward wall, compared to the neutral condition and except in the radiative transfer case with a 1600 LST sun position, the potential temperature is largely increased near the ground level ($\sim +2.4^{\circ}$C). From $z/H = 0.2$, the potential temperature rises and reaches its maximal value within the range $z/H = 0.8 - 0.9$. After that, the airflow cools down and the profiles tend to the neutral case at about $z/H = 3$. Near the last leeward wall, the potential temperature difference at the ground level between the radiative reference case (green line) and imposed temperatures case (red line) is about 2.5°C (Fig. 10d), which is due to the shading effects behind the last buildings not taken into account in the imposed temperatures case.

When taking into account the thermal stratification, the vertical component of the velocity shows some variability (Fig. 10b and 10e). Without heating, the vertical velocity turns negative forming a downdraft flow in the canyons close to the windward sides or over the canyons close to the leeward sides. On the contrary, with thermal transfer, the vertical velocity is always positive and a strong updraft

flow is formed from $z/H = 0.2$ up to the roof level. The impact of the heating on the TKE (Fig. 10c and 10f) is also important at these low wind speeds. The thermal gradients near the windward wall and near the leeward wall induce a difference in the TKE production.

Close to the windward wall, choosing the imposed surface temperature on the order of magnitude of the ones from the radiative transfer case makes this case agree well with the radiative transfer case on the airflow properties (red and green lines). Significant differences are found close to the leeward side due to different treatments of the ground temperature at this area. These differences lead us to conclude on the importance of the non-uniform surface heating configuration with the 3D radiative model, linked to the full flow simulation.

For the radiative transfer cases, a late afternoon sunlit position (1600 LST) and using a higher albedo value for the walls both result in smaller heating. However, in comparison to the morning (0900 LST) with an albedo of 0.6, the late afternoon sun position with an albedo of 0.1 shows a weaker impact on the airflow (blue and cyan lines in Fig.10a, 10b, 10c). Compared to the neutral case, the increase of the potential temperature is less than 1°C in the cavity (black and blue lines in the Fig. 10a). Moreover, the variability of the vertical velocity and the TKE are also moderate along the windward wall (black and blue lines in the Fig. 10b. 10c). Behind the last building, the heating of the leeward wall has less influence on the airflow pattern than the heating of the windward one.

5. Conclusion

We have investigated the effects of different wall heating conditions on the airflow within an idealized canopy in a low wind speed case, using new atmospheric

radiative and thermal schemes implemented in the 3D CFD code (*Code_Saturne*). Firstly, the results show the importance of the thermal stratification effects in urban areas for low wind speed and the contribution of 3D radiative transfer within the canopy. The thermally induced motion is combined with the mechanically induced motion formed in the canyon, mainly resulting in increased upward motion.

Because of the shading effects, the multi-reflections and the infrared emissions, 3D atmospheric radiative transfer induce a non-uniform and asymmetrical wall heating which, in comparison to the uniform and symmetrical wall heating from imposed surface temperatures conditions, modifies the airflow pattern. In this short-term study (10 minutes with a reference velocity of $1ms^{-1}$), the maximum difference close to the leeward walls reaches $0.3ms^{-1}$ for the vertical velocity and 2 °C for the potential temperature. Secondly, under radiative transfer conditions, we also discussed the influence of the sun position and different values for the albedo of the building. The results show that changing the physical parameters of the walls have an important effect on the potential temperature and motion. We illustrate that increasing the albedo from 0.1 to 0.6 (e.g. painting a dark surface to white) reduces the net radiation flux (Q^*) term in the surface energy balance (SEB), as a result, the potential temperature close to the windward wall or roof may decrease by 2 °C. More examples, using different building materials (e.g. wood, brick) may modify the Q^* term (difference in the infrared emission) and the conductive heat flux (Q_{cond}) term (difference in the conductivity or thickness etc.), therefore has a potentially important influence on the airflow pattern. By describing simulations with the same building physical parameters but different sun positions, we show that solar heating of the leeward wall (at 1600 LST) has less influence on the airflow pattern than the heating of the windward

wall (at 0900 LST) for our particular set-up.

This knowledge is important to further assess the street canyon ventilation potential, the possible shading strategies on building surfaces and the influence of both aspects on indoor thermal comfort and air quality. It can also contribute to future research and applications in the field of wind engineering and pollutant dispersion in the urban environment, when the thermal stratification is of importance.

However, this discussion is based on an idealized urban area. In a real urban environment, the complex geometry has a strong influence on the wind field. Moreover, the simulation results were not compared to any experiment. Using a real measurement data set may be appropriate to qualitatively evaluate the numerical simulations and enrich the discussion. In order to focus on topics related to microscale dispersion in irregular canopy and complex urban environments, our ongoing work is evaluating this model on a district of a real urban area with the CAPITOUL field experiment (City of Toulouse, France).

References

K. Uehara, S. Murakami, S. Oikawa, S. Wakamatsu, Wind tunnel experiments on how thermal stratification affects flow in and above urban street canyons, Atmos. Environ. 34 (2000) 1553–1562.

A. Kovar-Panskus, L. Moulinneuf, E. Savory, A. Abdelqari, J. F. Sini, J. M. Rosant, A. Robins, N. Toy, A wind tunnel investigation of the influence of solar-induced wall-heating on the flow regime within a simulated urban street canyon, Water, Air, & Soil Pollution 2 (2002) 555–571.

K. Richards, M. Schatzmann, B. Leitl, Wind tunnel experiments modelling the thermal effects within the vicinity of a single block building with leeward wall heating, J. Wind Eng. Ind. Aerodyn. 94 (2006) 621–636.

J. F. Sini, S. Anquetin, P. Mestayer, Pollutant Dispersion and Thermal Effects in Urban Street Canyons, Atmos. Environ. 15 (1996) 2659–2677.

J. Kim, J. Baik, Urban street-canyon flows with bottom heating, Atmos. Environ. 35 (2001) 3395–3404.

P. Louka, G. Vachon, J. F. Sini, P. G. Mestayer, J. M. Rosant, Thermal effects on the airflow in a street canyon –Nantes 99 Experimental Results and Model Simulation, Water, Air, and Soil Pollut. 2 (2001) 351–364.

X. Xie, C. H. Liu, D. Y. C. Leung, Impact of building facades and ground heating on wind flow and pollutant transport in street canyons, Atmos. Environ. 41 (2007) 9030–9049.

M. Kanda, Progress in the scale modeling of urban climate: Review, Theor. Appl. Climatol. 84 (2006) 23–33.

K. Niachou, I. Livada, M. Santamouris, Experimental study of temperature and airflow distribution inside an urban canyon during hot summer weather conditions. Part II: Airflow analysis, Build. Environ. 43 (2008) 1393–1403.

M. Milliez, Modélisation micro-météorologique en milieu urbain: dispersion des polluants et prise en compte des effets radiatifs, Ph.D. thesis, École des Ponts ParisTech, [in French, available on line at http://cerea.enpc.fr/fr/theses.html], 2006.

Y. Qu, M. Milliez, L. Musson-Genon, B. Carissimo, Micrometeorological modeling of radiative and convective effects with a building resolving code, J. Appl. Meteor. Climatol. 50 (8) (2011) 1713–1724.

E. Yee, C. A. Biltoft, Concentration fluctuations measurements in a plume dispersing through a regular array of obstacles, Boundary-Layer Meteorol. 111 (2004) 363–415.

M. Milliez, B. Carissimo, Numerical simulations of pollutant dispersion in an idealized urban area, for different meteorological conditions, Bound.-Layer Meteor. 122 (2) (2007) 321–342.

F. Archambeau, N. Méchitoua, M. Sakiz, *Code_Saturne*: a Finite Volume Code for the Computation of Turbulent Incompressible Flows - Industrial Applications, Int J Finite Volumes 1 (2004) 1–62.

W. A. Fiveland, Discrete-ordinates solutions of the radiative transport equation for rectangular enclosure, J. Heat Tran. 106 (1984) 699–706.

J. S. Truelove, Discrete-ordinates solutions of the radiative transport equation, J. Heat Tran. 109 (1987) 1048–1051.

J. Liu, H. M. Shang, Y. S. Chen, Development of an unstructured radiation model applicable for two-dimensional planar, axisymmetric, and three-dimensional geometries, J. Heat Tran. 66 (2000) 17–33.

J. F. Louis, A parametric model of vertical eddy fluxes in the atmosphere, Bound.-Layer Meteor. 17 (1979) 187–202.

T. R. Oke, Boundary Layer Climates, Routledge, 2 edn., 1987.

S. Onomura, H. Takimoto, M. Kanda, Influence of a heated wall on urban canopy flow using PIV measurements, in: 7th Int. Conf. on Urban Climate, Yokohama, Japan (June 29 - July 3), 2009.

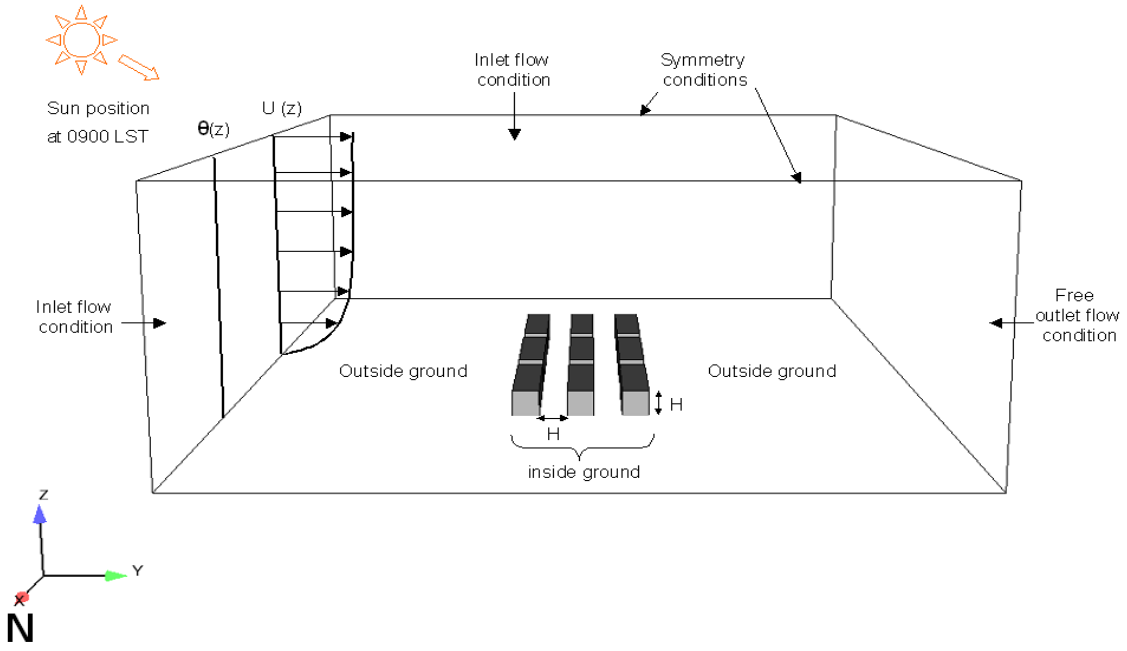

Figure 1: Computational domain with building models for low wind speed simulations-definition of boundary conditions.

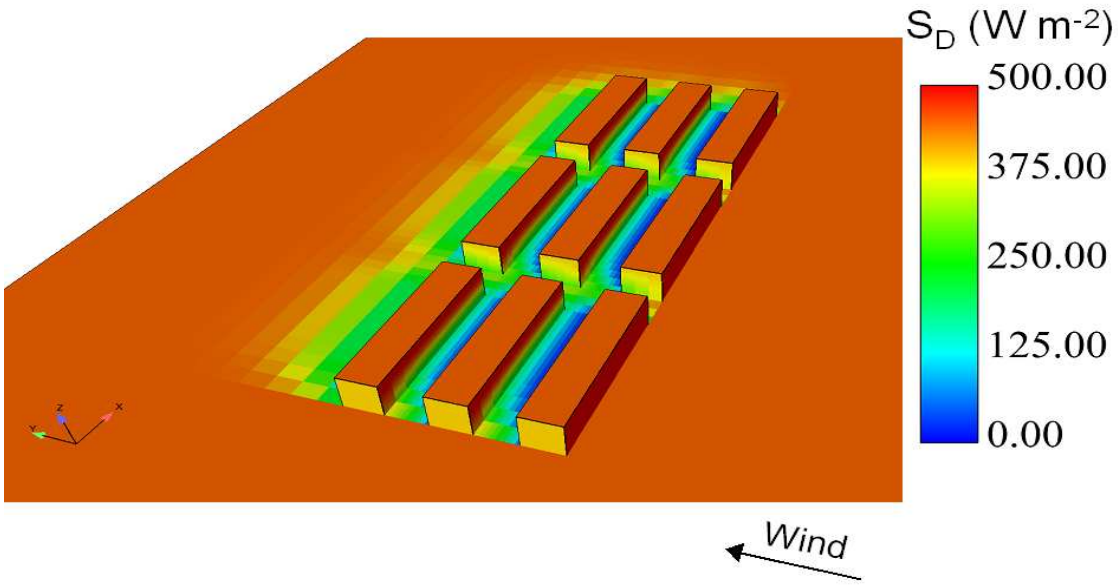

Figure 2: Visualization of the direct solar flux (S_D) ($W\ m^{-2}$) received by the surfaces with a 0900 LST sun position from the radiative model.

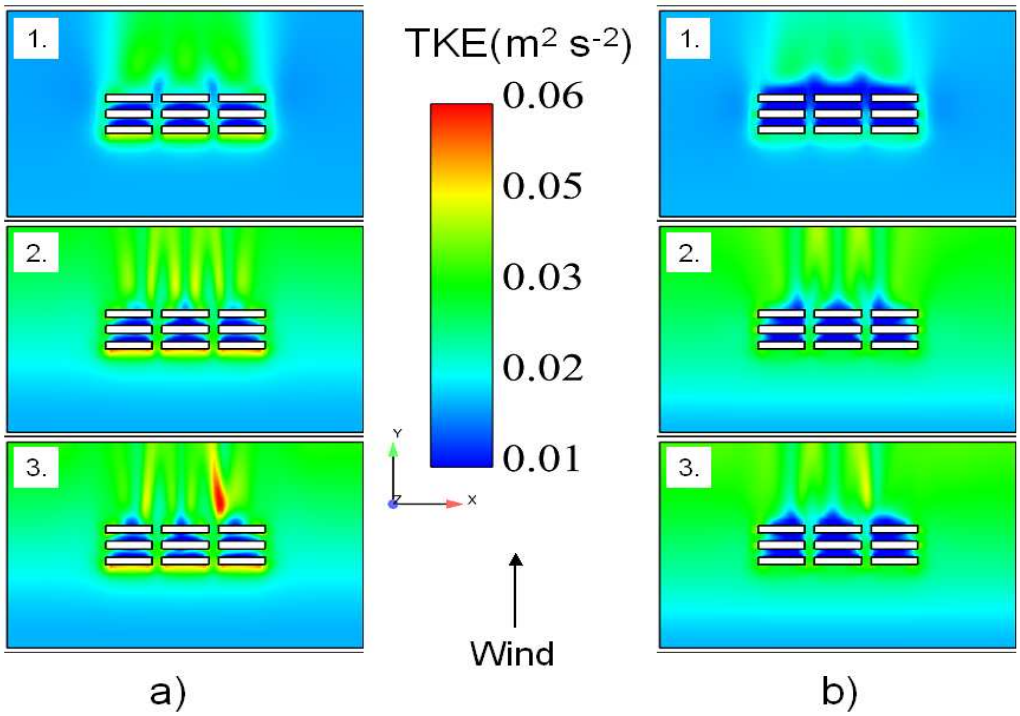

Figure 3: Comparison of the mean turbulent kinetic energy (TKE) (m^2s^{-2}) distribution on: a) roof level; b) half height of the building, for three thermal conditions: 1) neutral; 2) imposed temperatures; 3) 3D radiative transfer with a 0900 LST sun position.

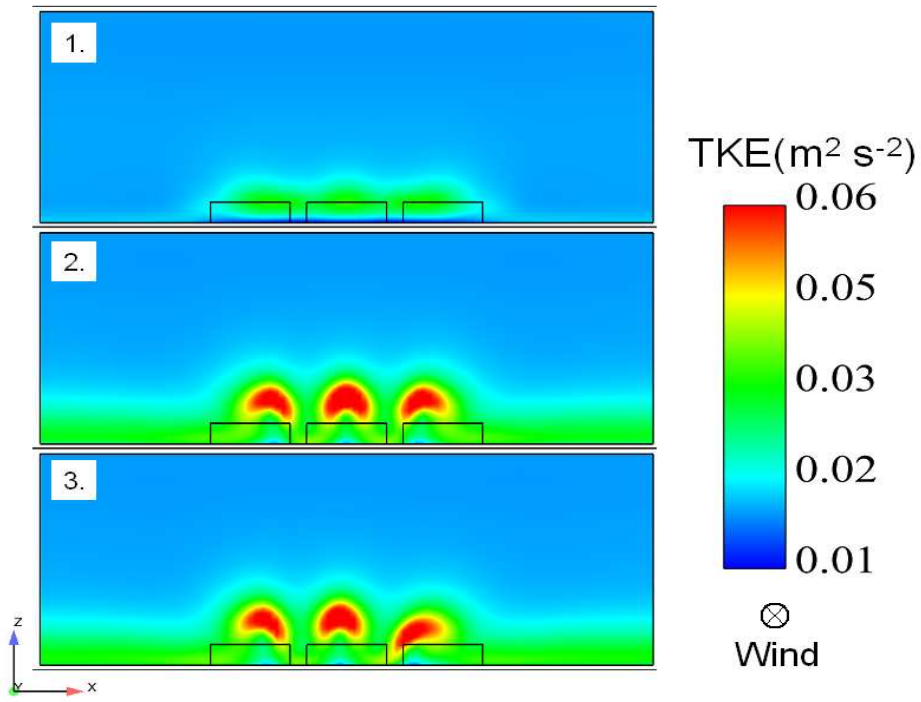

Figure 4: Comparison of the mean turbulent kinetic energy (TKE) (m^2s^{-2}) distribution on the cross-section at 5H behind last building for three thermal conditions: 1) neutral; 2) imposed temperatures; 3) 3D radiative transfer with a 0900 LST sun position.

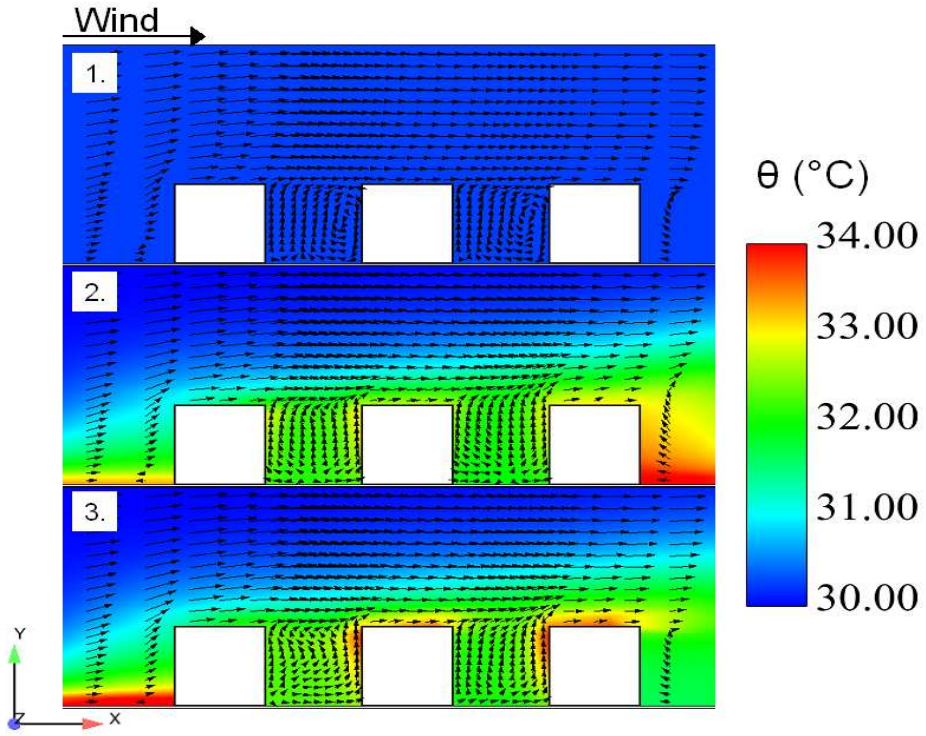

Figure 5: Comparison of the mean airflow potential temperature (θ) (°C) distribution on the center-plane for three thermal conditions: 1) neutral; 2) imposed temperatures; 3) 3D radiative transfer with a 0900 LST sun position.

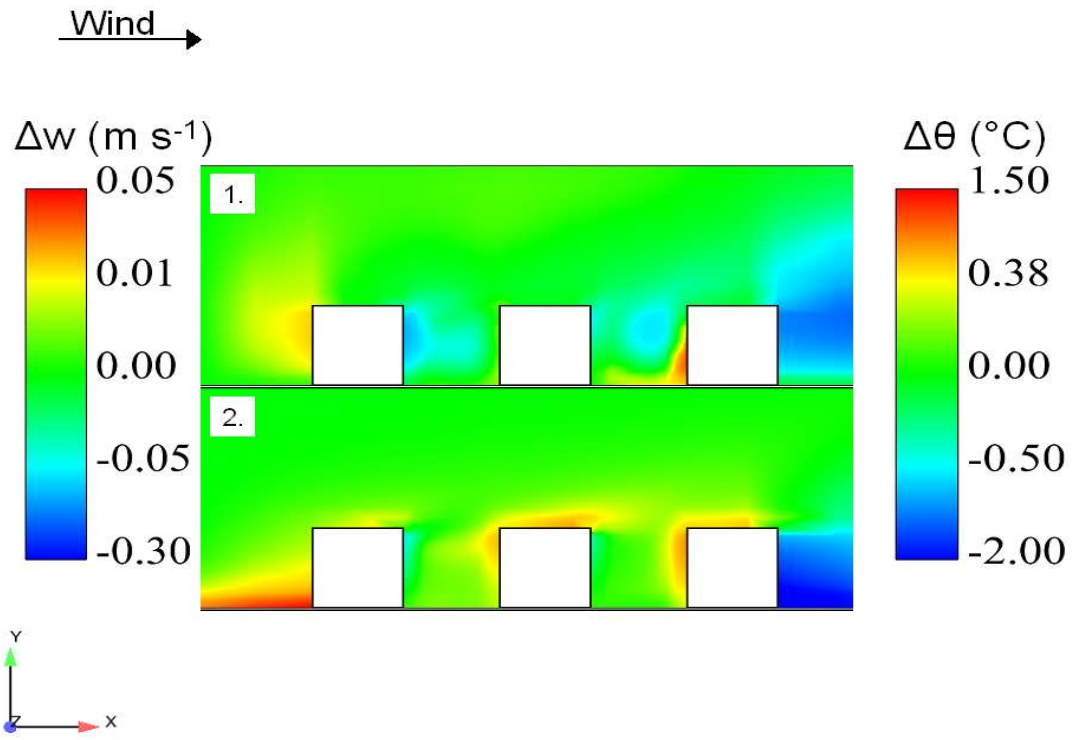

Figure 6: Difference between 3D radiative transfer with a 0900 LST sun position and imposed temperatures case on the center-plane: 1) difference in vertical velocity (Δw) (ms^{-1}); 2) difference in potential temperature ($\Delta\theta$) (°C).

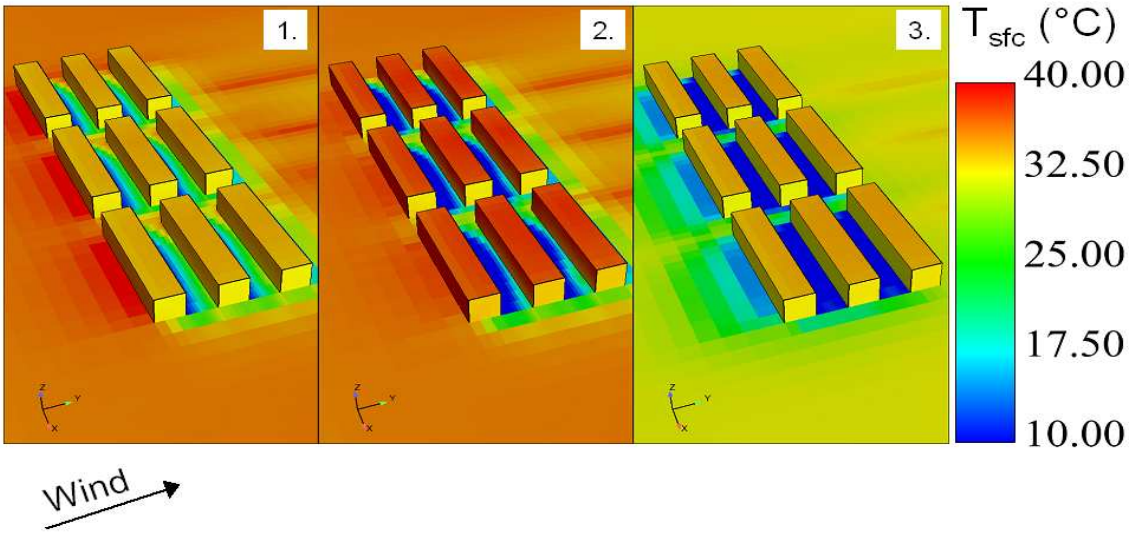

Figure 7: Comparison of the surface temperatures (T_{sfc}) (°C) for three radiative transfer conditions: 1) a 0900 LST sun position with an albedo of 0.6 for the building walls; 2) same as 1) but with an albedo of 0.1 for the building wall; 3) same as 2) but with a 1600 LST sun position.

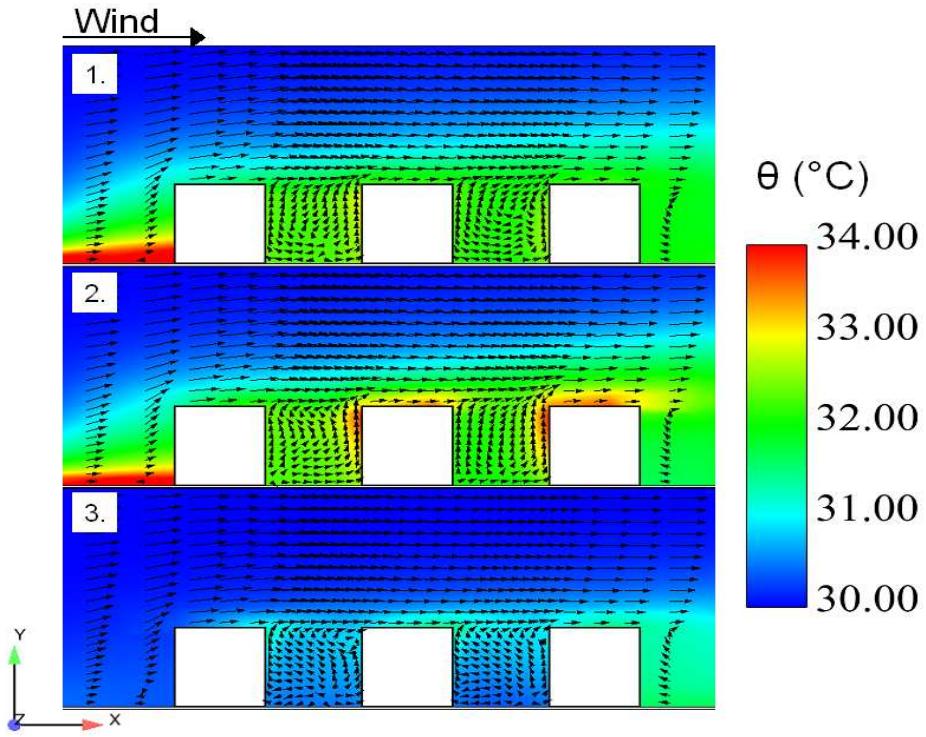

Figure 8: Comparison of the mean airflow potential temperature (θ) (°C) on the center-plane for three radiative transfer conditions: 1) a 0900 LST sun position with an albedo of 0.6 for the building walls; 2) same as 1) but with an albedo of 0.1 for the building walls; 3) same as 2) but with a 1600 LST sun position.

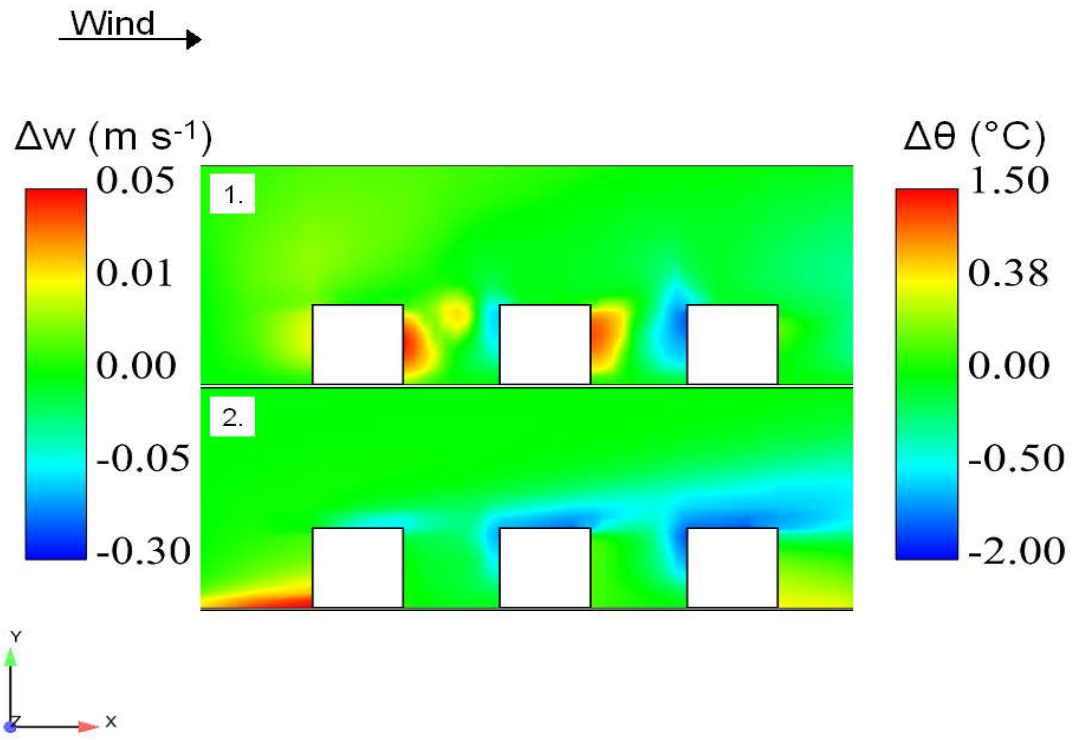

Figure 9: Difference with a 0900 LST sun position between 3D radiative transfer with an albedo of 0.6 and with an albedo of 0.1 for the building walls on the center-plane: 1) difference in vertical velocity (Δw) (ms^{-1}); 2) difference in potential temperature ($\Delta\theta$) (°C).

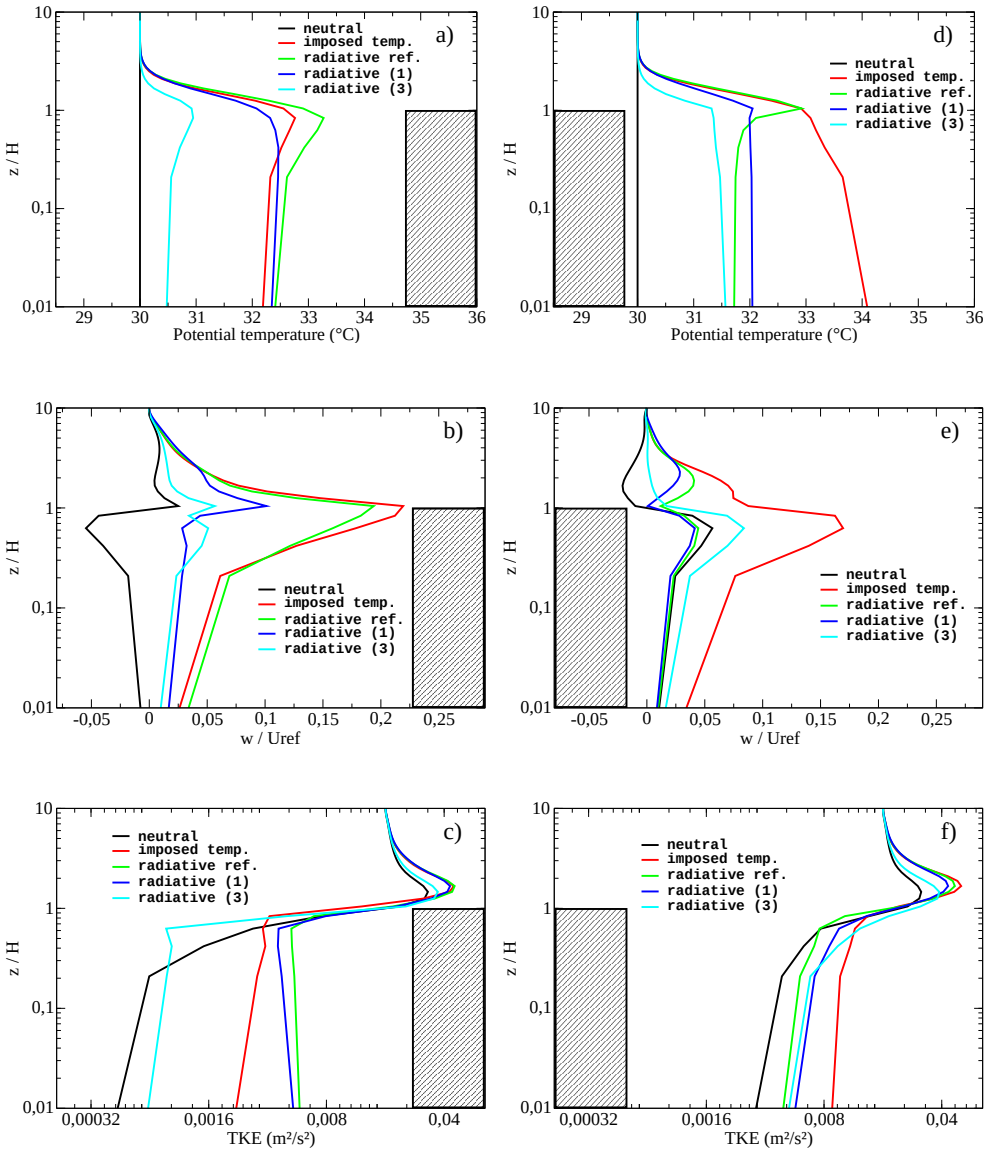

Figure 10: Vertical profiles of (a) potential temperature (θ) (°C); (b) normalized vertical velocity (w/U_{ref}); (c) turbulent kinetic energy (TKE) (m^2s^{-2}) close to the last windward wall (from left-hand side to right-hand side) under different thermal conditions (black: neutral; red: imposed temperatures; green (i.e. radiative ref.): a 0900 LST sun position with an albedo of 0.1 for the building wall; blue (i.e. radiative (1)): same as radiative ref. but with an albedo of 0.6 for the building wall; cyan (i.e. radiative (3)): same as radiative ref. but with a 1600 LST sun position). (d), (e) and (f) same as (a), (b) and (c) but close to the last leeward wall.

Table 1: Parameters used in the low wind speed simulations: Z_{ref} reference height for the inlet profile; U_{ref} inlet initial wind speed at Z_{ref}; ϕ the initial wind angle; z_0 dynamical roughness length; z_{0_T} thermal roughness length; α_S, α_W and α_R respectively albedo of soil, walls and roofs; ε_S, ε_W and ε_R respectively emissivity of soil, walls and roofs; λ_S, λ_W and λ_R respectively conductivity of soil, walls and roofs; e_S, e_W and e_R respectively thickness of soil, walls and roofs; θ initial potential temperature; T_S soil temperature, first: initial value for the radiative transfer case, second: value inside the canopy for imposed temperatures case, third: value outside the canopy for imposed temperatures case; T_{Sint} the deep-soil temperature; T_{Wint} and T_{Rint} respectively building wall and roof internal temperature; T_W and T_R respectively walls and roofs surface temperature: initial value for the radiative transfer case and value for the imposed temperatures case.

Parameter	Unit	Value
Dynamic:		
Time-step	s	0.05
Z_{ref}	m	10
U_{ref}	ms^{-1}	1.0
ϕ	$^\circ$	-90
Soil z_0	cm	4
Wall z_0 = Roof z_0	cm	2
Radiative:		
Time-step	min	2
Soil z_{0_T}	cm	4
Wall z_{0_T} = Roof z_{0_T}	cm	2
α_S		0.53
$\alpha_W = \alpha_R$		0.1
ε_S		0.8
$\varepsilon_W = \varepsilon_R$		0.13
λ_S	$W\ K^{-1}\ m^{-1}$	0.75
$\lambda_W = \lambda_R$	$W\ K^{-1}\ m^{-1}$	6
e_S	cm	50
$e_W = e_R$	cm	10
Initial values:		
θ	$^\circ$C	30
T_S	$^\circ$C	32/11.30/35.15
T_{Sint}	$^\circ$C	25
$T_{Wint} = T_{Rint}$	$^\circ$C	32
$T_W = T_R$	$^\circ$C	36

CHAPTER 6

Validation with CAPITOUL field experiment

Contents

6.1 Introduction

Existing canopy models often use a statistical representation of building which is generally obtained through quantitative field survey or qualitative estimates. But in performing this geo-

metric simplification there is no way to ensure that the simplified geometry match locally the actually city. In this work we want to represent the energy and momentum exchanges in portion of an existing city as realistically as possible.

In the previous work (Milliez, 2006) and also in Chapter 3, 4 and 5, the coupling of the radiative transfer and fluid dynamics models has been evaluated with idealized cases. In order to validate our model as completely as possible with a large available experimental dataset in a real urban environment, we choose the Canopy and Aerosol Particles Interactions in TOulouse Urban Layer (CAPITOUL) experimental dataset. Hereafter, we first give a brief overview of the experimental campaign. Then we present the mesh developed for the city center and the simulation conditions for the selected day of the campaign. Afterwards, we discuss the simulation results with the observation including surface temperatures, brightness temperatures measured by an airborne infrared thermo-graph, sensible heat flux, radiation flux, friction velocity and hand-held thermometers data.

6.2 Overview of CAPITOUL field experiment

The CAPITOUL campaign is a joint experiment, organized by the Centre National de Recherches Meteorologiques and other partners (Laboratoire d'Aérologie, Laboratoire des Mécanismes et Transferts en Géologie and ORAMIP local air quality agency), which took place in Toulouse in southwest of France (43°36'16.21"N, 1°26'38.5"E) from February 2004 to February 2005. It is an effort in urban climate, aiming to document the energetic exchanges between the surface and the atmosphere, the dynamics of the boundary layer over the city, and the interactions between urban boundary layer and aerosol chemistry. A general view of the experiment, describing the goals, experimental set up and a summary of the results is given by Masson et al. (2008).

6.2.1 Objectives and description of the site

The urban area covers approximately 200 km^2 and encompasses $900,000$ inhabitants. The surrounding landscape is relatively flat with small rolling hills. Toulouse was chosen as a candidate for urban climate research for several reasons: its location away from the potential influences of mountains and coastlines, so that it is not influenced by local effects of valley

or sea breezes. The meteorology is therefore mainly controlled by the synoptic flow, so in anticyclonic conditions, urban effects such as the urban heat island, an urban plume or an urban breeze circulation can develop. The old downtown area with an area of approximately 3.5 km^2 is generally made up of buildings 4 to 5 stories high (approximately 20 m) with the walls primarily composed of brick and stone and the roofs of clay tile (Fig. 6.1). This structure is typical of southern European cities but is in contrast to the tall skyscrapers typically found in the urban cores of more modern cities. These characteristics suggest it favors the study of turbulent transport flows for a dense down town area. The city has few polluting industries, the main economic activity being mainly space and aeronautics. The principal sources of air pollutants are the motor vehicle and space heating of buildings. This was an advantage for specific study of carbonaceous aerosols and sulphates (Moscicki, 2007; Pigeon et al., 2008). Study of the energetic exchanges between the surface and the atmosphere was one of the objectives. We briefly describe the data used in this study.

6.2.1.a Meteorological data

The study area is mainly located in the central site of Toulouse around the corner of the two streets, Alsace-Lorraine and Pomme (yellow contour in Fig. 6.1a and Fig. 6.1b). In this neighborhood, vegetation is very scarce and buildings are around 20 m in height (Pigeon et al., 2008). The base of the meteorological mast was on a roof at a height of 20 m, with the top of the mast being 47.5 m above the road (position shown in Fig. 6.4). It provided data including short- and long-wave radiation flux, sensible heat, latent heat, air temperature, wind speed and direction etc. continuously from mid-February 2004 to early March 2005. All meteorological variables were sampled at one-second intervals and were recorded as one minute averages (Masson et al., 2008).

6.2.1.b Infrared surface temperature measurements

A total of ten InfraRed Thermometers (IRTs) were affixed to balconies or booms to record the surface temperatures of the roads, walls, and roofs of the canyons. Described in details in Moscicki (2007), four IRTs were positioned in the Alsace canyon to record surface temperatures of the two walls, the road, and a roof (e.g. Fig. 6.2a). Three IRTs were located in both the Pomme and Remusat canyons to observe the temperature of the two walls and the

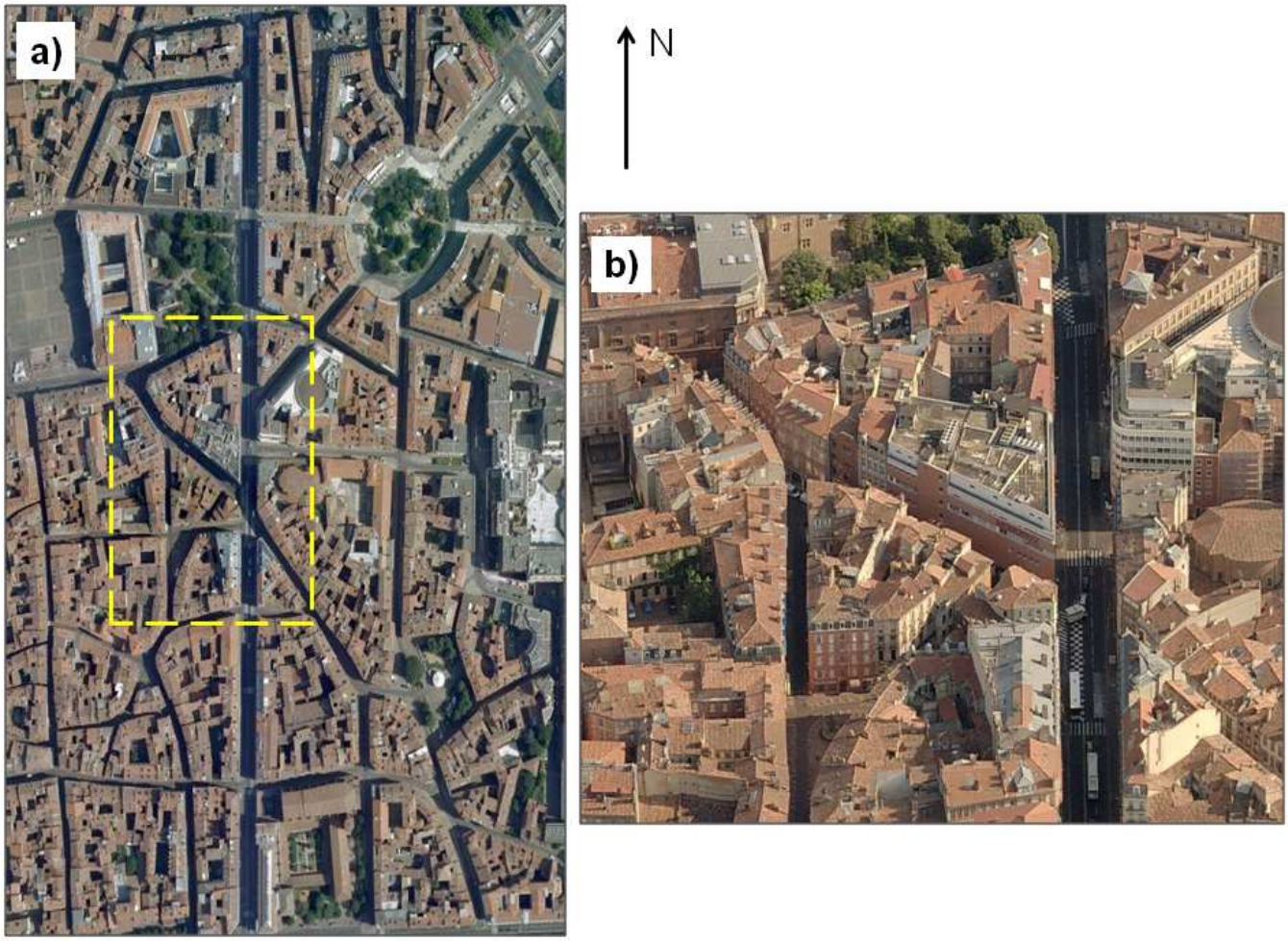

Figure 6.1: Aerial view of downtown Toulouse, France: a) main study area, from Google Maps; b) zoom in the selected area (in a yellow contour), from Bing Maps. The north is indicated.

road in each canyon (e.g. Fig. 6.2b). Temperature observations were sampled at 15-minute intervals and were recorded for the walls and roof at 30-minute intervals at the top and bottom each hour. The canyon floor (road) temperatures were recorded at one-second intervals and this information was then organized into a series of frequency distributions covering 15-minute time spans each with 900 temperature samples and a mean temperature was calculated for each distribution. The road temperature readings were calculated with the correction of the traffic (Moscicki, 2007; Pigeon et al., 2008). The angular Fields Of View (FOV) of each road-viewing IRT is 15° resulting in a FOV encompassing much of the road, centered on the middle of the road. The IRTs viewing opposing walls have a 60° FOV that allowed the viewed area to encompass the majority of the wall. For the roof, an IRT is affixed to a small tower on top of the roof such that the IRT is pointed directly downward. The roof is pitched at a slight angle such that half of it faces southwest and the other half faces northeast. The FOV of the IRT over the roof encompasses portions of the roof facing both directions (Moscicki, 2007).

6.2.1.c Hand-Held IRT data and Aircraft data

A series of observations were recorded using hand-held infrared thermometers for each surface type in the vicinity of the study area on July 15, 2004 (Moscicki, 2007). An example of the database is shown in Fig. 6.3. For the same day, Thermal InfraRed (TIR) airborne images were obtained during several Intensive Observation Periods (IOP) with 2 airborne cameras on board of a Piper Aztec PA23 aircraft over the study area (flight 430: 0749 - 0816 UT; flight 431: 1115 - 1150 UT; flight 432: 1348 - 1423 UT). The speed of the aircraft was 70 $m\,s^{-1}$ and the camera acquisition frequency was 4.3 frames per second. The flight height was about 460 m, which results in a resolution between 1.5 and 3 m depending on the sight angle (Lagouarde et al., 2010; Hénon et al., 2011b).

6.3 Simulation set-up

Concerning urban canopy energetics issue, several papers on the CAPITOUL project have been published. Pigeon et al. (2007, 2008) present the modeling of the anthropogenic heat flux by the TEB urban scheme (Masson, 2000) and its validation against anthropogenic fluxes estimated by a new method using standard surface energy balance measurements. Based on the use of SOLENE model coupled with a 3D model of the city providing the information about the

Figure 6.2: Photo of the affixed IRTs: a) an IRT mounted on a boom in the Alsace canyon; b) IRTs mounted on a railing in the Remusat canyon, one is directed toward the wall across the street and the other to the road below. Source Pigeon (2004).

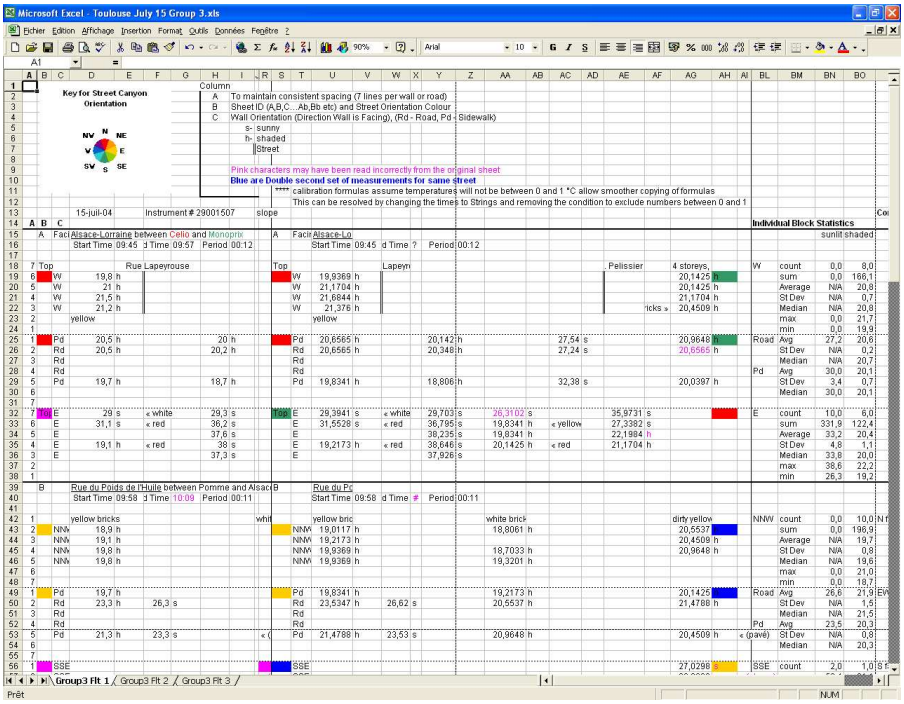

Figure 6.3: An example of the hand-held infrared thermometers database for 15 July 2004.

actual structure of the urban canopy, Lagouarde et al. (2010) simulate the TIR anisotropy and the directional surface temperatures over the Toulouse city. Gastellu-Etchegorry (2008) imports the Toulouse urban databased as a DART scene (Gastellu-Etchegorry et al., 2004) and test the DART-TEB model for simulating remote sensing images and the radiation budget of urban canopies. Recently, using SOLENE software, Hénon et al. (2011b) assessed the case of a small district of the city center for four independent sets of measurements for two complete diurnal cycles, in summer and in winter by comparison with the thermo-radiative simulations.

Whereas most earlier works estimate the sensible heat flux with simplified convection models, the heat transfer coefficient h_f is usually considered as a constant or a simple function of height. In order to model the microscale heat transfer with more accuracy by determining the surface-air thermal gradient that controls convective heat transfer and also examine the mechanisms (e.g. complex topographic influences on air motions), we perform the CAPITOUL simulation with *Code_Saturne* to investigate the thermo-dynamical impacts on the local atmosphere.

6.3.1 Choice of the computational domain

From the CAPITOUL experiment, we selected the day of July 15^{th} 2004. Considering Alsace-Lorraine and Pomme roads as the center of interest in the computational domain (Fig. 6.1), the dimension of the three-dimensional simulation domain is $891 \times 963 \times 200$ m. Using this dimension is taking into account the recommendations of COST 732 (Franke et al., 2007) and AIJ (Tominaga et al., 2008) reports when we introduce the CFD Best practice guidelines in Chapter 2.

6.3.2 Mesh strategy

As we mentioned in Chapter 2, mesh generation may be the most important part of CFD simulation. However with the CAPTOUL complex geometry, it is almost impossible to directly generate a hexahedral mesh. In spite of a larger storage requirement and being less robust than hexahedral mesh, using a tetrahedral mesh in this case is a more feasible option. The information about the 3D structure of the urban canopy was provided by the administrative authorities of Toulouse who made the 3D database of the city available for the CAPITOUL project.

First, we import the urban database (AutoCAD format) of the Toulouse town hall into the commercial mesher ICEM CFD. The urban elements in the database are not individual houses or buildings but a group of the walls and roofs including a large number of internal fine walls which are unnecessary to be meshed. Moreover, the urban elements have a variety of heights but no soil element. So before the meshing step, it is necessary to do a preparatory work on the geometry. After a series of geometric optimization (remove the internal surface, simplify a part of details, create the ground then project the buildings onto it ...), we build a proper geometry topology as shown in Figure 6.4. In real urban environment, all obstacles cannot be resolved with sufficient detail, but their impact need to be parameterized. We describe the strategy for this study as follows. From the boundary of the domain to the center, we progressively retain more geometric details. That is, the buildings at these Alsace-Lorraine and Pomme streets in the center study area are modeled with fine details. Then, the surrounding buildings next to the center study area are simplified as urban blocks. Finally, the buildings in the region outside are treated with a high roughness value at this stage (eventually with drag-porosity in future work). The volumetric mesh used here is an unstructured grid of about $1,8$ million tetrahedral cells. The grid resolution varies from 0.8 m near the center to 24 m far from the center zone (Fig.

6.5).

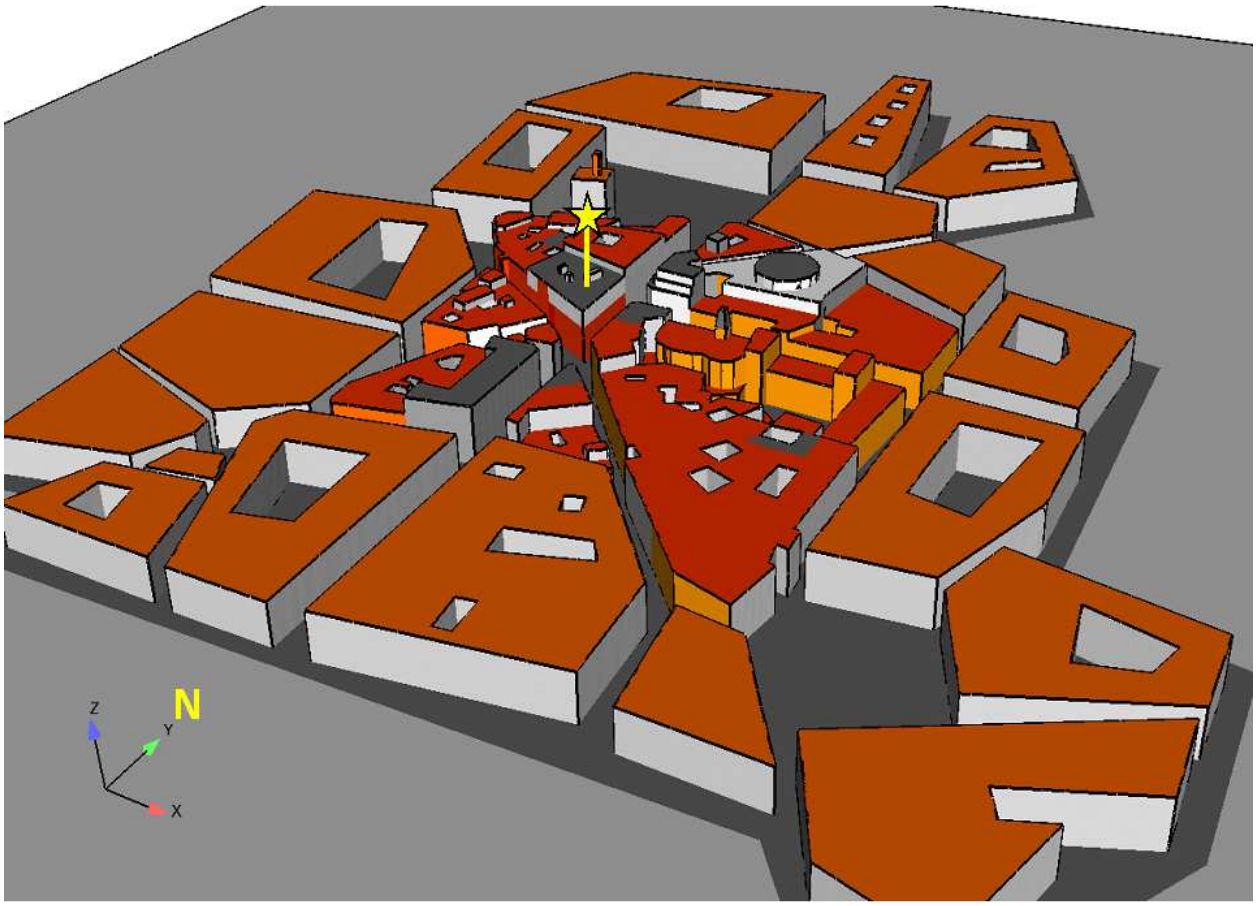

Figure 6.4: Central site area geometry processed by ICEM CFD with the meteorological mast position (yellow star). The north is indicated.

6.3.3 Initial and boundary conditions

The wind inlet boundary conditions are determined from measurements, using a meteorological mast (Fig. 6.4) which gives the wind velocity every 2 hours (Fig. 6.6a), wind direction (Fig. 6.6b), and potential temperature profiles (Fig. 6.6c). In the previous work (see Chapter 3, 4, 5), the surface temperature was obtained by either with a force-restore approach or a wall thermal model. In order to take advantage of the each scheme (force-restore method is well adapted for the soil model, wall thermal model is more appropriate for the building surfaces), in this work, we use the hybrid model, the ground temperature with force-restore method and the building surfaces (wall/roof) temperature with wall thermal model. The variation of the deep

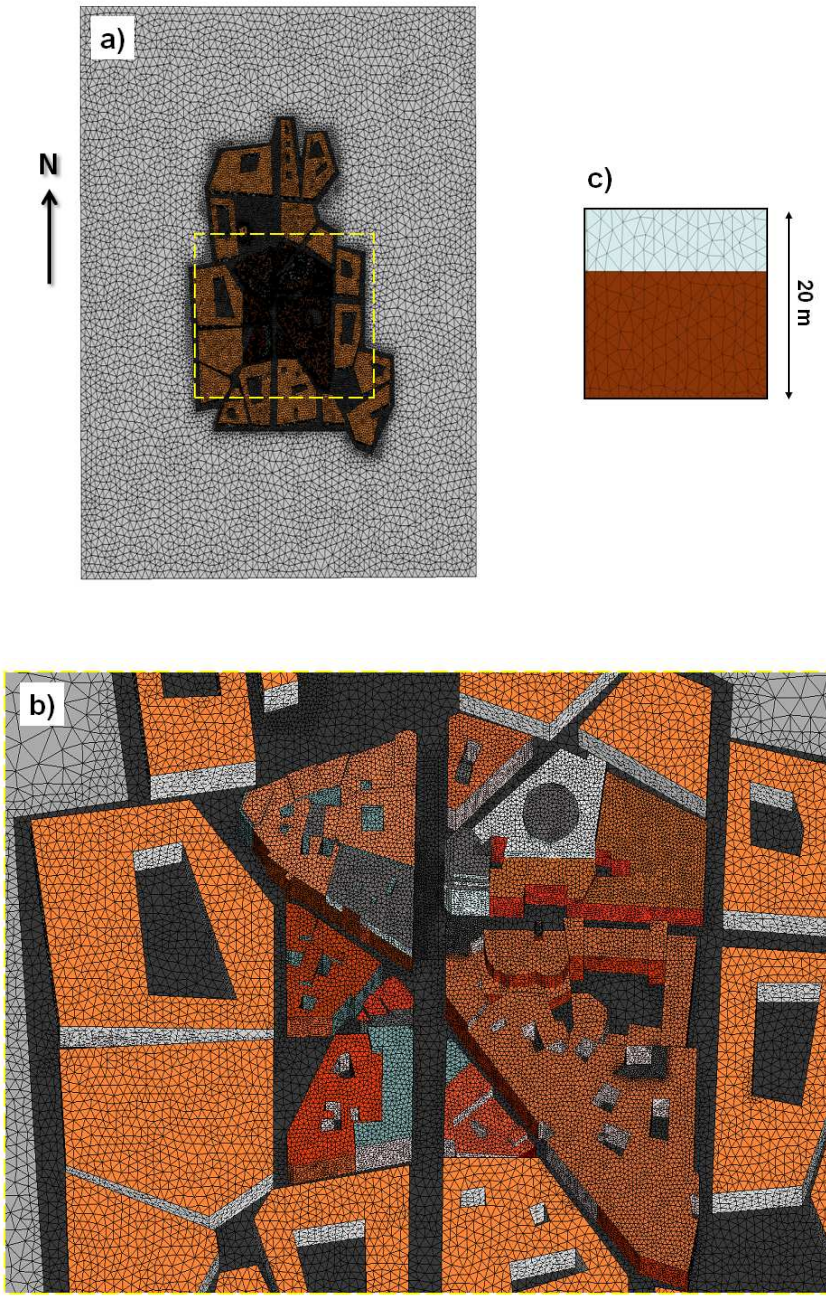

Figure 6.5: Tetrahedral mesh on the central area: a) whole area; b) zoom in the selected area a) (yellow contour); c) zoom in a Monoprix building wall. The north is indicated.

soil temperature is neglected. Since most buildings in the center of Toulouse are from 19th century, walls are built with bricks and most are not insulated as well as the roofs (Pigeon et al., 2008). Thus, at this stage, the internal building temperature is calculated with a temperature evolution equation as Eq. 2.34.

Table 6.1: Parameters applied in the CAPITOUL simulations, symbols with same signification as MUST simulation, see Chapter 3, Table 1.

Parameter	Unit	Value
Dynamic		
Time-step	s	10
Z_{ref}	m	47.5
U_{ref}	ms^{-1}	3.21
ϕ	$^{\circ}$	340
Roof z_0	cm	10
Wall z_0	cm	10
Street z_0	cm	2
Radiative		
Time-step	min	15
Roof z_{0_T}	cm	10
Wall z_{0_T}	cm	10
Street z_{0_T}	cm	2
α_S		0.08
ε_R		0.9
ε_W		0.92
ε_S		0.95
λ_R	$W\ K^{-1}\ m^{-1}$	0.83
λ_W	$W\ K^{-1}\ m^{-1}$	1.15
e_R	m	0.09
e_W	m	0.3
μ_S	$Jm^{-2}s^{-0.5}K^{-1}$	1330
Initial temperature values		
T_{air}	°C	18.86
Alsace East (outside/inside)	°C	22.36/22.94
Alsace Road (outside/inside)	°C	23.18/25
Alsace West (outside/inside)	°C	21.32/22.23
Pomme SSWest(outside/inside)	°C	24.70/25.55
Pomme Route (outside/inside)	°C	23.33/25
Pomme NNEast (outside/inside)	°C	29.06/29.78
LaPoste Roof (outside/inside)	°C	11.13/10.36

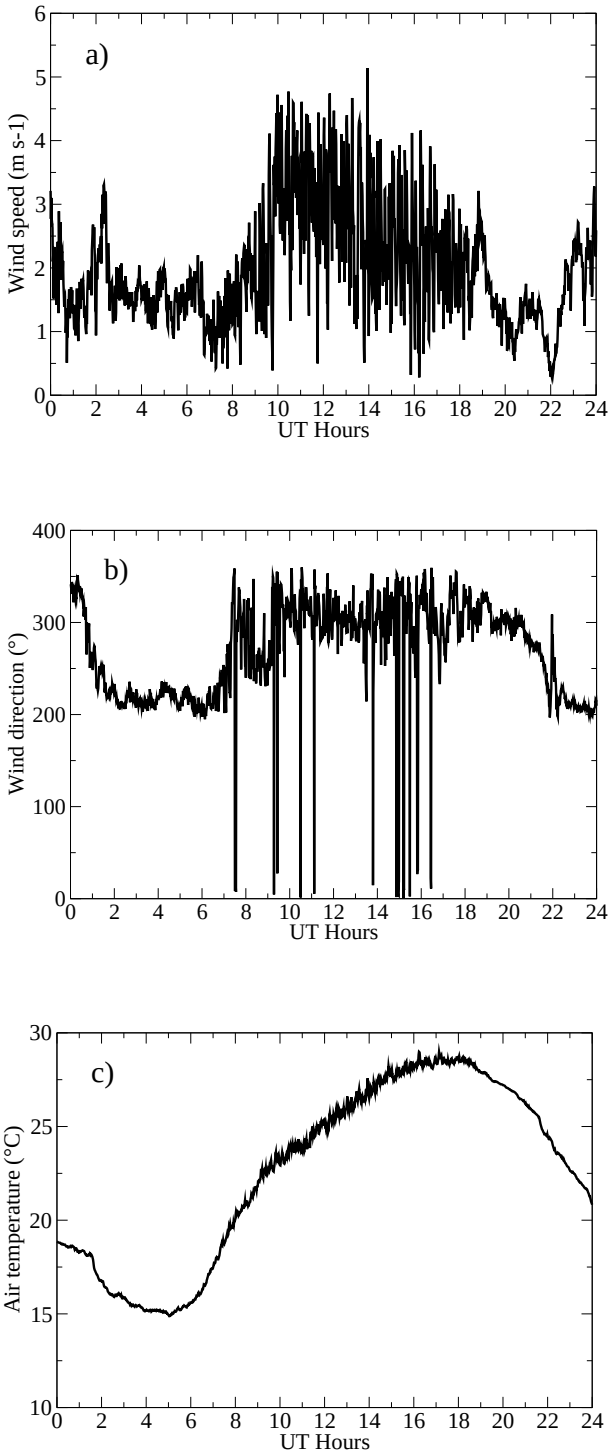

Figure 6.6: Meteorological data at 47.5 *m* above the road from the CAPITOUL experiment for 15 July 2004: a) Wind speed ($m\ s^{-1}$), b) Meteorological wind direction (°), and c) Air temperature (°C).

Table 6.2: Albedo classfication of the buildings surfaces

Paint color	albedo
White	0.6
Whitewash	0.5
Rose	0.3
Gray	0.15

From some Toulouse pictures, we estimate the roughness value depending on its location (e.g. 0.1 m for roofs and walls in the center, 0.02 m for street in the center and 1.5 m for the outside region) and set value for both dynamic roughness length and thermal roughness length. Based on Pigeon et al. (2008), we set the thermal properties such as surface conductivity and thickness. We summarize the model parameters in Table 6.1. Since the values from Pigeon et al. (2008) are averages over the 500-m radius around the surface energy balance station, watching some Toulouse pictures from Google Maps, we furthermore classify four wall painting color (rose, gray, whitewash and white) for the buildings in the center area (Fig. 6.4) to estimate the albedo. Their values are given in Table 6.2.

Modeling the urban energy balance in CAPITOUL consists in several steps. First we test only the radiative scheme without introducing the convective exchange. Second we specify a constant heat transfer coefficient to take into account a global wind field effects. Finally, we model detailed variable wind fields and the effects of the full radiative-convective coupling on the thermal transfer. For the full coupling study, since there is no wind field data available in the street, we retains a degree of simplicity by modeling the h_f under canopy height with 1D h_f model (see Chapter 3, Section 5b).

6.4 Results and discussion

6.4.1 Comparison of IRT pictures

A Thermal InfraRed (IRT) picture from for the aircraft flight 432 of July 15, 2004 at 1412 UT is shown in Figure 6.7a. In Figure 6.7b and 6.7c, we depict respectively the modeled

brightness temperature and surface temperature with the radiative-convective full coupling. We note that it is difficult to compare value by value because of the simplification of the geometry. However, since we distinguish different albedo from painting colors, the model reproduced well the heterogeneity of the distribution of the brightness temperature, especially at roof level (Fig. 6.7b). We can also note that if we were to keep more details especially some slopes on central roof in our 3D model to create a more detailed distribution of the shadows on the roof, the simulated brightness roof temperature would be closer to the observations. The value of the modeled surface temperatures (Fig. 6.7c) is obviously larger than the modeled brightness one (e.g. about 3 °C difference on the roof), because from equation 2.35, we can see that the brightness temperature is approximately proportional to the product of the surface temperature and emissivity ($T_{br} \approx T_{sfc}\varepsilon^{1/4}$, the emissivity is smaller than 1).

Figure 6.8 from (a) to (d) shows the measured and modeled brightness temperatures for the aircraft flight 431 at 1138 UT, compared with three modeling approaches: radiative model only (Fig. 6.8b), radiative and a constant heat transfer coefficient (Fig. 6.8c), and radiative-dynamic full coupling (Fig. 6.8d) using the hybrid thermal scheme for the streets and walls. The constant heat transfer coefficient (Fig. 6.8c) is set similar to Hénon (2008) and Hénon et al. (2011b). The result of the first simulation (Fig. 6.8b, radiative scheme alone) shows that the brightness temperatures are obviously higher than measurements. For a visibility reason, an additional black contour is drawn to show the building structures. Especially on the roof, the difference is more than 25 °C. The modeled T_{br} is out of color range.

Either taking a constant heat transfer coefficient, i.e. assuming a constant wind field in the domain or taking a variable heat transfer coefficient with full coupling i.e. more realistically modeling the wind field, as expected, the results (Fig. 6.8c and 6.8d) show a much better agreement with observation (Fig. 6.8a) in comparison to radiative model only case (Fig. 6.8b). From this IRT picture with this view (Fig. 6.8a), in spite of the fact that we did not keep all the elementary details on the roofs with different orientations and slopes, the simulated temperatures represent well the spatial variability of the temperatures.

For the variable h_f case, the model-observation difference rarely exceeds 10 °C (Fig. 6.8d). We notice also in the measurement (Fig. 6.8a) that for the same roof and same orientation, the temperature may differ by more than 5 °C, for instance at the bottom right of the image. This may be due to heterogeneities in materials and geometry which can not be all accounted for by modeling each individual area (or even every detail). For building walls, either shaded or

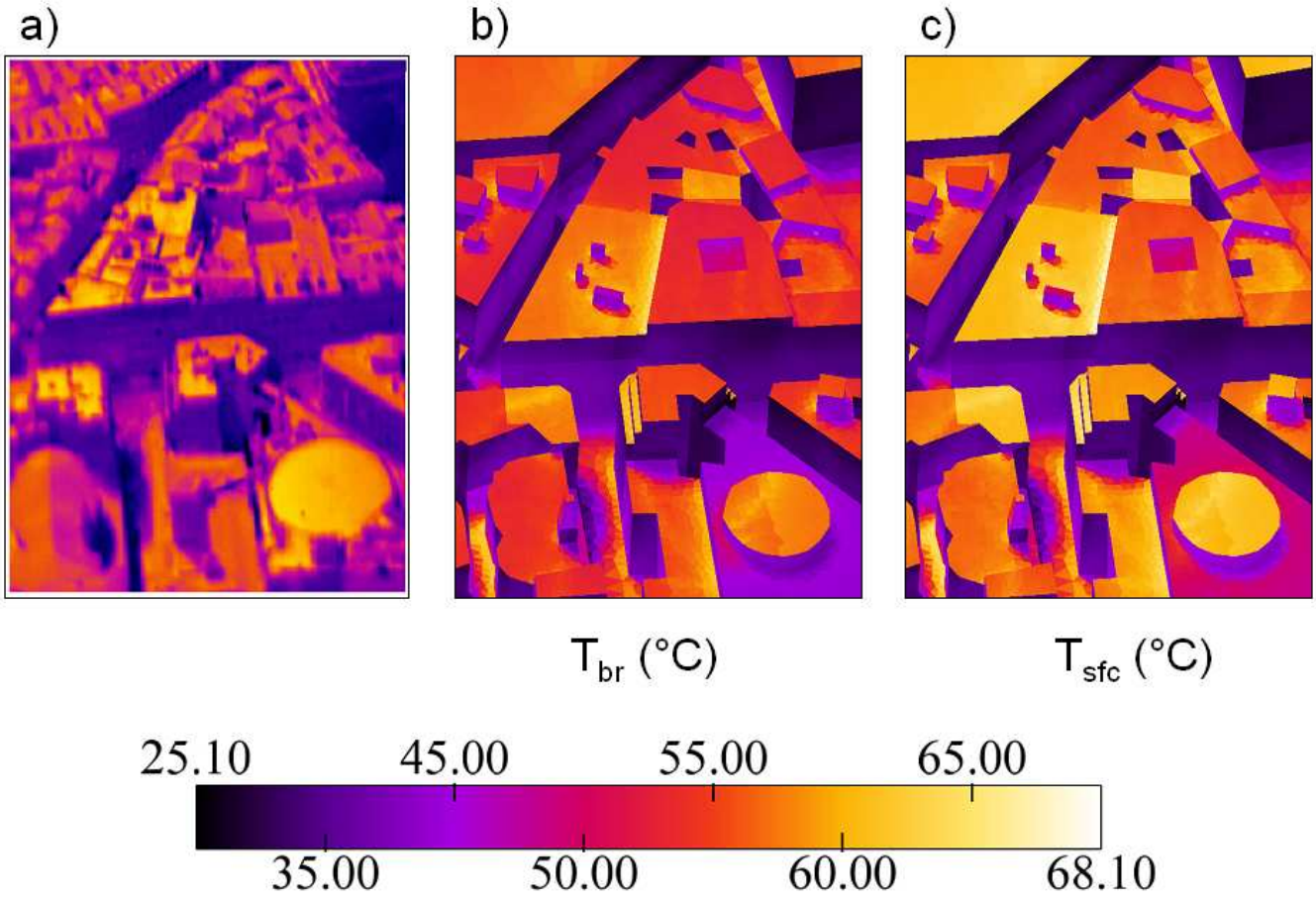

Figure 6.7: Comparison between the Thermal infrared (TIR) airborne images, simulated brightness temperatures and surface temperatures of July 15, 2004, at 1412 UT during flight 432 (Lagouarde et al., 2010): a) TIR picture (189 $\times$ 118 pixels), source from Hénon (2008); b) modeled brightness temperature with full radiative-dynamic coupling; c) same as b) but for modeled surface temperature.

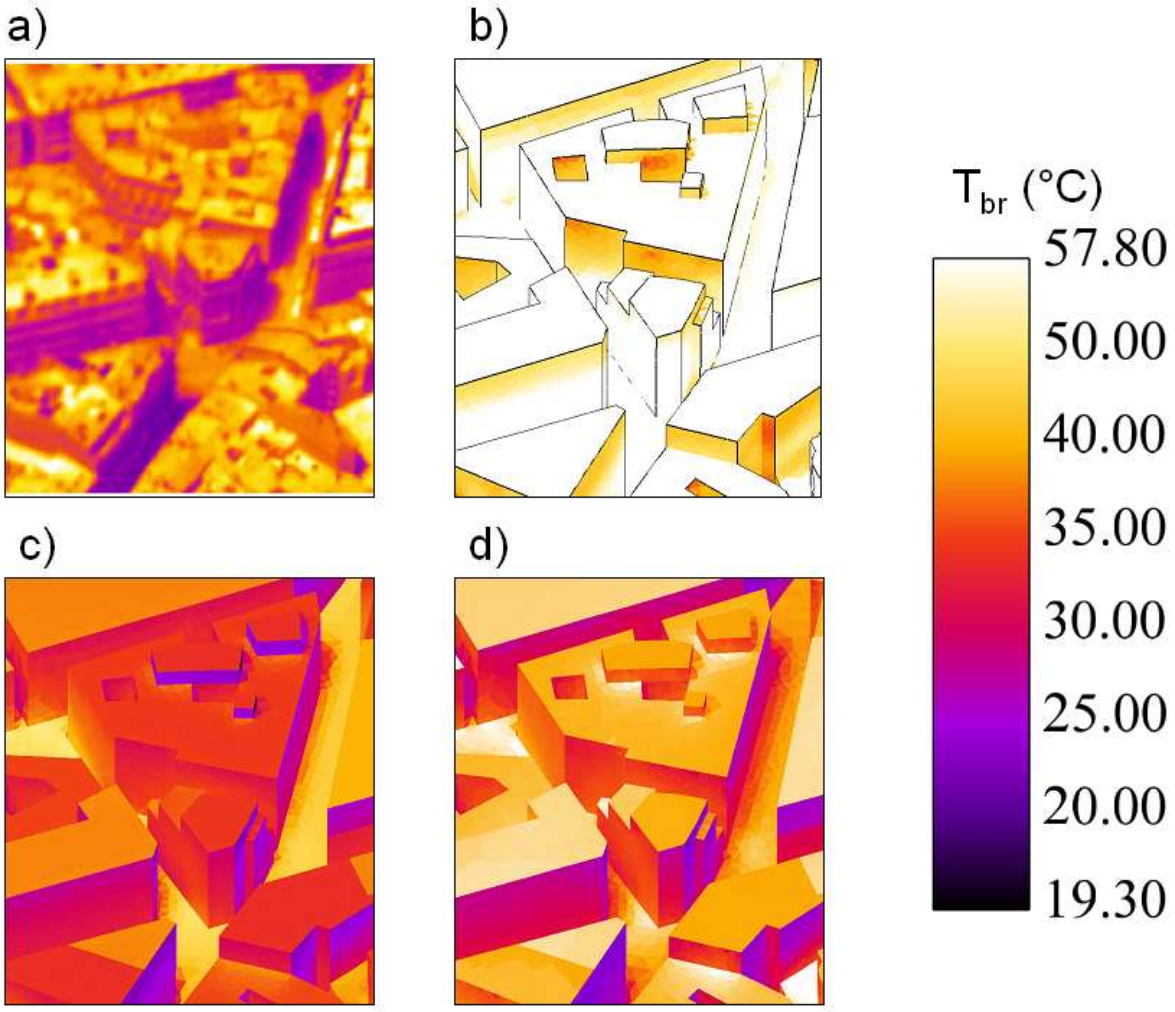

Figure 6.8: Comparison between the simulated brightness temperatures and Thermal infrared (TIR) airborne images of July 15, 2004, at 1138 UT during flight 431 (Lagouarde et al., 2010): a) TIR picture (189 × 118 pixels), source from Hénon (2008); b) Modeled brightness temperature without taking into account the convection; c) Same as b) but with a constant heat transfer coefficient; d) Same as b) but with full radiative-dynamic coupling.

sunlit, the difference between measurement (Fig 6.8a) and simulation (Fig. 6.8d) is generally less than 5°C. In the measurement, some horizontal faces (e.g. buildings at left in center) are relatively warmer than others. This may be due to some external structures (e.g. balcony) that are not modeled but were exposed to the sun and therefore received more solar heating (Hénon, 2008). Regarding the streets, a minimum of 3 cells were set for the width; the model is able to simulate the sharpness of the shadow (Fig. 6.8c and 6.8d). The portion of the street brightness temperatures near the buildings is well reproduced. The averaged difference is less than 3 °C (Fig. 6.8d). The simulated sunny portion is underestimated by about 5 °C (Fig. 6.8d).

The difference between constant h_f (Fig. 6.8c) case and variable h_f case (Fig. 6.8d) is also evident. These two different h_f are shown in Figure 6.9. With the chosen value (Fig. 6.9a), the constant h_f case shows an overcooling about 15°C at roof level, 4 to 5 °C at walls, 4 °C in shaded streets and 7 °C in sunlit streets (Fig. 6.8c). The difference is due to the overestimation of constant chosen value ($h_f = 12$) at this moment. Actually, the contribution of the variable h_f (Fig. 6.9b) may be more important on the surface and air temperature when modeling the temporal evolution. For this reason, we perform the simulation with full coupling for a diurnal evolution in the next section.

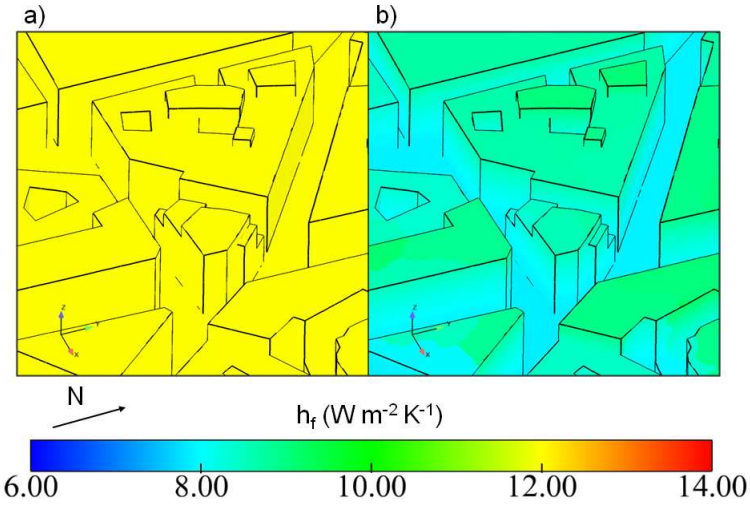

Figure 6.9: Comparison between two convective models with visualization of heat transfer coefficient $h_f(W\ m^{-2}\ K^{-1})$ during same flight as Fig. 6.8: a) constant $h_f = 12$ corresponding to Fig. 6.8c; b) variable h_f corresponding to Fig. 6.8d. The north is indicated.

6.4.2 Comparison of the local diurnal evolution of brightness surface temperature T_{br}

Figure 6.10a to c present the model-observation comparison for the brightness surface temperatures of the diurnal cycle of July 15, 2004. The simulation is performed with full radiative-dynamic coupling. Hereafter, unless specified otherwise, all the results refer to full coupling simulations. The infrared radiometers provided the measured brightness temperatures. Their fixed positions around the central building of the study district are shown in Figure 6.11. Overall, the diurnal evolutions of the brightness surface temperatures at the local positions in the scene are correctly simulated.

For the faces of the Alsace street (black and red lines in Fig. 6.10a), an overcooling about 5 °C appears during the evening (1800 to 2400 UT). Since a similar remark has been found in MUST case (see Chapter 3), it seems that the wall thermal model exhibits an underestimation on the surface temperature after sunset. However, for the Alsace west face, the model predicts a higher brightness temperature (red line in Fig. 6.10a) from 0600 to 1200 UT. By using SOLENE model, Hénon et al. (2011b) also report a similar difference in surface temperature. They explain that this may be due to a sensor underestimation. The ground temperature is computed by the force-restore method which is well adapted for the soil model. The bias on the Alsace road (green line in Fig. 6.10a) can be explained by the approximation of the modeled shadow. Indeed, values taken from the selected cell might be quite different from its neighborhood values.

The brightness temperature of the Pomme route is best predicted (magenta line in Fig. 6.10b). The primary model-observation disagreement occurs on Pomme northeast face (cyan line in Fig. 6.10b) during the afternoon. The bias reaches 8 °C. We can call upon the same explanation as for the Alsace road. Moreover, from some photos (Fig. 6.12), we find that there are numerous windows with white blind on this side of the wall. The infrared radiometer might detect a position where white blinds were closed therefore more solar radiation flux was reflected. Or windows were opened, the ventilation in the canopy led to a lower internal building temperature which decreased the external temperature. Finding a solution is a hard task. Firstly, there is an uncertainty in the observation. Secondly, it needs to model this wall in more details, maybe including the in front walls and windows.

The modeled roof brightness temperature displays a good agreement with observation be-

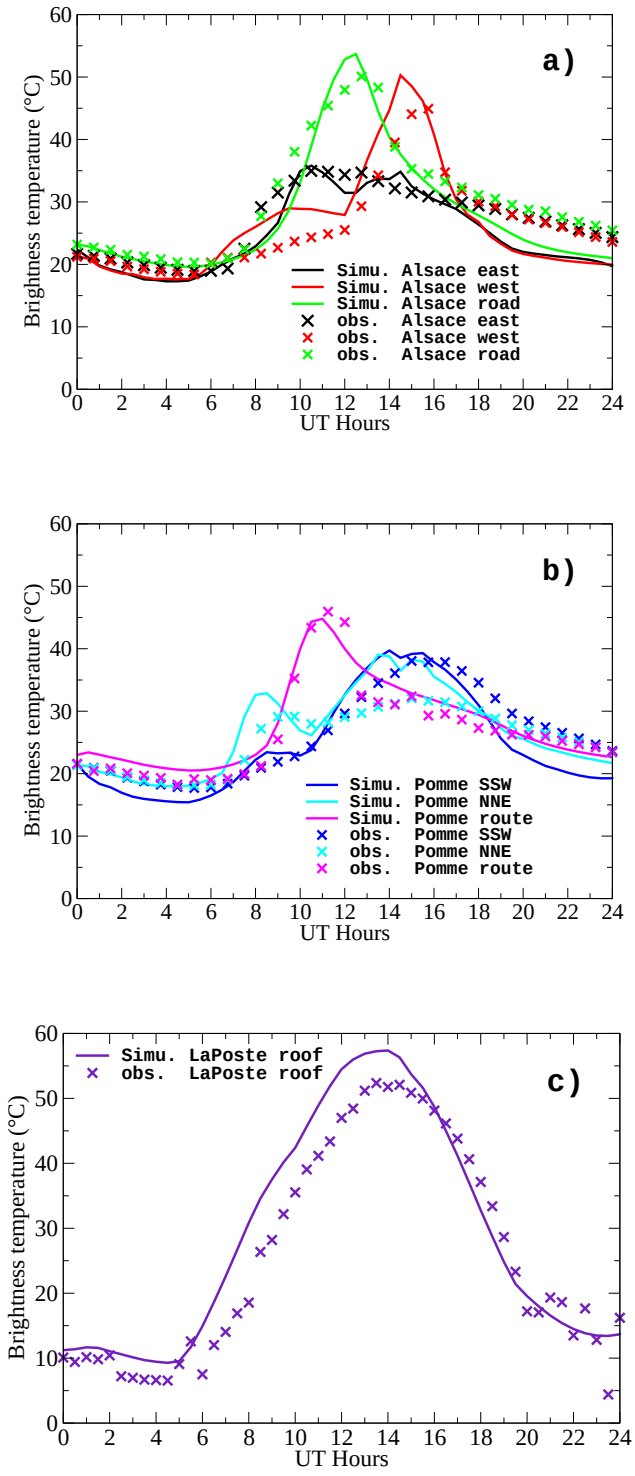

Figure 6.10: Evolution of brightness surface temperature of different positions of the infrared thermometers during a diurnal cycle (cross symbol: Measurements; full line: Simulation).

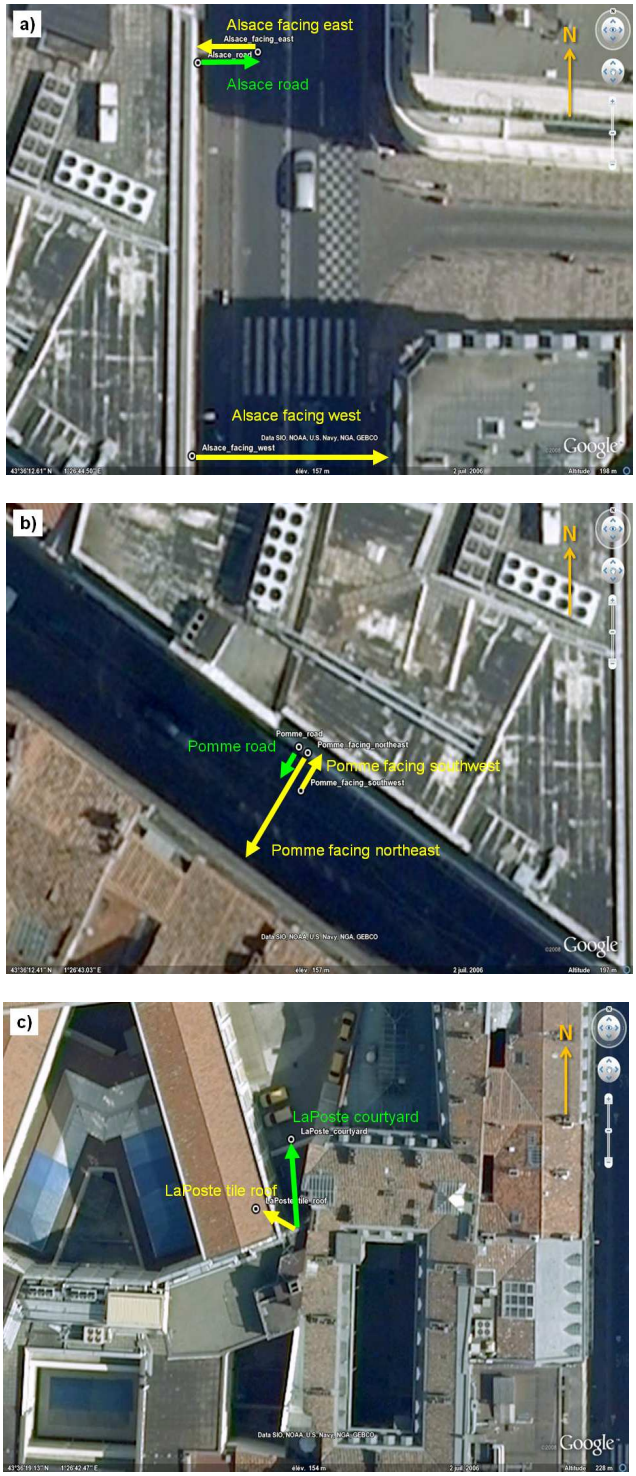

Figure 6.11: From a) to c), different positions of the infrared thermometers. The north is indicated. Source Pigeon (2004).

fore sunrise and from late afternoon to midnight (Fig. 6.10c). However, the model exhibits significant advance in warming when the roof start being sunlit. Actually, the sensor detecting roof brightness temperature was fixed at a northern building's roof from the mast (Fig. 6.11c and Fig. 6.13). This building is treated as a simple block in the 3D model (Fig. 6.4). However, from Figure 6.11c and 6.13, we can observe the complex structure of the roof. In particular, there are some small obstacles which are higher than the measured roof to the east but are not represented in the simulated scene. During the sunrise, the roof might be shaded due to these non modeled detail structures. From the late afternoon, the sun shifts to another side. Since no

Figure 6.12: Photo of the Pomme northeast face, view from affixed IRT sensor. Source Pigeon (2004).

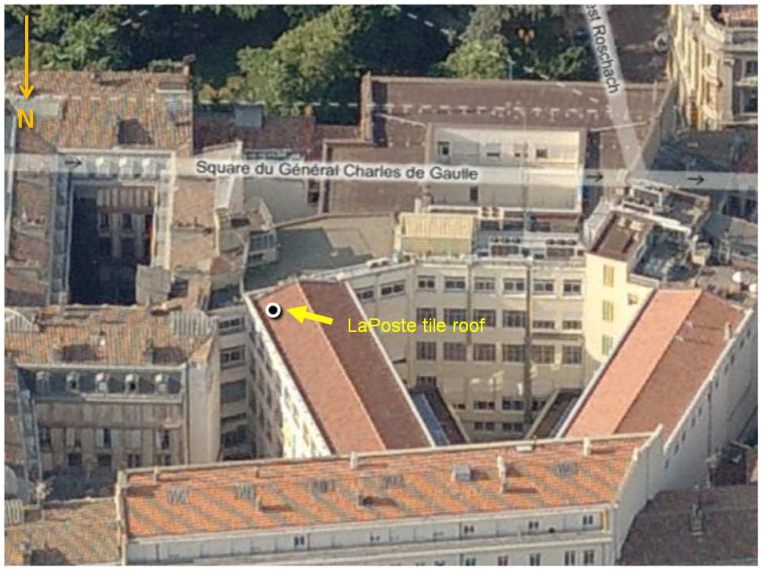

Figure 6.13: Aerial view of IRT position on the LaPoste roof from Bing Maps. The north is indicated.

more small obstacles are higher than the measured roof, the bias disappears.

6.4.3 Model-Observation comparison of heat fluxes

I recall here one advantage of our model is that the determination of the heat fluxes is not only at solid faces but also in the whole fluid domain. In order to compare the fluxes data, we set two monitoring points in the computational domain. One is at the same location as the actual sensors on the top of the mast (47.5 m) (Fig. 6.4). Another is set on the roof surface where the mast is placed (20 m).

6.4.3.a Sensible heat flux Q_H

The sensible heat flux at the surface can be recorded easily in the simulation (cf. Eq. 1.7) and be compared to the value measured on the mast computed using eddy-covariance technique. Here, we assume that the vertical sensible flux is conserved between the surface and its value at sensor level. The horizontal advection of heat is therefore assumed negligible.

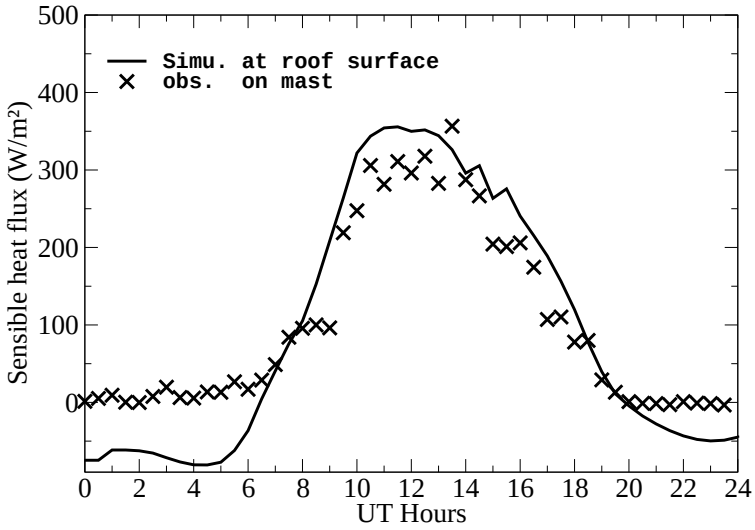

Figure 6.14: Diurnal variation of sensible heat flux calculated at roof surface (full line) and measured on the mast (cross symbol).

Figure 6.14 depicts the comparison between the time evolution of calculated sensible flux at roof surface and the mast observation. Reasonable agreement generally exists between calculated and measured values. Difference between observed and calculated values are less than

40 $W\ m^{-2}$, except for the night ($45-70\ W\ m^{-2}$). From midnight to 0700 UT, the wind is calm but does not have a zero speed (Fig. 6.6a) and the air temperature varies from 15 to 19°C (Fig. 6.6c). The observed sensible flux is very small (cross symbol in Fig. 6.14), this maybe due to the fact that the air layer just above the roof has a temperature very close the roof temperature. However, the initialized roof temperature at this position is set to the same value as the measured roof temperature (11.13°C in Table 6.1). With a non zero heat transfer coefficient and a higher air temperature, consequently, negative sensible heat flux is obtained at roof surface (full line in Fig. 6.14). For the rest of the day the comparison is rather good.

6.4.3.b Outgoing long-wave radiative flux $L^{\uparrow}$

Figure 6.15 shows the model-observation comparison of long-wave radiation flux. The difference between the modeled outgoing long-wave radiation flux at roof surface (full line) and on the mast (dashed line) is generally less than 20 $W\ m^{-2}$. However, both of them give an underestimation of about 20 $W\ m^{-2}$ during the night and a maximum overestimation of about 100 $W\ m^{-2}$ in daytime. In fact, these differences are related to the error of on the roof temperature, i.e. underestimation in the night and overestimation in the day. We recall here, from Eq. 1.6 the outgoing infrared radiation flux highly depends on the surface temperature because of the term of $\varepsilon\sigma T_{sfc}^4$.

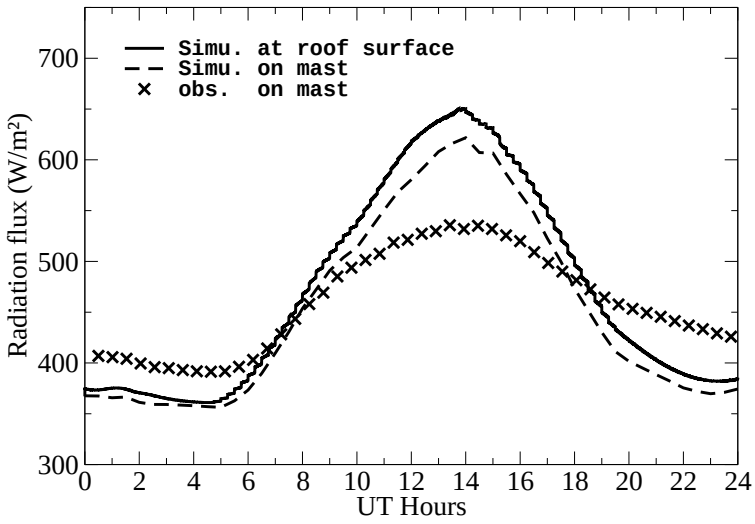

Figure 6.15: Diurnal variation of outgoing infrared flux calculated at roof surface (full line), at the mast level (dashed line) and measured on the mast (cross symbol).

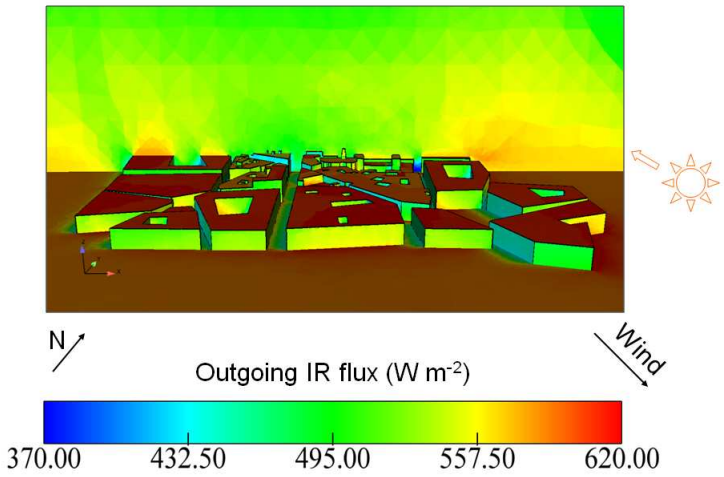

Figure 6.16: Visualization of the outgoing infrared flux on the center-plane and surfaces at 1030 UT. The north, wind and sun direction are indicated.

To complete the discussion, we have the advantage with the model to be able to visualize the radiative flux in the computational domain. Fig. 6.16 illustrates the distribution of the outgoing infrared flux at 1030 UT on the vertical center-plane and on the building surfaces. Significant variability can be observed on the center-plane. Relatively high values are found at horizontal solid-air interface due to the fact that horizontal surfaces are warmer than the vertical surfaces in the daytime.

6.4.3.c Outgoing global radiative flux $S^{\uparrow}$

Figure 6.17 compares the modeled upward global solar flux with the measured one. The non-zero measured nighttime solar flux may be due to the sensor errors or the artificial lights from shop-windows, cars and street-lamps (Hénon et al., 2011b). The upward solar flux can be estimated by Eq. 1.5. For this gray roof (Fig. 6.11b), we set an albedo of 0.15 (Table 6.2). The same value is also proposed by Pigeon et al. (2008) and is used in Hénon et al. (2011b). Compared to the observation, in spite of about 20 $W\ m^{-2}$ higher values at noon estimated by the model (full line), the agreement between measurement and modeled the outgoing solar flux on mast (dashed line) is very satisfactory.

In the same manner as for the long-wave radiative flux, in Figure 6.18 we display the distribution of the outgoing global solar flux at 1030 UT on the center-plane and on the surfaces.

Through the visualization the propagation of the radiative flux in the fluid domain, we can better understand the distribution of the shadow projected by the different structures. We can also readily identify surfaces with higher albedo since they reflect more solar radiation flux.

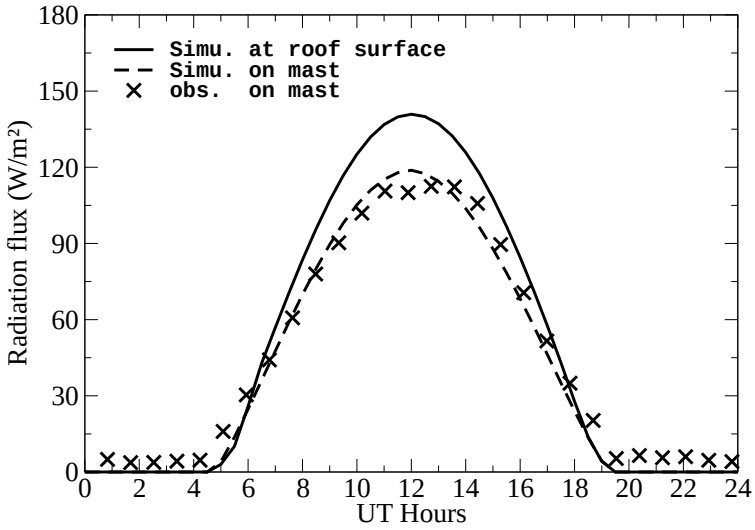

Figure 6.17: Same as Fig. 6.15 but for outgoing solar flux.

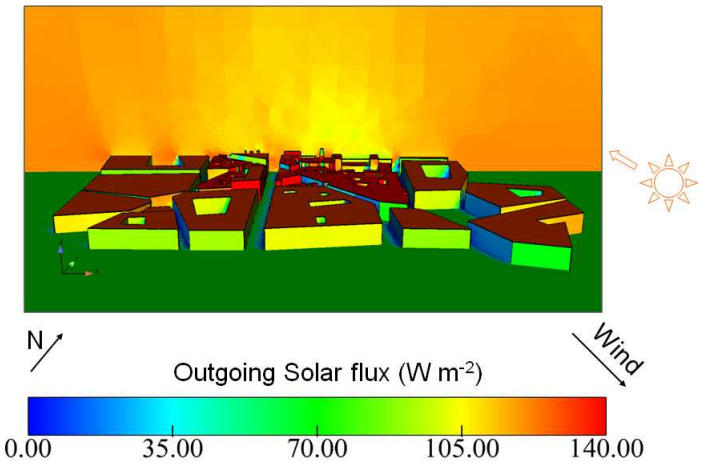

Figure 6.18: Same as Fig. 6.16 but for outgoing solar flux.

6.4.4 Model-Observation comparison of friction velocity u^*

Friction velocity u^* ($m\ s^{-1}$) is also measured on the mast during the CAPITOUL experiment. The u^* at the roof surface is defined by the relation:

$$u^* = (|\tau_w/\rho|)^{1/2}, \tag{6.1}$$

where τ_w is the Reynolds stress at wall ($N\ m^{-2}$), ρ ($kg\ m^{-3}$) the fluid density at the wall.

In order to compare with the observation on the mast, we use the kinematic momentum fluxes in the x and y directions ($\overline{u'w'}$, $\overline{v'w'}$), therefore the friction velocity can be evaluated as:

$$u^* = (\overline{u'w'}^2 + \overline{v'w'}^2)^{1/4}, \tag{6.2}$$

where $\overline{u'w'}$ and $\overline{v'w'}$ are given by:

$$\overline{u'w'} = \nu_t \frac{\partial \bar{u}}{\partial z},\ \overline{v'w'} = \nu_t \frac{\partial \bar{v}}{\partial z}, \tag{6.3}$$

and ν_t ($m^2\ s^{-1}$) is the turbulent viscosity given by the $k-\varepsilon$ closure.

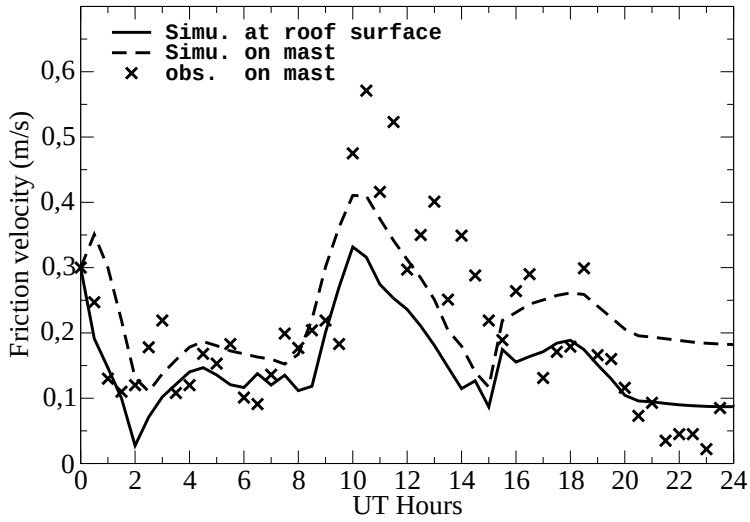

Figure 6.19: Same as Fig. 6.15 but for friction velocity.

From Figure 6.19 it can be seen that the simulated friction velocities are reasonable in terms of magnitude. Modeled friction velocity at roof surface (full line) shows a good agreement with observation when the u^* less than $0.2\ m\ s^{-1}$. Simulated u^* on mast (dashed line) can produce higher value ($0.4\ m\ s^{-1}$). It seems that the model overestimates the nighttime ($1800-2400$

UT) u^* on mast. However, estimates of u^* from the turbulence measurements by the sonic are known to be rather uncertain, especially when u^* is small. The difference between the modeled u^* at roof surface (full line) and at the mast level (dashed line) is due to different methods of the estimation, and the numerical errors in the computed gradients.

6.4.5 Statistical comparison with hand-held IRT data

Regarding hand-held IRT measurement, several groups of records for different surface types in the study center are available in the database (e.g. Fig. 6.3). In order to statistically analyze simulation results with these data, we select the samples obtained in the Alsace street (Fig. 6.20a) at 0945 UT, 1245 UT and 1545 UT for the day of 15th July 2004 and calculate the averaged values, standard deviation and median values for the predicted brightness temperature in a similar zone from the computational domain as shown in Figure 6.20b. The results are tabulated in Tables 6.3, 6.4 and 6.5.

Note that the number of observations that are available to conduct the statistical analysis is often very small. Only records for building walls and street (excluding the roof elements) are available for this database. The data of the street consists of two parts, road and sidewalk. However, we have only a flat ground in our 3D model. For that reason, from our simulation result, we consider that the cells next to the buildings foot belong to the sidewalk part and the central part of the street is the road. Moreover, values in the database were separated into sunlit and shaded part. In order to give a criteria to separate facets in the simulation, we look at the direct solar flux value received by the surfaces. That is, for a given facet, if the direct flux is less than 50 $W\ m^{-2}$ (we discuss the sensitivity to that value later in the text), we consider that it is in the shadow. Otherwise, it is sunny. In addition, if a value is not available in the measurement or does not meet the criteria in the simulation, we set 'N/A' in the tables.

From Table 6.3, we observe that all the westward walls are shaded at 0945 UT. The model gives higher average and median values (about 4 to 7 °C). The results from the facets exposed under the sun conform better with expectation, especially for the sidewalk and eastward walls. The difference between prediction and observation is about 2 to 4 °C for the mean temperature. The pavement prediction shows a better agreement with observation for mean and median temperature but with a relatively important standard deviation (6.2 in Tab. 6.3).

The overall result conveyed by Table 6.4 is disappointing. Most of westward walls from

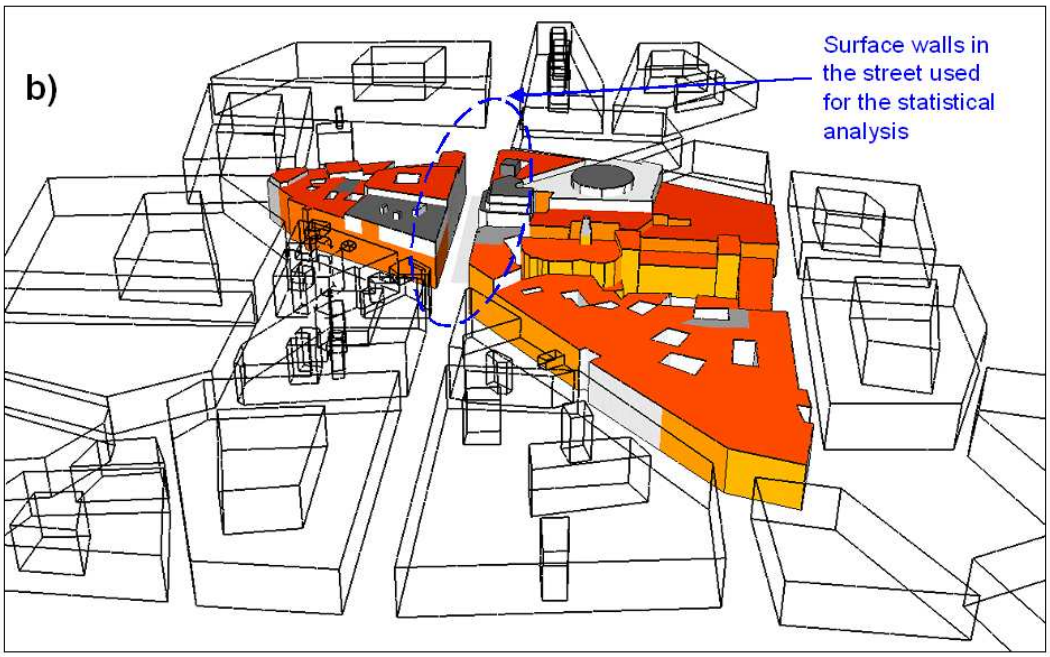

Figure 6.20: Selected zone for statistical study: a) Alsace street view, from Google maps; b) selected urban blocks in 3D model (in color).

0945 UT		Sunlit		Shaded	
		Simulated	Measured	Simulated	Measured
W	Average	N/A	N/A	27.3	20.8
	St. Dev.	N/A	N/A	1.3	0.7
	Median	N/A	N/A	27.5	20.8
	Max	N/A	N/A	29.6	21.7
	Min	N/A	N/A	23.7	19.9
Road	Average	33.5	27.2	27.0	20.6
	St. Dev.	5.7	N/A	0.8	0.2
	Median	32.2	N/A	27.1	20.7
Pd	Average	32.6	30.0	26.9	20.1
	St. Dev.	6.2	3.4	0.8	0.7
	Median	30.0	30.0	27.0	20.1
E	Average	37.5	33.2	25.1	20.4
	St. Dev.	3.5	4.8	1.7	1.1
	Median	36.9	33.8	24.4	20.0
	Max	47.3	38.6	27.9	22.2
	Min	28.4	26.3	22.5	19.2

Table 6.3: Statistical comparison of modeled brightness temperature (°C) and hand-held IRT data (°C) at 0945 UT with: *Sunlit*, *Shaded* values from sunny and shaded conditions, respectively; *Simulated*, *Measured* modeled and observed values, respectively; *St. Dev.* stand deviation; N/A no available value; W, E wall facing west and east respectively; *Road* middle of street; *Pd* sidewalk.

1245 UT		Sunlit		Shaded	
		Simulated	Measured	Simulated	Measured
W	Average	34.2	N/A	28.7	24.4
	St. Dev.	2.4	N/A	0.0	0.7
	Median	34.3	N/A	28.7	24.3
	Max	54.1	N/A	28.7	25.8
	Min	28.1	N/A	28.7	23.7
Road	Average	52.9	37.2	51.8	23.0
	St. Dev.	1.7	7.9	2.7	0.3
	Median	52.6	34.2	52.0	23.0
Pd	Average	50.9	40.0	49.2	22.6
	St. Dev.	5.1	0.6	1.4	0.2
	Median	50.9	40.0	50.3	22.7
E	Average	43.7	34.4	32.2	26.4
	St. Dev.	5.0	1.6	3.1	2.3
	Median	45.8	35.0	32.1	26.4
	Max	49.9	36.4	40.3	28.1
	Min	35.7	30.9	27.7	24.8

Table 6.4: Same as Tab. 6.3 but for 1245 UT.

1545 UT		Sunlit		Shaded	
		Simulated	Measured	Simulated	Measured
W	Average	40.8	32.8	29.9	N/A
	St. Dev.	6.2	2.5	0.8	N/A
	Median	40.8	32.5	29.9	N/A
	Max	55.1	37.3	33.5	N/A
	Min	29.2	28.8	28.1	N/A
Road	Average	N/A	45.8	35.9	36.2
	St. Dev.	N/A	4.8	1.7	1.6
	Median	N/A	48.0	35.6	36.2
Pd	Average	50.5	46.4	35.9	22.6
	St. Dev.	3.5	0.7	3.3	5.9
	Median	50.4	46.4	34.4	33.5
E	Average	41.8	N/A	31.3	30.2
	St. Dev.	3.8	N/A	2.1	0.9
	Median	40.0	N/A	30.8	30.2
	Max	47.4	N/A	37.7	31.5
	Min	37.5	N/A	28.1	28.9

Table 6.5: Same as Tab. 6.3 but for 1545 UT.

the model are judged to be sunlit. Significantly higher values are found for road and pavement (more than 10 °C) than measurements. It seems that the model fails to predict the low temperature of either the shaded road or sidewalk. We notice that either for road or sidewalk, the predicted average and median temperature in shadow is very close to the sunlit one. However, as mentioned above, the threshold set is only 50 $W\ m^{-2}$ from predicted direct solar flux value. It means that the high temperatures from shaded road and sidewalk are not due to heating by the direct solar radiation but probably due to received diffuse solar or infrared radiation and also the multi-reflected radiation by surrounding buildings. Since we can see many shop windows in this commercial street in Figure 6.20a, the model may overestimate the multi-reflection without modeling the glass (Fig. 6.20b). Moreover, the presence of smaller obstacles (e.g. vehicles, traffic signs, fences, etc.) increase the percent cover of shaded surface. A large standard deviation in the observation for the sunlit road (7.9 from Tab. 6.4) shows that the street may have heterogeneities on the surface (e.g. albedo) and materials (e.g. asphalt, concrete, stone). The model gives such result without including these details.

The corresponding results for 1545 UT (Tab. 6.5) are better than for 1245 UT. The shaded elements have the best performance. Bias of the predicted average and median temperatures are only about 1 °C. The modeled sunlit elements have less accuracy. The overestimations of average and median temperature on the westward walls (about 8 °C) are due to some extremely high predicted values. No available values appear for the predicted sunlit road part but not for the pavement. We can explain that the chosen resolution of the road may be insufficient. It leads to the fact that the cells over the threshold appear as pavement.

For this statistical assessment, we have also tested 100 $W\ m^{-2}$ as threshold criteria, but the model result seems not very sensible to this criteria. For instance, averaged temperatures of the sunlit and shaded westward wall at 1545 UT are 41.7 and 30.2 °C respectively against 40.8 and 32.8 °C as found in Table 6.5.

6.5 Conclusions and perspectives

We have investigated the energy exchanges in a real city with the atmosphere during the CAPITOUL campaign, using new atmospheric radiative and thermal schemes implemented in *Code_Saturne*. A pre-processing is realized including the optimization of the complex geometry and creation of a high quality tetrahedral mesh for this study. It also requires determining the

complex thermal parameters which take into account the actual variability of materials in the district. Based on the literature data, we have separated the building surface into 4 categories of albedo depending on painting colors.

First, simulations are evaluated with the comparison with Thermal InfraRed airborne images from two flights in the day of 15th July 2004 during the CAPITOUL project. The result shows the importance of taking into account heterogeneities in materials and geometry to represent the spatial variability of the temperatures in complex urban areas. Then, we have evaluated the coupled dynamic-radiative model with CAPITOUL experiment including the comparison with the measured brightness temperature, sensible flux, radiative fluxes diurnal variation, and statistical values with hand-held IRT data. Overall the agreement between measurements and model simulations are fair but can be improved in the future with more information. For the sensible flux, the model-observation nighttime bias is probably linked to the uncertainty of the estimation on the roof nighttime temperature. Similar explanation can be used for the comparison of the outgoing infrared flux, because results are sensitive to the surface temperature. In fact, due to the complex geometries, a comparison of the IR flux in a simple case might be appropriate for understanding the difference and evaluating the model.

Better agreement is obtained for the comparison of the outgoing solar flux at the mast level. However, the difference between the modeled outgoing solar flux at roof surface and at the mast is still unclear. For the modeled friction velocities, the difficulty mainly appears to capture the extreme values (highest or lowest). Small structures may have important influence on the computation of local brightness surface temperature, sensible flux, outgoing short- and long-wave radiation. The simulation results shows the importance of modeling in details while doing local model-observation comparison. The statistical analysis, while comprehensive, is not exhaustive. Despite the fact that difference between measured and modeled averaged, median and standard deviation of brightness surface temperature may be significant, such comparison is very useful for a better understanding of the radiative transfer processes in the canopy.

The model results are encouraging and give insight into local surface-atmosphere processes, but further and more rigorous testing has to be performed, especially regarding vertical sensible flux and upward infrared flux.

CHAPTER 7

Conclusions and Future Work

Contents

7.1 Summary and Conclusions

A three-dimensional numerical atmospheric radiative transfer scheme coupled with a CFD code to simulate the urban Surface Energy Balance (SEB) has been developed. Validations of the full radiative-convective coupling are performed through a comparison with observation datasets from MUST (idealized built-up area, Chapter 3) and CAPITOUL (real urban environment, Chapter 6) field experiments.

The improvement of the heat transfer model for buildings and the study of the full radiative-convective coupling, are addressed in Chapters 3 and 6. The model successfully simulates a key parameter in the SEB, the surface temperature, for different sides of a container within the MUST canopy in a diurnal cycle (see Chapter 3) and also a 24 hours evolution of the brightness surface temperature for different positions in the district within the CAPITOUL study center area (see Chapter 6). The model incorporates two approaches to model heat transfer with buildings: the force-restore scheme and the wall thermal model. Tests of the performance of these two approaches show that to explicitly treat the heat conduction, even with only one-layer, the wall thermal model is more adapted for the building walls than the force-restore approach which was originally developped for the soil model (see Chapter 3). By taking advantage of the force-restore approach and the wall thermal model to separately model the ground and building walls temperatures, a hybrid surface temperature scheme shows a good ability when applied to the CAPITOUL case (see Chapter 6). In case of buildings without good insulation, the internal

building temperature has a large influence on the surface temperature in the diurnal cycle (see Chapter 3). As a solution, an evolution equation obtained from the literature is adopted to more realistically model the internal building temperature. In any case the improvement of the surface model has been identified as an area for future work.

Results from Chapter 3 and 6 also illustrate quantitatively how the sensible heat flux plays an important role in SEB. For instance, in MUST case (see Chapter 3), a difference of about 10 to 30 °C on the surface temperature is obtained in moderate wind situation when including or not the convection. Moreover, in Chapter 3, we have discussed and compared different approaches to estimate the sensible flux: constant heat transfer coefficient, using a 1D equation based on a vertical wind profile within the canopy and our 3D modeling approach. This comparison shows a difference about 4 °C on the wall. Thus we conclude that a good description of the heat transfer coefficient and its spatial variability is essential to determine the sensible heat flux in the canopy.

Based on MUST full radiative-convective validation, the atmospheric radiation model in *Code_Saturne* is well-tested in Chapter 4 to achieve the objective of comparison with the geometric view factor approach, used by the SOLENE model. The most significant differences between the two models are for the diffuse solar flux, due partly to an assumption of the homogeneous incoming diffuse solar flux from simple clear sky model in *Code_Saturne*. Nevertheless, results show that the two models agree well with each other for the time evolution of the direct solar flux, incident infrared flux and surface temperature, because the diffuse solar fluxes are relatively small in clear sky condition.

Chapter 5 serves primarily as a demonstration of the ability of our radiative model to investigate the thermal effect of buildings on the local atmospheric flow under low wind speed condition. In this short-term study, the results show that taking into account the thermal stratification has a significant influence on the wind field. The difference between the case for which we impose the temperatures and the case with temperatures calculated with 3D radiative transfer case can also be important. Moreover, under radiative condition, the temperature and vertical motion show a great sensitivity to change in the physical parameters of the wall surfaces. We illustrate that increasing the albedo from 0.1 to 0.6 (e.g. painting a dark surface to white) reduces the net radiation flux term in SEB, as a result, the temperature close to the windward wall or roof may decrease by 2 °C.

The results from the CAPITOUL case described in Chapter 6 have addressed the last ob-

jective: the validation of our approach on a real city district. The generation of the CAPITOUL complex mesh requires a important preliminary work to optimize the geometry, and in addition, we have separated 4 classes of albedo value depending on wall painting colors. Through the comparison with the Thermal InfraRed airborne images from two flights in the day of 15th July 2004, we demonstrate the importance of taking into account heterogeneities in materials and geometry to reproduce the spatial variability of the temperatures in complex urban areas. Moreover, the full coupling is tested against in situ observation during the same day. The results show that the coupling perform well overall in terms of the brightness temperature (with hybrid temperature scheme). The model predicts a good daytime sensible flux, but shows a nighttime underestimation. Similar comments can be made for the model-observation comparison of the outgoing infrared flux. Regarding the outgoing solar flux, the result shows an excellent model-observation agreement at the mast position. In the statistical study, some significant differences between the predicted and observed mean, median, standard deviation brightness temperature are identified. Despite of some significant differences between the predicted and observed statistics of brightness temperatures, the analysis provides an interesting and different approach to evaluate the model performance.

7.2 Perspectives

There are still a number of directions avenues which remain to be investigated or which have opened during this work.

The application of our radiative-dynamical coupled model for the CAPITOUL case could be extended through more model-observation comparisons, in particular for a winter day. If the anthropogenic heat flux is not significant in a summer day, it may not be neglected in winter. Thus the model should properly include variation of diurnal anthropogenic flux, eventually by using a formula proposed by Pigeon et al. (2008). Moreover, the comparison of model results with measurements carried out in winter day would address in a different way the issue of the condition of internal building temperature. Further improvements should be considered, such as the buildings in the region outside which are treated at present with a high roughness value, but should be treated with a drag-porosity approach which will permit a more realistic modeling of the wind profile in the canopy. Other additional improvements for the results might be considered such as to increase the complexity of the representative geometry of the studied

site, for instance, pitched roof; to increase the resolution of the current mesh and add one or several prism layers for the boundary layers.

The one-layer wall thermal model we used shows some limitations. In MUST case, it can reproduce the diurnal cycle of the different surface temperature only with a very low thermal conductivity. Either in MUST or in CAPITOUL, a nighttime overcooling appears by using this scheme. At day scale, at least two layers for a wall scheme are requested to obtain the surface temperature rapid changes and diurnal cycles (i.e. heat storage) (Dupont and Mestayer, 2006). We expect that the implementation of a multilayer wall thermal model may lead to improvements and can improve the temperature underestimation during the night.

The comparison of *Code_Saturne* and SOLENE radiation models and the numerical study of a low wind speed case in Chapter 4 and 5 respectively may be supplemented with more real measurement data set. Furthermore, in comparing the two radiation models, taking diffuse solar flux values from SOLENE as boundary conditions shows an improvement in *Code_Saturne*. Full implementation of a similar sky model as in SOLENE with non-uniform diffuse solar radiation distribution may be necessary in *Code_Saturne* when applications are under cloudy weather condition. The comparison also can be extended to other field experiments, such as with results presented by Hénon et al. (2011b) from CAPITOUL datasets, or to compare with other radiation models, e.g. SYRTHES (SYstèm de Résolution THErmique Solide) (Péniguel and Rupp, 2008). SYRTHES is a thermal code for a larger number industrial applications and has become open-source also. The thermal solver can be used alone if only by conduction/radiation problems or coupled with *Code_Saturne* or other fluid mechanics codes.

In the model presented in this work, the atmosphere at the microscale is considered to be transparent and non-diffusive. One of the perspective of this work is to use the 3D radiative scheme for nontransparent media, for applications like assessment of pollutant dispersion or fog formation and dissipation etc. Absorption and diffusion have significant importance. Absorption can already be taken into account by our scheme, so it requires adding the diffusion term in the resolution of the radiative transfer equation.

Regarding the dynamical aspect, in the present work, the turbulence is parameterized by the Reynolds-averaged Navier-Stokes (RANS) (more specifically, the standard $k-\varepsilon$ closure) approaches due to the limitations on computational cost. It is well known that conventional $k-\varepsilon$ models, with the turbulent viscosity formulation, tend to overestimate the level of turbulent kinetic energy around the stagnation point. In order to increase the accuracy of the predic-

tion of the airflow around buildings, one direction of future work is to use the Large Eddy Simulation (LES) approach for the convective model. A comparison between LES and RANS computations for the study of contaminant dispersion in the MUST field experiment has been assessed by Santiago et al. (2010). At the microscale level, small irregularities are shown to affect significantly the mean vertical velocity component while the mean streamwise velocity and Reynolds shear stress are shown to be less sensitive to small geometrical perturbations. For the mean streamwise velocity and Reynolds shear stress, the present LES results are found to be close to RANS results and both approaches were in satisfactory agreement with the observations. However, LES captured better the irregularity effects observed on the vertical velocity components. The magnitude of this velocity component is in general underestimated by RANS. At the mesoscale level, the small geometrical perturbation effects were found insignificant for both the spatially-averaged streamwise and vertical velocity components and as well for the spatially-averaged Reynolds shear stress. Regarding the dispersive stress, it was shown to be negligible compared to the spatially-averaged shear stress. Globally, the results obtained with LES and RANS for the spatially-averaged flow properties were found to be similar for each flow configuration considered and only slight differences were observed in their cases studied (LES in regular and irregular arrays, and RANS in regular and irregular arrays). At this scale level, it was shown that the flow properties averaged over the full MUST array flow configuration are similar to the flow properties averaged over the one unit regular container flow configuration. This result is very relevant from the urban canopy modeling point of view because the spatially-averaged flow properties computed by CFD models in a simplified configuration can be representative of the average properties of a real part of a city without large irregularities, and can be used for the improvement of the parameterization of atmospheric mesoscale models.

In CAPITOUL case, the simulated sensible heat flux at the roof surface does not compare well with the measured flux on the mast. This is probably due to the comparison does not take into account the micro-meteorology. One solution is to use a 3D back-trajectory model to identify all the surfaces (not only the roof) which influenced by the convective flux at the top of the mast. However, due to the inhomogeneities at micro-scale, back-trajectory analysis is very difficult in complex geometry with unstationary 3D field. So another solution is to calculate the convective flux from the simulation of the turbulent fluctuations by using LES model. If the computational cost remains too high for the whole day simulation, at least, LES can be applied for the shorten study such as the low wind speed case described in Chapter 5.

Finally, tests of the full model are limited to two days at two separate sites, and should be performed for a greater range of urban sites, weather conditions and seasons to more successfully separate model weaknesses from incorrect parameter specification and/or processes influencing the observations. For instance, the Joint ATREUS-PICADA Experiment (JAPEX) in situ experimental campaign of which the buildings were idealized by the containers was established. Two principal objectives of the JAPEX experiment were to evaluate buildingstreet-atmosphere thermal transfers and the energy budget of a street, to document the re-circulation flow in a street (Idczak et al., 2007, 2010). Since the measurement includes more data than in the MUST filed experiemnt such as radiation data, it can be used to be a complementary work for the studies with the idealized cases (Chapter 3, 4 and 5). A more recent field experiment, Towards Optimisation of urban-planning and architectural Parameters for Energy Use minimisation in Mediterranean cities (TOPEUM) campaign has been carried out in the city of Nicosia, in Cyprus in July 2010 (Neophytou et al., 2011). The main objective of TOPEUM is to investigate the influence of different urbanisation characteristics (such as the geometry and density of buildings within a city and the type of building materials used) on the intensity of the urban heating effect in the case of a typical Mediterranean city, such as a Cypriot urban area. The field measurements include meteorological measurements as well as on-ground and aerial thermal infrared pictures, covering a range of spatial scales, from local-street canyon to meso-scale. The measurements record the meteorology, the resulting local microclimate, particularly in the street and the thermal response of the buildings in the field area, especially the building inside temperature measurement. This can provide a good verification for the accuracy of the evolution equation which we used to estimate the internal building temperature.

Bibliography

AIJ, 2004: Recommendations for loads on buildings. Technical report, Architectural Institute of Japan. 21

Antoine, M. J. and D. Groleau, 1998: Assessing solar energy and environmental variables in urban outdoor spaces: Towards a simulation and monitoring tool. *Rebuild the European cities of Tomorrow : Shaping our European cities for, for the 21st Century Proceedings of the 2nd European Conference*, Florence, Italy (April 1-3, 1998). 68, 69

Archambeau, F., N. Méchitoua, and M. Sakiz, 2003: *Code_Saturne*: a Finite Volume Code for the Computation of Turbulent Incompressible Flows - Industrial Applications. *Int. J. Finite. Volumes*, **1**, 1–62 [Available online at http://www.latp.univ–mrs.fr//IJFVDB/saturne.pdf]. 36

Arnfield, A. J., 2003: Two decades of urban climate research: A review of turbulence, exchanges of energy and water, and the urban heat island. *Int. J. Climatol.*, **23 (1)**, 1–26. 46

Asawa, T., A. Hoyano, and K. Nakaohkubo, 2008: Thermal design tool for outdoor space based on a numerical simulation system using 3D-CAD. *Build. Environ.*, **43 (12)**, 2112–2123. 63, 64

Baldwin, B. S. and H. Lomax, 1978: Thin layer approximation and algebraic model for separated turbulent flows. *AIAA*, 78–257. 15

Best, M. J., C. S. B. Grimmond, and M. G. Villani, 2006: Evaluation of the urban tile in MOSES using surface energy balance observations. *Bound.-Layer Meteor.*, **118 (3)**, 503–525. 32

Bird, R. E. and R. L. Hulstrom, 1981: A simplified clear sky model for direct and diffuse insolation on horizontal surfaces. Tech. Rep. SERI/TR-642-761, Solar Research Institute, 38 pp., Golden, Colorado. 42, 43, 72

Blocken, B., 2009: Pedestrian wind comfort around a large football stadium in an urban environment: CFD simulation, validation and application of the new Dutch wind nuisance standard. *J. Wind Eng. Ind. Aerod.*, **97 (5-6)**, 255–270. 14

Blocken, B., T. Defraeye, D. Derome, and J. Carmeliet, 2009: High-resolution CFD simulations for convective heat transfer coefficients at the facade of a low-rise building. *Build. Environ.*, **44 (12)**, 2396–2412. 14

Blocken, B., T. Stathopoulos, and J. Carmeliet, 2007: CFD simulation of the atmospheric boundary layer: wall function problems. *Atmos. Environ.*, **41(2)**, 238–252. 23

Boussinesq, J., 1877: Essai sur la theories des eaux courantes. *Memoires presentes par divers savants a l'Academic des Sciences de l'Institut National de France*, **23**, 46–50. 15

Bouyer, J., 2009: Modélisation et simulation des microclimats urbains: Étude de l'impact de l'aménagement urbain sur les consommations énergétiques des bâtiments. Ph.D. thesis, École Polytechnique de l'Université de Nantes, 306 pp., [in French]. 35, 65

Briggen, P. M., B. Blocken, and H. L. Schellen, 2009: Wind-driven rain on the facade of a monumental tower: numerical simulation, full-scale validation and sensitivity analysis. *Build. Environ.*, **44 (8)**, 1675–1690. 14

Brown, M. J. and M. D. Williams, 1998: An urban canopy parameterization for mesoscale meteorological models. *AMS 2nd Urban Environment Conf.*, Albuquerque, New Mexico (November 1998). 29

Camuffo, D. and A. Bernardi, 1982: An observational study of heat fluxes and the relationship with net radiation. *Bound.-Layer Meteor.*, **23 (3)**, 359–368. 11

Casey, M. and T. Wintergerste, 2000: Best Practice Guidelines, ERCOFTAC Special Interest Group on Quality and Trust in Industrial CFD. Tech. rep., Fluid Dynamics Laboratory Sulzer Innotec, ERCOFTAC, Brussels. 16, 17

Chapman, D. R., 1979: Computational aerodynamics development and outlook. *AIAA*, **17**, 1293–1313. 15

Chen, H., R. Ooka, H. Huang, and T. Tsuchiya, 2009: Study on mitigation measures for outdoor thermal environment on present urban blocks in Tokyo using coupled simulation. *Build. Environ.*, **44 (11)**, 2290–2299. 32, 35

Coceal, O., A. Dobre, T. G. Thomas, and S. E. Belcher, 2007: Structure of turbulent flow over regular arrays of cubical roughness. *J. Fluid Mech.*, **589**, 375–409. 15

Cook, M., Y. Ji, and G. Hunt, 2003: CFD modelling of natural ventilation: combined wind and buoyancy forces. *Int. J. Ventilation*, **1**, 169–180. 14

Courant, R., K. Friedrichs, and H. Lewy, 1967: On the partial difference equations of mathematical physics. *IBM Journal*, 215–234. 18

Dandou, A., M. Tombrou, E. Akylas, N. Soulakellis, and E. Bossioli, 2005: Development and evaluation of an urban parameterization scheme in the Penn StateNCAR Mesoscale model (MM5). *J. Geophys. Res.*, **110**, D10 102. 32

Davidson, P. A., 2004: *Turbulence - An Introduction for Scientists and Engineers*. Oxford University Press, 678 pp. 14

Deardorf, J. W., 1978: Efficient prediction of ground surface temperature and moisture with inclusion of a layer of vegetation. *J. Geophys. Res.*, **83**, 1889–1903. 44

Douce, A. and N. Méchitoua, 2003: Mise en œuvre dans *Code_Saturne* des modélisations physiques particulière, Tome 3: Transfert thermique radiatif en milieux gris semi-transparents. Rapport interne EDF, [in French], EDF R&D, Fluid Mechanics and Heat Transfer Department. 40

Dupont, S., I. Calmet, and P. G. Mestayer, 2002: Urban canopy modeling influence on urban boundary layer simulation. *Fourth Symp. on Urban Environment*, Norfolk, Virginia (May 20-24, 2002), pp. 151-152. 30

Dupont, S. and P. G. Mestayer, 2006: Parameterization of the urban energy budget with the submesoscale soil model. *J. Appl. Meteor. Climatol.*, **45 (12)**, 1744–1765. 30, 32, 44, 150

Dupont, S., T. L. Otte, and J. K. S. Ching, 2004: Simulation of meteo-rological fields within and above urban and rural canopies with a mesoscale model (MM5). *Bound-Layer. Meteorol.*, **113 (1)**, 111–158. 30

Fiveland, W. A., 1984: Discrete-ordinates solutions of the radiative transport equation for rectangular enclosure. *J. Heat Tran.*, **106 (4)**, 699–706. 41

Fortuniak, K., B. Offerle, and C. S. B. Grimmond, 2005: Application of a slab surface energy balance model to determine surface parameters for urban areas. *Lund eRep. Phys. Geog.*, **5**, 90–91. 32

Franke, J., A. Hellsten, H. Schlünzen, and B. Carissimo, 2007: Best Practice Guideline for the CFD simulation of flows in the urban environment: COST Action 732: Quality Assurance and Improvement of Microscale Meteorological Models. Tech. Rep. ISBN 3-00-018312-4, COST Office Brussels. 16, 17, 18, 19, 20, 21, 22, 24, 27, 28, 120

Gastellu-Etchegorry, J. P., 2008: 3D modeling of satellite spectral images, radiation budget and energy budget of urban landscapes. *Meteor. Atmos. Phys.*, **102 (3-4)**, 187–207. 31, 39, 63, 119

Gastellu-Etchegorry, J. P., E. Martin, and F. Gascon, 2004: Dart: A 3-D model for simulating satellite images and surface radiation budget. *Int. J. of Remote Sens.*, **25**, 75–96. 31, 119

Grell, G., J. Dudhia, and D. R. Stauffer, 1994: *A Description of the Fifth-Generation Penn State/NCAR Mesoscale Model (MM5)*. NCAR/TN-398+STR, 138 pp. 29

Grimmond, C. S. B. and T. R. Oke, 1999a: Aerodynamic properties of urban areas derived from analysis of surface form. *J. Appl. Meteor.*, **38 (9)**, 1262–1292. 29

Grimmond, C. S. B. and T. R. Oke, 1999b: Heat storage in urban areas: Local-scale Observations and Evaluation of a Simple model. *J. Appl. Meteor.*, **38 (7)**, 922–940. 10, 11

Grimmond, C. S. B. and T. R. Oke, 2002: Turbulent heat fluxes in urban areas: Observations & local-scale urban meteoro-logical parameterization scheme (LUMPS). *J. Appl. Meteor.*, **41 (7)**, 792–810. 29

Grimmond, C. S. B., et al., 2010: The International Urban Energy Balance Models Comparison Project: First Results from Phase 1. *J. Appl. Meteor. Climatol*, **49 (6)**, 1268–1292. 31, 32, 33

Grimmond, C. S. B., et al., 2011: Initial results from Phase 2 of the international urban energy balance model comparison. *Int. J. Climatol.*, **31 (2)**, 244–272. 31

Hamdi, R. and V. Masson, 2008: Inclusion of a drag approach in the Town Energy Balance (TEB) scheme: offline 1-D evaluation in a street canyon. *J. Appl. Meteor. Climatol*, **47 (10)**, 2627–2644. 32

Hanna, S. R., et al., 2006: Detailed simulations of atmospheric flow and dispersion in downtown manhattan: An application of five computational fluid dynamics model. *Bull. Amer. Meteor. Soc.*, **87**, 1713–1726. 14

Harman, I. N. and S. E. Belcher, 2004: Radiative exchange in an urban street canyon. *Bound.-Layer Meteor.*, **110 (2)**, 301–316. 32

Harman, I. N. and S. E. Belcher, 2006: The surface energy balance and boundary layer over urban street canyons. *Quart. J. Roy. Meteor. Soc.*, **132 (621)**, 2749–2768. 32

Hémon, D. and E. Jougla, 2003: Estimation de la surmortalité et principales caractéristiques épidémiologiques. Technical report, [in French], INSERM. 2

Hénon, A., 2008: Températures mesurées, modélisées, et observées par télédétection infrarouge, dans la canopée urbaine: modélisation aéro-thermo-radiatif des flux de chaleur urbains. Ph.D. thesis, École Centrale de Nantes, 253 pp., [in French]. 47, 65, 68, 126, 127, 128, 129

Hénon, A., P. G. Mestayer, D. Groleau, and J. A. Voogt, 2011a: High resolution thermo-radiative modeling of an urban fragment in Marseilles city center during the UBL-ESCOMPTE campaign. *Build. Environ.*, **46 (9)**, 1747–1764. 65, 69

Hénon, A., P. G. Mestayer, J. P. Lagouarde, and J. A. Voogt, 2011b: An urban neighborhood temperature and energy study from the CAPITOUL experiment with the Solene model. Part 1: analysis of flux contributions. *submitted to Theor. Appl. Climatol.* 65, 117, 119, 126, 130, 136, 150

Hénon, A., P. G. Mestayer, J. P. Lagouarde, and J. A. Voogt, 2011c: An urban neighborhood temperature and energy study from the CAPITOUL experiment with the Solene model. Part 2: influence of building surface heterogeneities. *submitted to Theor. Appl. Climatol.* 65

Howard, L., 1820: *The climate of London, deduced from Meteorological observations, made at different places in the neighbourhood of the metropolis. Vol 1*. Harvey and Darton, 358 pp. 2

Idczak, M., D. Groleau, P. Mestayer, J.-M. Rosant, and J.-F. Sini, 2010: An application of the thermo-radiative model SOLENE for the evaluation of street canyon energy balance. *Build. Environ.*, **45 (5)**, 1262–1275. 152

Idczak, M., P. Mestayer, J.-M. Rosant, J.-F. Sini, and M. Violleau, 2007: Micrometeorological

measurements in a street canyon during the joint atreus-picada experiment. *Bound.-Layer Meteor.*, **124 (1)**, 25–41. 152

Jesionek, K. and M. Bruse, 2003: Impacts of vegetation on the microclimate: modeling standardized building structures with different greening levels. *Fifth Int. Conf. on Urban Climate*, Lodz, Poland (September 1-5, 2003). 35

Johnson, G. T., T. R. Oke, T. J. Lyons, D. G. Steyn, I. D. Watson, and J. A. Voogt, 1991: Simulation of surface urban heat islands under 'ideal' conditions at night. Part I: Theory and tests against field data. *Bound.-Layer Meteor.*, **56 (3)**, 275–294. 44

Kanda, M., , R. Moriwaki, and F. Kasamatsu, 2004: Large-eddy simulation of turbulent organized structures within and above explicitly resolved cube arrays. *Bound.-Layer Meteor.*, **112 (2)**, 343–368. 15

Kanda, M., T. Kawai, M. Kanega, R. Moriwaki, K. Narita, and A. Hagishima, 2005: A simple energy balance model for regular building arrays. *Bound.-Layer Meteor.*, **116 (3)**, 423–443. 32, 64

Kato, M. and B. Launder, 1993: The modelling of turbulent flow around stationary and vibrating square cylinders. *Ninth symposium on turbulent shear flows*, Kyoto, Japan (August 16-18, 1993). 15

Kawai, T., M. Kanda, K. Narita, and A. Hagishima, 2007: Validation of a numerical model for urban energy-exchange using outdoor scale-model measurements. *Int. J. Climatol.*, **27 (14)**, 1931–1942. 32

Kawamoto, Y. and R. Ooka, 2009: Accuracy validation of urban climate analysis model using MM5 incorporating a multi-layer urban canopy model. *Seventh International Conference on Urban Climate, ICUC-7*, Yokohama, Japan, (June 28 - July 3, 2009) Extended abstract: A10-1. 32

Knaus, H., R. Schneider, X. Han, J. Ströjle, U. Schnell, and K. R. G. Hein, 1997: Comparison of different radiative heat transfer models and their applicability in coal-fired utility boiler simulations. *Fourth Int. Conf. on Technologies and Combustion for a Clean Environment*, Lisbon, Portugal (July 7-10, 1997). 41

Kondo, H., Y. Genchi, Y. Kikegawa, Y. Ohashi, H. Yoshikado, and H. Komiyama, 2005: Development of a Multi-Layer Urban Canopy Model for the Analysis of Energy Consumption in a Big City: Structure of the Urban Canopy Model and its Basic Performance. *Bound.-Layer Meteor.*, **116 (3)**, 395–421. 32

Krayenhoff, E. S. and J. A. Voogt, 2007: A microscale three-dimensional urban energy balance model for studying surface temperatures. *Bound.-Layer Meteor.*, **123 (3)**, 433–461. 31, 32, 39, 46, 47, 63, 64

Kurz, B., 2009: Modélisation de l'anisotropie directionnelle de la température de surface: application au cas de milieux forestiers et urbains. Ph.D. thesis, Université de Toulouse, 144 pp., [in French]. 65

Kusaka, H., H. Kondo, Y. Kikegawa, and F. Kimura, 2001: A simple single-layer urban canopy model for atmospheric models: comparison with multi-layer and slab models. *Bound.-Layer Meteor.*, **101 (3)**, 329–358. 32

Lagouarde, J. P., A. Hénon, B. Kurz, P. Moreau, M. Irvine, J. Voogt, and P. Mestayer, 2010: Modelling daytime thermal infrared directional anisotropy over Toulouse city centre. *Remote Sens. Environ.*, **114 (1)**, 87–105. 117, 119, 127, 128

Launder, B. E., G. J. Reece, and W. Rodi, 1975: Progress in the Development of a Reynolds-Stress Turbulent Closure. *J. Fluid Mech.*, **68 (3)**, 537–566. 15

Launder, B. E. and D. B. Spalding, 1974: The numerical computation of turbulent flow. *Comp. Meth. Appl. Mech. Eng.*, **3**, 269–289. 15, 38

Lawson, T. V. and A. D. Penwarden, 1975: The effects of wind on people in the vicinity of buildings. *Fourth Int. Conf. on Wind Effects on Buildings and Structures*, Heathrow, Cambridge University Press, (pp. 605-622). 4

Lee, S.-H. and S.-U. Park, 2004: A vegetated urban canopy model for meteorological and environmental modelling. *Bound.-Layer Meteor.*, **126 (1)**, 73–102. 32

Lemonsu, A., C. S. B. Grimmond, and V. Masson, 2004: Modelling the surface energy balance of an old Mediterranean city core. *J. Appl. Meteor.*, **43 (2)**, 312–327. 30

Liu, J., H. M. Shang, and Y. S. Chen, 2000: Development of an unstructured radiation model applicable for two-dimensional planar, axisymmetric, and three-dimensional geometries. *J. Quant. Spectrosc. Radiat. Transfer*, **66 (1)**, 17–33. 41

Loomans, M. G. L. C., M. van Houdt, A. D. Lemaire, and J. L. M. Hensen, 2008: Performance assessment of an operating theatre design using CFD simulation and tracer gas measurements. *Indoor and Built Environment*, **17 (4)**, 299–312. 13

Louis, J., 1979: A parametric model of vertical eddy fluxes in the atmosphere. *Bound.-Layer Meteor.*, **17 (2)**, 187–202. 48

Martilli, A., A. Clappier, and M. W. Rotach, 2002: An urban surface exchange parameterisation for mesoscale models. *Bound.-Layer Meteor.*, **104 (2)**, 261–304. 30, 32

Masson, V., 2000: A physically based scheme for the urban energy budget in atmospheric models. *Bound.-Layer Meteor.*, **94 (3)**, 357–397. 30, 32, 63, 117

Masson, V., 2006: Urban surface modeling and the meso-scale impact of cities. *Theor. Appl. Climatol.*, **84 (1-3)**, 35–45. 29

Masson, V., C. S. B. Grimmond, and T. R. Oke, 2002: Evaluation of the Town Energy Balance (TEB) Scheme with Direct Measurements from Dry Districts in Two cities. *J. Appl. Meteor.*, **41 (10)**, 1011–1026. 30, 46

Masson, V., et al., 2008: The Canopy and Aerosol Particles Interactions in TOulouse Urban Layer (CAPITOUL) experiment. *Meteor. Atmos. Phys.*, **102 (3-4)**, 135–157. 114, 115

Maxwell, E. L., 1998: METSTAT-the solar radiation model used in the production of the National Solar Radiation Data Base (NSRDB). *Solar Energy*, **62 (4)**, 263–279. 42

McCarthy, M. P., M. J. Best, and R. A. Betts, 2010: Climate change in cities due to global warming and urban effects. *Geophys. Res. Lett.*, **37**, L09 705, doi:10.1029/2010GL042 845. 2

Miguet, F. and D. Groleau, 2002: A daylight simulation tool for urban and architectural spaces - application to transmitted direct and diffuse light through glazing. *Build. Environ.*, **37 (8)**, 833–843. 12, 31, 42, 46, 63, 64, 66

Milliez, M., 2006: Modélisation micro-météorologique en milieu urbain: dispersion des polluants et prise en compte des effets radiatifs. Ph.D. thesis, École des Ponts ParisTech, 228 pp., [in French, available on line at http://cerea.enpc.fr/fr/theses.html]. 11, 12, 14, 29, 36, 39, 40, 43, 44, 45, 114

Milliez, M. and B. Carissimo, 2007: Numerical simulations of pollutant dispersion in an idealized urban area, for different meteorological conditions. *Bound.-Layer Meteor.*, **122 (2)**, 321–342. 37

Mills, G., 1997: An Urban Canopy-Layer Climate Model. *Theor. Appl. Climatol.*, **57 (3-4)**, 229–244. 46, 63

Moin, P. and K. Mahesh, 1998: Direct numerical simulation: A tool in turbulence research. *Annu. Rev. Fluid Mech.*, **30**, 539–578. 14

Monteith, J. L. and M. H. Unsworth, 1990: *Principles of environment physics*. 2d ed., Edward Arnold, 291 pp. 67

Moscicki, M. A., 2007: A Comparison of Modeled and Observed Surface Temperatures in Toulouse, France. Ph.D. thesis, The University of Western Ontario, 170 pp. 47, 115, 117

Musson-Genon, L., 1993: Paramétrisation du rayonnement infra-rouge dans le code atmosphérique mercure (version 3.1). Rapport interne EDF, [in French], EDF R&D, Fluid Mechanics and Heat Transfer Department. 39

Musson-Genon, L., 1994: Paramétrisation du rayonnement solaire dans le code atmosphérique mercure (version 3.1). Rapport interne EDF, [in French], EDF R&D, Fluid Mechanics and Heat Transfer Department. 39

Musson-Genon, L., E. Dupont, and D. Wendum, 2007: Reconstruction of the Surface-Layer Vertical Structure from Measurements of Wind, Temperature and Humidity at Two Levels. *Bound.-Layer Meteor.*, **124 (2)**, 235–250. 48

Neophytou, M., et al., 2011: Towards optimization of urban planning and architectural parameters for energy use minimization in Mediterranean cities. *World Renewable Energy Congress 2011*, Linköping, Sweden (May 8-11, 2011). 152

Offerle, B., C. S. B. Grimmond, and T. R. Oke, 2003: Parameterization of net all-wave radiation for urban areas. *J. Appl. Meteor. Climatol.*, **42 (8)**, 1157–1173. 32

Oke, T. R., 1987: *Boundary Layer Climates*. 2d ed., Routledge, 435 pp. 1, 2, 5, 7, 8, 9

Oke, T. R., R. Spronken-Simith, E. Jáuregui, and C. S. B. Grimmond, 1999: The energy balance of central Mexico City during the dry season. *Atmos. Environ.*, **33 (24-25)**, 3919–3930. 5

Oleson, K. W., G. B. Bonan, J. Feddema, M. Vertenstein, and C. S. B. Grimmond, 2008: An urban parameterization for a global climate model: 1. Formulation & evaluation for two cities. *J. Appl. Meteor. Climatol.*, **47 (4)**, 1038–1060. 32

Orlanski, I., 1975: A rational subdivision of scales for atmospheric processes. *B. Am. Meteorol. Soc.*, **56**, 527–530. 5

Péniguel, C. and I. Rupp, 2008: SYRTHES 3.4 - Manuel Théorique. Technical report, [in French], EDF R&D, Fluid Mechanics and Heat Transfer Department. 150

Perez, R., R. Seals, and J. Michalsky, 1993: An all-weather model for sky luminance distribution. *Sol. Energ.*, **50**, 235–245. 66

Pigeon, G., D. Legain, P. Durand, and V. Masson, 2007: Anthropogenic heat release in an old European agglomeration (Toulouse, France). *Int. J. Climatol.*, **27 (14)**, 1969–1981. 10, 117

Pigeon, G., M. A. Moscicki, J. A. Voogt, and V. Masson, 2008: Simulation of fall and winter surfac energy balance over a dense urban area using the TEB scheme. *Meteorol. Atmos. Phys.*, **102 (3-4)**, 159–171. 115, 117, 123, 125, 136, 149

Pope, S. B., 2000: Turbulent flows. *Cambridge University Press*, **125**, 1361–1362. 16

Prandtl, L., 1925: Bericht über untersuchungen zur ausgebildeten turbulenz, Z. angew. *Math, Meth.*, **5**, 136–139. 15

Prata, A. J., 1996: A new long-wave formula for estimating downward clear-sky radiation at the surface. *Q. J. R. Meteorol. Soc.*, **122**, 1127–1151. 43

Randerson, D., 1976: An overview of regional-scale numerical models. *Bull. Am. Met. Soc.*, **57**, 797–804. 5

Ringenbach, N., 2004: Bilan radiatif et flux de chaleur en climatologie urbaine: mesures, modélisation et validation sur strasbourg. Ph.D. thesis, Université Louis Pasteur Strasbourg I, 180 pp., [in French]. 65

Robitu, M., 2005: Étude de l'interaction entre le bâtiment et son environnement urbain: influence sur les conditions de confort en espaces extérieurs. Ph.D. thesis, École Polytechnique de l'Université de Nantes, 264 pp., [in French]. 65

Rotach, M. W., et al., 2005: BUBBLE- an Urban Boundary Layer Meteorology Project. *Theor. Appl. Climatol.*, **81 (3-4)**, 231–261. 7

Ryu, Y.-H., , J.-J. Baik, and S.-H. Lee, 2009: A new single-layer urban canopy model for use in mesoscale atmospheric models. *Proceedings of the Seventh International Conference on Urban Climate, ICUC-7*, Yokohama, Japan, (June 28 - July 3, 2009) Extended abstract: A10-1. 32

Salamanca, F., A. Krpo, A. Martilli, and A. Clappier, 2009: A new building energy model coupled with an urban canopy parameterization for urban climate simulationsâpart I.formulation, verification, and sensitivity analysis of the model. *Theor. Appl. Climatol.*, **99 (3-4)**, 331–344. 32

Santiago, J. L., A. Dejoan, A. Martilli, F. Martin, and A. Pinelli, 2010: Comparison Between Large-Eddy Simulation and Reynolds-Averaged Navier-Stokes Computations for the MUST Field Experiment. Part I: Study of the Flow for an Incident Wind Directed Perpendicularly to the Front Array of Containers. *Bound.-Layer Meteor.*, **135 (1)**, 109–132. 15, 151

Schlünzen, K. H., D. Grawea, S. I. Bohnenstengelb, I. Schlüterc, and R. Koppmannd, 2011: Joint modelling of obstacle induced and mesoscale changes–Current limits and challenges. *J. Wind Eng. Ind. Aerodyn.*, **99 (4)**, 217–225. 5, 6

Shashua-Bar, L. and M. E. Hoffman, 2004: Quantitative evaluation of passive cooling of the UCL microclimate in hot regions in summer. *Build. Environ.*, **39 (9)**, 1087–1099. 32

Shirasawa, T., R. Yoshie, H. Tanaka, T. Kobayashi, A. Mochida, and Y. Endo, 2008: Cross comparison of CFD results of gas diffusion in weak wind region behind a high-rise building. *Proceedings of the 4th International Conference on Advances in Wind and Structures (AWAS'08)*, Jeju, Korea, (May 2008) 1038-1050. 4

Soux, A., J. A. Voogt, and T. R. Oke, 2004: A Model to Calculate What a Remote Sensor 'Sees' of an Urban Surface. *Bound.-Layer Meteorol.*, **111 (1)**, 109–132. 66

Stephens, G. L., 1984: The parameterization of radiation for numerical weather prediction and climate models. *Mon. Weather. Rev.*, **112**, 826–867. 39

Stull, R. B., 1988: *An Introduction To Boundary Layer Meteorology*. Kluwer Academic Publisher, Dordrecht, The Netherlands, 670 pp. 5, 20

Tominaga, Y., A. Mochida, R. Yoshie, H. Kataoka, T. Nozu, M. Yoshikawa, and T. Shirasawa, 2008: AIJ guidelines for practical applications of CFD to pedestrian wind environment around buildings. *J. Wind Eng. Ind. Aerodyn.*, **96 (10-11)**, 1749–1761. 16, 17, 18, 19, 20, 21, 24, 28, 120

Truelove, J. S., 1987: Discrete-ordinates solutions of the radiative transport equation. *J. Heat Tran.*, **109**, 1048–1051. 41

Washington, W. M., 1972: Numerical climatic-change experiments: The effect of mans production of thermal energ. *J. Appl. Meteorol*, **11 (5)**, 768–772. 10

WBCSD, 2009: Energy Efficiency in Buildings. WBCSD news, World Business Council for Sustainable Development. 3

WHO, 2006: Air quality guidelines. Global update 2005. particulate matter, ozone, nitrogen dioxide and sulfur dioxide. Technical report, The World Health Organization. 3

Xie, Z.-T., O. Coceal, and I. P. Castro, 2008: Large-eddy simulation flows over random urban-like obstacles. *Bound.-Layer Meteor.*, **129 (1)**, 1–23. 15

Yakhot, V., S. A. Orszag, S. Thangam, T. B. Gatski, and C. G.Speziale, 1992: Development of turbulence models for shear flows by a double expansion technique. *Phys. Fluids*, **4**, 1510–1520. 15

Yamada, T., 1982: A numerical study of turbulent airflow in and above a forest canopy. *J. Met. Soc. Japan*, **60**, 439–454. 29

Yang, K., G. W. Huang, and N. Tamai, 2001: A hybrid model for estimating global solar radiation. *Solar Energy*, **70 (1)**, 13–22. 43

Three-dimensional modeling of radiative and convective exchanges in the urban atmosphere

Abstract: In many micrometeorological studies, building resolving models usually assume a neutral atmosphere. Nevertheless, urban radiative transfers play an important role because of their influence on the energy budget. In order to take into account atmospheric radiation and the thermal effects of the buildings in simulations of atmospheric flow and pollutant dispersion in urban areas, we have developed a three-dimensional (3D) atmospheric radiative scheme, in the atmospheric module of the Computational Fluid Dynamics model *Code_Saturne*. The radiative scheme was previously validated with idealized cases, using as a first step, a constant 3D wind field. In this work, the full coupling of the radiative and thermal schemes with the dynamical model is evaluated. The aim of the first part is to validate the full coupling with the measurements of the simple geometry from the 'Mock Urban Setting Test ' (MUST) experiment. The second part discusses two different approaches to model the radiative exchanges in urban area with a comparison between *Code_Saturne* and SOLENE. The third part applies the full coupling scheme to show the contribution of the radiative transfer model on the airflow pattern in low wind speed conditions in a 3D urban canopy. In the last part we use the radiative-dynamics coupling to simulate a real urban environment and validate the modeling approach with field measurements from the 'Canopy and Aerosol Particles Interactions in TOulouse Urban Layer' (CAPITOUL).

Keywords: Urban physics, Urban energy balance, Surface temperature, 3D radiation modeling, CFD, Coupling

Modélisation tri-dimensionnelle des échanges radiatifs et convectifs dans l'atmosphère urbaine

Résume: Dans de nombreuses études micrométéorologiques, les modèles numeriques prenant en compte les bâtiments considèrent généralement l'atmosphère comme neutre. Néanmoins, les transferts radiatifs urbains jouent un rôle important en raison de leur influence sur le bilan énergétique. Afin de prendre en compte le rayonnement atmosphérique et les effets thermiques des bâtiments dans les simulations de l'écoulement atmosphérique et la dispersion des polluants en milieux urbains, nous avons développé un modèle de rayonnement atmosphérique tridimensionnel (3D), dans le module atmosphérique du code de mécanique des fluides *Code_Saturne*. Le schéma radiatif a été précédemment validé avec des cas idéalisés, en utilisant dans un premier temps, un champ constant de vent 3D. Dans ce travail, le couplage des schémas radiatifs et thermiques avec le modèle dynamique est évalué. L'objectif de la première partie est de valider le couplage complet avec les mesures de la campagne de mesure américaine 'Mock Urban Setting Test' (MUST) sur des géométries simples. La deuxième partie traite deux approches différentes pour modéliser les échanges radiatifs en milieu urbain avec une comparaison entre *Code_Saturne* et SOLENE. La troisième partie utilise le couplage complet pour montrer l'apport du modèle de transfert radiatif sur l'écoulement de l'air dans des conditions de faible vitesse du vent dans une canopée 3D. Dans la dernière partie, nous utilisons le couplage dynamique-radiatif pour simuler un environnement urbain réel et valider le modèle avec les données expérimentales de la campagne 'Canopy and Aerosol Particles Interactions in TOulouse Urban Layer' (CAPITOUL).

Mot-clés: Physique urbaine, Budget énergétique urbaine, Température de surface, Modélisation du rayonnement 3D, CFD, Couplage